UNIVERSITÉ DE MONTRÉAL

THEORETICAL AND EXPERIMENTAL STUDIES OF LASER INDUCED COOLING OF SOLIDS

ELTON SOARES DE LIMA FILHO

DÉPARTEMENT DE GÉNIE PHYSIQUE

ÉCOLE POLYTECHNIQUE DE MONTRÉAL

THÈSE PRÉSENTÉE EN VUE DE L'OBTENTION

DU DIPLÔME DE PHILOSOPHIÆ DOCTOR

(GÉNIE PHYSIQUE)

MAI 2015

UNIVERSITÉ DE MONTRÉAL

ÉCOLE POLYTECHNIQUE DE MONTRÉAL

Cette thèse intitulée:

THEORETICAL AND EXPERIMENTAL STUDIES OF LASER INDUCED COOLING OF SOLIDS

présentée par : SOARES DE LIMA FILHO Elton

en vue de l'obtention du diplôme de : Philosophiæ Doctor

a été dûment acceptée par le jury d'examen constitué de :

M. FRANCOEUR Sébastien, Ph. D., président

M. KASHYAP Raman, Ph. D., membre et directeur de recherche

M. RUDA Harry, Ph. D., membre

M. KASAP Safa, Ph. D., membre externe

DEDICACE

Dedicated to my parents.

ACKNOWLEDGEMENTS

Writing this PhD thesis was a challenging task, which would not be possible to make without the help of the great people I had met during this long journey. I wish to thank my research supervisor, Raman Kashyap, whose over-the-clock support allowed the completion of many publications related to this Thesis. His guidance has been fundamental to polish my skills, and to pave my way towards independent research.

Furthermore, I would like to thank Prof. S. Francoeur, Prof. S. Kasap and Prof. H. Ruda for giving part of their precious time to kindly evaluate my Ph. D. thesis.

I would like to thank Dr. S. Bowman, Dr. M. Saad, Prof. Y. Messaddeq's group, Dr. M. Quintanilla, Prof. Vetrone and Dr. K. V. Krishnaiah, for their immense work manufacturing some of the samples studied here.

The last five years spent in the APCL/FABULAS group were very rewarding to me. These years would not pass so fast, were not for the awesome people there. Several colleagues and friends have contributed in their way for this great experience: Jêrome Lapointe, Meenu Kajal, Mathieu Gagné, Ameneh Bostani, Mohamad Diaa Baiad, Mamoun Wahbeh, Sébastien Loranger, François Parent and Ye-Jin Yu.

I thank the many friends from the outside world who helped me to keep my sanity and physical health in acceptable shape. Many thanks to Mmes. Bouilly, Blaney, Lavoie-Gauthier and d'Messier, as well as to Filipe Salles, Thiago Mendes and Fabrício A. Fonseca, for their patience and kind support. I also like to thank Dr. Talbot for the fruitful discussions, and to Dr. Gagnon and Maude, as well as to all my outdoorsy friends who never let me fall, literally.

I would like to thank the co-authors of my papers and all who have helped in the advancement of my project. I would like to thank for the technical assistance of Mr. Gauthier, Mr. Dubé, J. S. Décarie and Mr. Babian who spent many hours making things work.

Finally, I can't express enough my gratitude to my family members, friends, and professors, for their support and motivation. I reserve special thanks to my parents Elvira and Elton for their sacrifices, and to my early mentors Prof. José Luiz M. Valle and Prof. Bernhard Lesche for their patience, honesty and tirelessness which set my reference as researcher and individual.

RÉSUMÉ

La plupart des recherches en technologies de réfrigération se concentrent dans l'amélioration de l'efficacité énergétique des réfrigérateurs et climatiseurs avides d'énergie, tandis qu'une petite fraction de la recherche est dédiée à la miniaturisation et à la flexibilité. La demande accrue pour des outils précis pour des mesures et fabrications générales, ainsi que la production, le traitement et la transmission de données, repoussent les limites de dispositifs électroniques et photoniques. Ces dispositifs nécessitent une gestion thermique qui n'est pas toujours possible d'atteindre avec les méthodes conventionnelles de réfrigération, en raison de la nécessité de miniaturisation, du transport thermique à distance et dans l'espace précis, l'insensibilité aux rayonnements électromagnétiques et des vibrations mécaniques ainsi que des capacités cryogéniques. Une technologie qui pourrait répondre à ces exigences est le refroidissement optique, où la chaleur est convertie en rayonnement optique, à travers un processus optique.

Plusieurs segments de l'industrie moderne, ainsi que de la vie quotidienne, sont dépendants de la technologie laser. Cette large dépendance pousse le besoin de plus petits et plus puissants lasers pour les télécommunications, la recherche, les applications militaires, médicales et d'affichage, pour ne citer que quelques-uns. Le premier goulot d'étranglement pour la montée en puissance des lasers est dû à la production de chaleur, et la gestion thermique externe ne résout qu'une partie du problème, puisque les gradients thermiques – qui produisent des effets lenticulaires – sont encore présents. Etant donné que le refroidissement optique peut fournir une gestion thermique *in situ*, il peut être utilisé pour éliminer ces gradients thermiques nuisibles. Actuellement, le besoin d'efficacité énergétique est le moteur du changement de la technologie d'éclairage vers les diodes électroluminescentes (DELs). Les DELs souffrent cependant de génération de chaleur due à l'extraction limitée de la lumière et des pertes résistives, qui diminuent considérablement la durée de vie de ces émetteurs à semi-conducteurs. Ils ont donc besoin des échangeurs de chaleur relativement grands, qui à leur tour rendent difficile la miniaturisation. Le refroidissement par laser pourrait offrir une solution potentielle pour la gestion de la chaleur dans cette application, ainsi que pour des applications électroniques d'haute vitesse et pour des composants optiques de la prochaine génération d'ordinateurs, dans lequel une gestion de chaleur similaire est également nécessaire. La réfrigération à distance, compact et sans vibrations, fournie par le refroidissement optique peut faire bénéficier les satellites, qui ont une durée de vie en partie limitée par la quantité de cryogène qu'ils portent pour réfrigérer leurs détecteurs. Ces mêmes caractéristiques feraient bénéficier les

détecteurs terrestres ultra-stables, par exemple les cavités laser pour la détection d'ondes gravitationnelles, dont la stabilité est actuellement limitée par les vibrations de leur système de réfrigération. Tous ces problèmes ont plusieurs aspects différents, mais un en commun : ils ne peuvent pas être facilement résolus avec des technologies standards de réfrigération, principalement en raison des difficultés de transport efficace de l'énergie thermique à distance et dans l'espace précis. Comme de nombreuses technologies actuelles reposent ou sont de plus en plus dirigées vers la photonique, la gestion thermique à base de refroidissement par laser peut trouver une utilisation dans un nombre croissant d'applications.

Cette thèse détaille les principaux aspects de la réfrigération optique de la matière condensée, en utilisant plus particulièrement la luminescence anti-Stokes induite par irradiation laser. Elle propose et démontre la solution à deux principales contraintes dans les études de refroidissement laser de matières solides (LICOS), qui sont la possibilité de réaliser cette expérience à l'air ambiant et à la pression atmosphérique, et sa mesure par un capteur de température par contact fiable. Elle propose et étudie également l'utilisation de nouveaux matériaux pour améliorer la technologie pour des applications à grande échelle. La réfrigération d'un solide au moyen d'un laser permet la possibilité d'avoir un dispositif dans lequel la chaleur est extraite de l'endroit même où elle est générée, empêchant ainsi la formation de gradients thermiques indésirables dans les lasers de forte puissance ou les dispositifs miniaturisés. En plus de la possibilité du transport local et précis de chaleur, le refroidissement optique permet également le transport de chaleur à distance, ce qui fait profiter les dispositifs sensibles aux vibrations ou difficile d'accès tels que les capteurs satellites et les cavités laser.

Avant cette étude, toutes les configurations de refroidissement optique ont utilisées des chambres à vide encombrantes, nécessaires pour réduire la charge thermique sur les échantillons optiquement refroidis, afin de permettre l'investigation précise des températures minimales réalisables et sa comparaison avec les prévisions théoriques. Le vide et la nécessité des lasers de pompe de forte puissance, ont été des obstacles dans de nombreuses expériences, en raison du coût et complexité de la configuration optique. Les principales contraintes dans la réalisation du refroidissement optique dans l'air sont le bon dimensionnement de la géométrie de l'échantillon, et la nécessité d'un détecteur de température sensible qui fonctionne dans les conditions de refroidissement par laser, soient sous haute irradiation et pour une large gamme de matériaux. Au cours de ce travail, plusieurs expériences de refroidissement optique ont été réalisées pour la première fois dans l'air à

pression atmosphérique, avec des charges thermiques relativement élevées et utilisant de faibles puissances. La solution emploie l'utilisation d'échantillons suffisamment petits pour éviter la réabsorption de fluorescence et pertes de surface, et assez volumineux pour que les effets de saturation ne deviennent pas préjudiciables au processus de refroidissement.

L'étude de refroidissement optique est intrinsèquement dépendante de la mesure de la température de l'échantillon pompé optiquement. Bien que la mesure de température soit un domaine bien développé, les solutions classiques ont dû être adaptées à l'environnement particulier trouvé dans le LICOS, et ces adaptations ont été un élément permanent de publications sur le LICOS, ainsi que d'une source de nombreux débats depuis le début de cette science. Ici, l'utilisation de réseaux de Bragg sur fibre (FBG) est proposée, démontrée et profondément étudiée pour la mesure de la température dans les expériences du LICOS. En utilisant un capteur en contact transparent, petit et sensible tel qu'un FBG, il est démontré qu'il est possible d'observer le refroidissement optique à des puissances de pompe très faibles, sous charge thermique élevée. Le fait que ce soit un capteur en contact élimine la plupart des problèmes d'interprétation rencontrés avec des techniques sans contact. Les capteurs à FBG ont également été étudiés à température ambiante jusqu'à la température de l'azote liquide, puisqu'une niche d'applications de LICOS est en refroidissement cryogénique. Il est montré pour la première fois que les propriétés des FBGs peuvent être modélisées avec précision, et le capteur montrent une bonne sensibilité aux températures cryogéniques.

Enfin, la recherche de refroidissement laser est concentrée sur les efforts dans la chasse aux matériaux les plus efficaces, principalement des cristaux. Bien que présentant des performances impressionnantes, ces matériaux sont difficiles et coûteux à fabriquer et à manipuler, et sont limités à quelques dopants. Cette thèse présente les études préliminaires sur poudres nanocristallines et les perspectives de refroidissement optique en verre-céramique, qui unissent les propriétés optiques des cristaux avec la production et l'application de masse souhaitable liées aux verres. En plus de l'avancement de la technologie de refroidissement par laser, les techniques développées ici trouvent une application directe dans les lacunes technologiques déjà présentes dans la métrologie optique et la thermométrie à des champs électromagnétiques intenses et à des températures cryogéniques.

ABSTRACT

Most research in refrigeration technologies concentrate in improving the energy efficiency of the energy-hungry refrigerators and air-conditioners, while a small fraction of the research is dedicated to the miniaturization and flexibility. Increased demand for precise tools for general measurement and manufacturing, as well as the generation, processing and transmission of data, push the limits of electronic and photonic devices. These devices require thermal management which is not always possible to achieve with conventional refrigeration methods, due to the need for miniaturization, remote or localized thermal transport, insensitivity to electromagnetic radiation and mechanical vibrations and cryogenic capabilities. One technology that could meet these requirements is optical cooling, where heat is carried away through optical radiation, through an optically-driven process.

Many segments of modern industry, as well as everyday life, are dependent on lasers. This broad dependence has pushed the need for smaller and more powerful lasers for telecommunications, research, military, energy, medical, and display applications, to cite a few. The first bottleneck for power scaling of lasers is due to heat generation, and external thermal management solves only part of the problem since thermal gradients – which produce lensing effects – are still present. Since optical cooling can provide in-situ thermal management, it can be used to remove these deleterious thermal gradients. Currently, the need for energy efficiency is driving lighting technology towards light-emitting diode (LED) lighting. LEDs however suffer from heat generation due to limited light extraction and resistive losses, which severely decrease the lifetime of these semiconductor emitters. Thus they require relatively large heat exchangers, which in turn make miniaturization challenging. Laser cooling could offer a potential solution for heat management in this application as it could for high speed electronics applications and next-generation-computer optical components, in which similar heat management is also needed. Remote, compact and free-of vibration refrigeration provided by optical cooling can benefit satellites, which have the operation lifetime partially determined by the amount of cryogen they carry to refrigerate their detectors. The same characteristics benefit ultra-stable earth-based detectors, for example laser cavities for gravitational wave detection, in which stability is currently limited by the vibrations of their refrigeration system. All these problems have several different aspects, but one in common is that they cannot be readily solved with standard refrigeration technology, mainly due to the difficulties of remote and spatially-specific efficient transport of thermal energy. As many current technologies

rely or are increasingly shifting towards photonics, thermal management based on laser cooling can find use in an increasing number of applications.

This thesis details the main aspects of optical refrigeration of condensed media, more specifically using anti-Stokes luminescence induced by laser irradiation. It also proposes and demonstrates solutions for two main constraints in the studies of laser induced cooling of solids (LICOS), which is the possibility of realizing such experiments in air at atmospheric pressure, and its measurement by a reliable contact temperature sensor. Further, it proposes and studies the use of new materials to push the technology to large scale applications by investigating potentially cheaper materials for its use. The refrigeration of a solid using a laser enables the possibility of having a device in which the heat is removed from the same place where it is generated, thus preventing the formation of unwanted thermal gradients in high-power lasers or miniaturized device. In addition to the possibility of precise, local transport of heat, optical cooling also allows the remote transport of heat, which benefits hard-to-access or vibration sensitive devices such as satellite sensors and laser cavities.

Before this study, all optical cooling setups used cumbersome vacuum chambers. These were required to reduce the heat load on the optically-cooled samples to allow the accurate investigation of the minimum achievable temperatures and its comparison with theoretical predictions. The vacuum and the need of high power pump lasers, has been a hindrance in many experiments, due to the added cost and complexity of the optical setup. The main constraints in the realization of optical cooling in air are the right dimensioning of the suitable geometry of the sample, and the need for a sensitive temperature detector which works under laser cooling conditions, i.e. under high irradiation and for a wide range of materials. In the course of this work, optical cooling experiments were realised for the first time in air at atmospheric pressure, with relatively high thermal loads and using low powers. The solution employs the use of samples small enough to avoid fluorescence reabsorption and surface losses, and large enough so that saturation effects do not become detrimental to the cooling process.

The study of optical cooling is intrinsically dependent on the measurement of the temperature of the optically-pumped sample. While temperature measurement is a well-developed field, the conventional solutions had to be adapted to the particular environment found in LICOS, and these adaptions have been a permanent part of publications on LICOS, as well as a source of considerable

debate since the beginning of this field. Here the use of fiber Bragg gratings (FBGs) for the measurement of temperature in LICOS experiments, is proposed, demonstrated and deeply-studied. By using a transparent, small and sensitive contact sensor such as FBGs, it is shown that it is possible to observe optical cooling with very low pump powers, under high heat load. The fact that it is a contact sensor removes most of the interpretation problems with noncontact techniques. FBG sensors were also studied from room to liquid nitrogen temperatures, since a niche of application of LICOS is in cryogenic cooling. It is shown for the first time that FBGs properties can be accurately modeled, and the sensor shows good sensitivity at cryogenic temperatures.

Finally, laser cooling research has concentrated efforts in the hunt for the most efficient materials, mainly crystals. Although presenting impressive performance, these materials are hard and expensive to fabricate and to handle, and are limited to a few dopants. This thesis presents the preliminary studies on nanocrystalline powders and the prospects of optical cooling in glass-ceramics, which merge the optical properties of crystals with the desirable mass-scalable production and application found in glasses. In addition to the advancement of laser cooling technology, the techniques developed here find direct application in technological gaps previously present in optical metrology and thermometry at intense electromagnetic fields and at cryogenic temperatures.

TABLE OF CONTENTS

LIST OF TABLES

LIST OF FIGURES

LIST OF ABBREVIATIONS

2BDSM	Two-band differential spectral metrology
ASF	Anti-Stokes fluorescence
BBS	Broadband source
BWIMP	Bragg wavelength interrogation by monochromatic power
CCS	Charge-coupled-device spectrometer
CFOM	Cooling figure-of-merit
CLYSiAl	Cadmium, lead, yttrium fluoride and silicon and aluminum oxide
DLT	Differential luminescence thermometry
ECJ	Electronic cold junction
eMFW	External mean fluorescence wavelength
EMR	Electromagnetic radiation
EQE	External quantum efficiency
FBG	Fiber Bragg grating
FIR	Fluorescence intensity ratio
GC	Glass-ceramic
IR	Infra-red
ISp	Integrating sphere
LANL	Los Alamos National Laboratory
LD	Diode laser
LED	Light-emitting diode
LICOS	Laser cooling of solids
LN_2	Liquid nitrogen
MFW	Mean fluorescence wavelength

OREOS	Optical refrigeration of solids
OSA	Optical spectrum analyser
PL	Photoluminescence
PTDS	Photo-thermal deflection spectroscopy
QD	Quantum dot
RBL	Radiation-balanced laser
RE	Rare-earth
RT	Room temperature
RTD	Resistance temperature detector
TC	Thermocouple
TEC	Thermoelectric coolers
Ti:Sapph	Titanium-sapphire
TL	Thermal lens
Yb	Ytterbium
YAG	Yttrium aluminum garnet ($Y_3Al_5O_{12}$)
YLF	Lithium yttrium fluoride ($LiYF_4$)

LIST OF SYMBOLS AND NOTATIONS

A_L	Absorptivity of a sample of length L
A_s	Surface area of the sample
c	Speed of light in vacuum
c_h	Specific heat capacity
C_h	Heat capacity
d	Sample edge dimension
$\bar{E}_f$	Mean energy of the emission
E_g	Energy gap between electronic ground and excited states
f	Focal length
h	Planck's constant
h_{eff}	Overall heat transfer coefficient
h_{cv}	Convective heat transfer coefficient
$\hbar\omega_{max}$	Maximum phonon energy
$I(\lambda)$	Spectral power density
I_p	Pump intensity
I_s	Pump saturation intensity
k	Conductivity of solid link
k_B	Boltzmann constant
k_{NR}	Multiphonon relaxation rate
L	Length of solid link
LNT	Boiling temperature of liquid nitrogen at 1 atm
L_s	Length of the sample

n	Refractive index
N	Total density of active ions
n_i	i-th manifold electron density
P_{abs}	Absorbed optical power
P_{load}	Heat load
P_{cool}	Cooling power
T	Temperature
T_s	Temperature of the sample
T_r	Temperature of the environment
V	Volume
α_b	Background absorption coefficient
α_r	Resonant absorption coefficient
α_T	Total absorption coefficient
γ_R	Radiative decay rate
γ_{NR}	Non-radiative decay rate
ΔT	Temperature difference between the sample and the environment
ε	Emissivity
η_{ext}	External quantum efficiency
η_{cool}	Cooling efficiency
Θ_c	Cooling figure-of-merit
κ_{th}	Thermal coupling constant between the sample and its environment
Λ	Spatial period of refractive index modulation
λ_B	Bragg wavelength

λ_f	External mean fluorescence wavelength
λ_p	Pump wavelength
ξ	Overall thermo-optic coefficient
$\xi(T)$	Bragg wavelength thermal coefficient
ρ	Mass density
σ	Stefan-Boltzmann constant
σ_a	Absorption cross-section
σ_e	Emission cross-section
τ_{eff}	Effective excited-state lifetime
τ_{rad}	Intrinsic radiative lifetime
τ_h	Heating time constant
Φ	Photon flux density
$\Psi_T(T)$	Bragg wavelength temperature sensitivity

CHAPTER 1 INTRODUCTION

1.1 History and literature review

Laser-induced cooling of solids (LICOS) is generally achieved by the extraction of thermal energy from a photoluminescent material through anti-Stokes fluorescence. In this process, the material is excited by a narrow-bandwidth light source whose photons have lower energy than the emitted fluorescence photons. The additional energy in the fluorescence photons is obtained from phonons in the material lattice, thus cooling the material. The higher-energy photons are said to be anti-Stokes shifted, the opposite of the well-known Stokes shift which leads to heat generation. The possibility of using anti-Stokes fluorescence (ASF) for optical cooling was predicted by Pringsheim in 1929 [1], who used a *gedanken experiment* to show that ASF, discovered nine years before, does not need to be accompanied by an equivalent power of Stokes fluorescence, thus a system could be locally cooled by means of optical radiation. The idea of optical cooling seemed to violate the second law of thermodynamics, but this question was settled with the mathematical formulation of the problem by Landau [2], proposing the entropy of the radiation field, and showing that the isotropic, broadband fluorescence [3], has higher entropy than the narrowband and directional pump light.

Optical cooling combines some of the advantages of thermoelectric coolers (TECs), e.g. miniaturization and potential volume production, with those of mechanical coolers, e.g. low temperature limit [4]. In addition, the LICOS scheme can benefit cooling systems that require electromagnetic radiation (EMR) and mechanical insulation, for lightweight cryogenics [4] and in-situ cooling [5]. The former are desirable in space instrumentation, for infra-red (IR) detectors [6] and further substitution of cryogen in long missions. The latter is particularly desirable for mitigating heat production in high-power lasers, which suffer from thermal defocusing and thermal damage. In addition, laser cooling has the potential of recycling un-coupled light of laser diode-to-fiber connections. Also, radiation-balanced lasers, where ASF is used to compensate for the heating due to the quantum defect in the laser, can provide high-power and high-quality beams without the thermal lensing effects [7]. The study of LICOS has gained focus in the laser community in the last decades, and constitutes one of the most important problems of laser physics technology [8].

Pringsheim had predicted that ASF can be present in the absence of Stokes fluorescence, but he had also remarked that the peak of the absorption spectrum of fluorescent materials is always at

higher energies than the peak of the emission spectra [9]. Thus LICOS cannot be performed at an arbitrarily long wavelength pump and practical anti-Stokes shifts are of the order of $k_B T$, the product of the Boltzmann constant, k_B and the temperature of the material, T. Since the thermal energy per cooling cycle extracted from the material lattice is very small, in order for cooling to occur it is necessary to have a fluorescence quantum efficiency of nearly 100%. The idea of using rare-earth (RE) doped matrices for observing anti-Stokes cooling was first proposed in 1950 by Kastler [10], who pointed out the high quantum efficiency of such materials, as well as the remarkable Zeeman and Stark level splitting which can be observed in them. In the same work, despite recognising the difficulties of the experimental realization and observation of LICOS, Kastler pointed out that proper design with the use of selective coatings would improve system cooling. Some other optimized designs have been proposed for achieving maximum temperature drop, by minimizing heat transport using fibre optic supports [11], and coated walls of the holder [11, 12]. The quest for a maximum temperature drop focuses on the insulation of the cooled sample and the fluorescence escape efficiency, and since extracted heat corresponds to only a small fraction of the energy of fluorescence photons, the efficiency of a typical optical cooler is relatively small. The main loss mechanism in that approach is the escaping fluorescence, which can be recycled and used to feed the refrigerator pump source, or to perform a secondary function, e.g. illumination. It has been shown that, when using photon waste recycling, an optical cooler can present a Carnot-limited efficiency given by the temperature of the cooler and the fluorescence absorber [13].

Initial evidence of anti-Stokes refrigeration in condensed media was observed in an electrical pumped semiconductor diode in 1964 [14], which did not show bulk cooling, believed to be due to the low photon escape efficiency – a problem still present in these materials. Four years later, evidence of reduced optical heating in a rare-earth doped crystal was reported [15], although no bulk cooling was achieved. Surprisingly only a decade later, Doppler laser cooling of gases was proposed [16], which opened a whole new field of research. Doppler cooling however reduces the temperature of the atoms by reducing their translational motion, thus is not applicable to atoms in a solid – which are trapped in a lattice. A few years after the proposition of Doppler cooling, the first demonstration of anti-Stokes cooling in gases was demonstrated [17], and the efficiency of the process suggested that one could use this phenomenum to refrigerate condensed matter. While

evidence of anti-Stokes refrigeration in liquids was reported in 1994 [18], optical cooling of solids remained elusive until 1995.

Experimental demonstration of LICOS was first realised in 1995 by Epstein *et al.* [19] at the Los Alamos National Laboratory (LANL), cooling a Yb^{3+}:ZBLANP glass by 0.3K from room-temperature (RT). Subsequent work demonstrated optical cooling using other dopants, and in 2000, Bowman [20] demonstrated cooling in a ytterbium-doped crystal for the first time. In the following year Epstein demonstrated cooling of the important laser host ytterbium-doped yttrium aluminum garnet, $Y_3Al_5O_{12}$ (Yb:YAG).

The lowest temperature record achieved in ZBLANP glass was obtained in 2005 by the LANL team, cooling the sample to 208K [21], starting at room temperature. A considerable effort was dedicated in the purification of the glasses, but cryogenic cooling regime was not attained. As the temperature drops, the long wavelength tail of the absorption coefficient decreases. Since in crystals inhomogeneous broadening is small, relatively high absorption coefficients are found in narrow spectral ranges and can therefore allow optical cooling at lower temperatures than in glasses. The first demonstration of cooling of a ytterbium-doped fluoride crystal was reported in 2006 [22, 23], and then Yb^{3+}:$LiYF_4$ was optically cooled in 2007 by the same group [24], opening possibility of cryogenic optical cooling. In April 2009, Seletskiy *et al.* [12] achieved the record-breaking temperature of 155 K (surpassing TECs) starting from ambient, using fluorescence up-conversion, in a sample of 5 wt. % Yb^{3+}:$LiYF_4$ crystal, in a resonant cavity enhanced approach, pumped by a diode-pumped Yb:YAG disk laser, operating at 1023 nm. This experiment also achieved the record of maximum cooling power of 110 mW [25]. The principal improvement in their approach was to use a high-purity crystal host. Crystals have long range order, so that the homogeneous broadening preserves the oscillator strength of the transitions, enhancing resonant absorption. In addition, the high purity decreases background absorption. In that experiment, the limiting factor for further cooling was the pump minimum wavelength of 1023 nm. In an experiment in 2011, the Los Alamos group reported local cooling in a 5% Yb^{3+}:$LiYF_4$ sample to 110 K at 1020 nm [26, 27]. They also presented a novel temperature measurement technique of two-band differential spectral metrology [28] (2B-DSM), showing a resolution down to 250 μK after averaging. The most recent record low temperature was achieved in a 10 % Yb:$LiYF_4$ crystal, optically cooled down to 93 K, a result of further purification of the material [29]. A discussion of the expected minimum achievable temperature as a function of the purity level of the samples is

presented in [30], showing that an improvement by a factor of 23 in the background absorption of the sample cooled down to 110 K would allow it to be cooled down to 60 K.

Research in laser cooling was limited to a handful of facilities in the world. Not only the materials and lasers are very specific, but the experimental conditions and temperature measurement needed bulky chambers and systems. New temperature measurement techniques for laser cooling experiments continued to emerge in order to adapt for the specifities of novel samples. A broadly applicable solution would be the use of a transparent, direct temperature sensor, such as a fiber Bragg grating, which was proposed in 2010 by Soares de Lima Filho *et al.* [31, 32] and also demonstrated for use in optical cooling in 2013 [33]. Another step towards the simplification of laser cooling research – and therefore its applicability as well – is to achieve optical refrigeration at ambient pressure, which was demonstrated for the first time in 2013 by Soares de Lima Filho *et al.* [34], obtaining a similar temperature drop to that achieved previously in vacuum for a similar sample and pump power. Other groups followed suit, performing optical cooling in air with low optical powers [35-37].

Another extension of LICOS is the production of lasers without internal heat generation, also known as the radiation-balanced laser (RBL), proposed in 1999 by Bowman [38] for bulk lasers. This technique consists of a laser whose heat generation is compensated for by anti-Stokes cooling at each point in the material. The realization imposes strict conditions on the laser material, operating wavelengths and powers. A comprehensive work on the metrics for choosing optimal materials for RBL is described in [39]. Another laser scheme which mitigates heat generation is the self-cooled laser, which has the same principle of the RBL, but the lasing and cooling take place in two different systems of ions in the same host [40]. The basic idea of the RBL and the self-cooled laser were extended to fibre lasers [5, 41-44] and Raman fibre amplifiers by Nemova and Kashyap [45], separating the cooling process from the lasing process, as an integrated optical cooler. The first radiatively cooled laser was demonstrated by Bowman [46] in 2002, in a Yb:KGW slab pumped at 992 nm and lasing at 1050 nm. In 2010, Bowman [47] demonstrated a near-RBL in Yb:YAG with 372 W of pump power at a wavelength of 1030 nm and lasing at 1050 nm with 70 W of output power. In that work, cooling by fluorescence at 1010 nm wavelength compensated for the 2 % laser quantum defect, reducing thermal loads to below 0.01 % of the output laser power. Theoretical predictions show that semiconductors may be better cooling materials than ion-doped solid dielectrics, but no success in bulk cooling has been achieved as yet in mesoscopic scale,

although extensive work has been done on the subject [13, 48-54]. The main issues are fluorescence trapping due to the high refractive indexes of semiconductors, and non-radiative recombination [55]. In 2013, Zhang *et al.* [56, 57] demonstrated for the first time bulk cooling of semiconductor nanostructures, achieving a 40 K temperature drop in CdS nanobelts of 110 nm thickness, pumped at 514 nm. As for larger semiconductor devices, although no direct cooling has been observed to date, one can optically cool them indirectly, as was demonstrated when cooling a semiconductor heat load down to 165K [58].

Another approach of cooling a semiconductor is combining it with a conventional RE-refrigerator. This integration allows one to produce another type of self-cooled laser, in which one cools a diode laser (LD) using part of the optical power from the laser to induce anti-Stokes cooling of an optical refrigerator thermally coupled to it. The optical refrigerator in this case is a doped crystal or glass which has a quantum defect larger than the quantum defect of the LD. Alternatively, one can use a single source to provide the pumping of both LD and refrigerator. A LD with an integrated optical cooler would provide stable temperature and consequently stable optical properties. As a typical LD heats up, its wavelength and gain is red-shifted [59], which can be used with an all-optical feedback control loop for the optical cooler, replacing the complex electrical thermal management system present in most telecommunication lasers. Typical LD-to-fiber losses of direct coupling in telecommunication are from -7 dB to -13 dB, and -1.5 dB for a good lens-aided coupling [60]. Such wasted optical power could be used to harvest heat by the use of an integrated optical cooler, substituting TECs and replacing large thermal sinks by small footprint waveguides. Such indirect thermal energy delivery allows an all-optical operation of LDs, which can be beneficial for space and telecommunication applications.

If cryogenically operated, it is possible to have low noise, higher quantum efficiency [61] and also more efficient heat removal can be achieved [62], enhancing beam quality for higher power scaling. Optical cryocoolers are strong candidates for substituting current spacecraft cryogenic technologies [6], substituting large radiators, vibrating mechanical pumps and increasing mission length by substituting cryogens needs. Recent studies show that such characteristics are also desirable for earth-based applications such as to fluidless-refrigeration of ultrastable silicon cavities, which can improve the frequency stability of these state-of-the-art cavities by a factor 10, being limited by Brownian noise.

Novel schemes of optical cooling continue to appear. Optical cooling could be enhanced through the use of superradiance for enhancing the radiative decay rate, as suggested by Andrianov in 1997 [63], and several similar approaches were studied [8, 40, 64-71], although no experimental demonstration has been reported so far. A group has proposed the radiative cooling of a cavity quantum electrodynamics system [72], and optomechanical cooling of a cavity membrane was demonstrated [73]. The induced radiative cooling of a semiconductor was demonstrated [74] by photon down-conversion, and the cooling of an active load was performed [75] in an InGaN LED optically cooled by 5 K from 450 K. However in this case the thermal energy is extracted in the form of thermal radiation [75-77], which makes the applications far more limited than anti-Stokes cooling. Contrary to mainstream strategy of enhancing cooling by material ultra-purification, it has been shown that certain impurities can help optical refrigeration to take place [78], which possibly is due to loss quenching rather than enabling new transitions to occur – as it has been suggested. Optical cooling in trapped single nanocrystals [79], as well as in Nd-doped [80-82] and Er-doped [83] nanocrystalline powders was demonstrated, and our group investigated the possibility of using ytterbium-doped nanocrystalline powders [84]. Single nanocrystals were cooled in water by another group [79], constituting the first experimental demonstration of cold-Brownian motion of nanoparticles in condensed media. Recently, studies of glass-ceramics for their potential in laser cooling reported by Soares de Lima Filho *et al.* [85-87], indicate how the desirable properties of crystals may be preserved in more easily available and flexible materials.

1.2 Objectives of this work

The objective of this work is to bridge the gap between the science of optical cooling and its implementation in real-world systems. Initially, the goal of the thesis was to cool a semiconductor laser chip using an optical refrigerator, powered by the same optical source as the laser. This would be a proof-of-concept of using optical refrigeration for thermal control of the ubiquitous solid-state laser, demonstrating a practical use of the technique. The concept, although simple, demonstrates a device in which its information (signal laser), power (refrigeration and laser excitation) and waste (thermal energy carried away) are transported completely by optical means. Some spin-offs are immediate: fully optical device integration, thermal management of remote devices (diode lasers, space-borne detectors). However the implementation of such a concept, which been the target of several groups, involves multiple, difficult problems. The solution to all these problems in a single

PhD work is unrealistic with the present state-of-the-art. It turns out that the optical cooling technology has more tractable, but timely significant challenges than this initial goal, and it would benefit more from the studies presented in this thesis: the exploration of new materials, sensing techniques and the realization of optical cooling at normal conditions of temperature and pressure. These would largely increase the pool of possible experiments on LICOS, keeping up with simplicity and reliability.

Due to specific goals – e.g. achieving record low temperatures – the mainstream materials research for LICOS has concentrated efforts on the purification of bulk fluoride glasses and crystals, and in the increase of the pump absorption. The studies of new materials such as glass-ceramics, quantum dots (QDs) and nanocrystals open the application of LICOS, for example the cooling of glass ceramics (GCs) enables LICOS on GC lasers and free-form devices and probes. Optical cooling on quantum dots allow the use of new pump wavelengths, thus widening the choice of pump wavelengths, as well as the media in which cooling take place. The use of GCs and nanocrystals means that optical cooling can be integrated into systems widely used as lasers, sensors and biomarkers, to cite a few.

At the start of LICOS experimental research, the optical cooling signals were typically low, the wavelength of transition between heating and cooling was not clear, and some results were not conclusive, or were subjects of heated debates. Therefore, an essential feature of LICOS experiments was a minimum heat load on the optically cooled sample, and that included the use of high vacuum systems. Vacuum for realization of optical cooling is not a fundamental need, and the technology is mature enough to produce and detect LICOS without it. Thus, the goal of performing LICOS at ambient pressure, which would simplify LICOS experiments, allows the focus to shift to laser science rather than vacuum technology. The time and monetary resources which are saved with this currently simple approach are significant.

The aforementioned small or ambiguous signals create a new problem for the experimenter: the temperature measurement *per se*. In addition to that, the particular conditions found in LICOS experiments limit the thermometric methods which can be utilized. Since the first experimental demonstration of LICOS, a significant part of the research in the field was dedicated to the study of these methods. Thus a major goal in this Thesis was to study and develop a reliable method for temperature measurements for LICOS experiments. Generally desirable properties for

thermometric methods are accuracy, sensitivity and inertness – in this case small thermal mass. In LICOS experiments, inertness also means transparency, since intense fluorescence must leave the material. As it will be discussed in the Thesis, noncontact measurements have several drawbacks other than signal interpretation. The use of an ultra-transparent, contact temperature sensor, based on fiber Bragg gratings (FBGs) is proposed and demonstrated in this Thesis. FBGs, as well as LICOS-systems, are immune to electromagnetic noise and are lightweight. Thus, this sensor can be readily integrated in many current LICOS experiments, and should be compatible with future LICOS-devices.

The three aforementioned goals should greatly help future exploration for LICOS, as well as the applicability of the technology. An important sequel is the thermally-independent power scaling of lasers, which would directly benefit the scope of the high-power laser applications. The development of the optical refrigeration technology would ultimately lead to a "reverse-microwave" device, a future-generation appliance in which the optical cooling of large thermal loads is possible, in a historical parallel to the development of the once unthinkable idea of using the Seebeck effect to refrigerate beer in a portable manner.

1.3 Thesis outline

In Chapter 2 the theoretical background behind the experiments on laser-induced cooling of solids (LICOS) is presented. The basics of optical refrigeration are presented and generalized in the section 2.1.1. In the subsequent section, the principal aspects of LICOS with rare-earth-doped solids, which have been the only type of materials so far to show bulk optical refrigeration are discusses. The specific case of Ytterbium-doped YAG, as a general example of Ytterbium-doped crystals as an important material for LICOS is presented. The chapter is concluded with a section on heat transfer, essential for experiments on optical refrigeration, and for completing the basic background for the understanding of this Thesis.

The optical methods for the characterization of materials for LICOS are presented in the Chapter 3. The basic instruments used for the characterization, as are used in the experiments are presented and discussed. The Chapter 3 also starts with fundamental but well-known techniques such as resonant absorption and fluorescence spectroscopy, and finishes with the characterization of a very important parameter in LICOS, the quantum efficiency. The latter measurements, although

important, can be redundant and serve mainly as validating techniques. Since material parameters limit the quantum efficiency achievable, its values appear very explicitly in the final optical cooling measurements. In the first half of the chapter, photoluminescence (PL) spectroscopy, mainly the spectra (3.2.1) and excited state lifetime (3.2.2) are studied. Both traditional systems, as well as tailored systems, designed for specific experimental conditions such as photoluminescence under in-band pumping or in highly scattering materials (3.2.1.1) are discussed in detail. Measurements peculiar to small or hard-to-access samples (3.2.1.2), and spatial-dependent PL spectroscopy (3.2.1.3) are then discussed.

The second half of Chapter 3 is dedicated to the experimental setups used for the determination of the quantum efficiency. Section 3.3 presents the widely utilized, absolute but often inaccurate method of photoluminescence quantum yield by the use of an Ulbricht or integrating sphere (ISp), and the approach used in this Thesis to quantify and minimize the common errors on this measurement.

In the Chapter 4 an in depth discussion on how optical refrigeration is typically measured, along with the main advantages and drawback of each technique is presented and a few examples are given. In the light of the previous sensors analysis, the use of a fiber Bragg grating as an ideal sensor for optical refrigeration is proposed for the first time, solving the main limitations of the previous techniques. In the second part (4.2) the fabrication, characterization, use and modeling of the proposed FBG at room temperature are described and discussed, as well as for the low temperatures that optical refrigeration is expected to reach.

The Chapter 5 presents the thermal design of the main experiment, the model utilized to interpret the data, and the errors associated with it. In the second part the characterization of the Yb:YAG sample and the complete setup for optical cooling is shown, as well as the first measurement of optical cooling performed in this work, as well as the first “in air at atmospheric pressure”. The novel use of a FBG temperature sensor to measure very small background absorption coefficients is presented in the section 5.2.2. The following section demonstrates and discusses the optimization of the experiment, which could allow the cooled crystal to achieve temperatures comparable to those achieved in vacuum. Also, further optimization is suggested based on the obtained results. The final part of the chapter shows a solid thermal load being cooled by the optically-cooled crystal, in a proof-of-concept of a optical refrigerator.

After the realization of the main objectives, further studies were conducted in order to find more accessible and flexible samples which could be optically-cooled, and are discussed in the Chapter 6. The first half of the chapter concerns the preliminary investigations on the cooling potential of nanocrystalline powders. These investigations were limited to spectroscopic studies. The second part concerns the cooling/heating experiments of ytterbium-doped glasses and glass-ceramics, which were done for the first time. The samples had their structural, thermal and photo-physical properties measured, and then their cooling figure of merit was measured in a calorimetric experiment. Although the present glasses and glass-ceramics did not show cooling, indications are that glass-ceramics can be optically-refrigerated, with purer samples.

Finally to conclude the Thesis, a summary of the main accomplishments, as well as the impact they have in the laser cooling science is given. The conclusion also highlights some of the contributions this work has made to other fields of research. A brief discussion and recommendations for the continuation of the present work, as well as for the laser cooling science as a whole, completes this Thesis.

CHAPTER 2 THEORETICAL BACKGROUND

2.1 Optical refrigeration

2.1.1 Basics of optical refrigeration

There are several proposed approaches for achieving optical cooling, and the particular cases will be described in this chapter. Without loss of generality, the cooling power, or the power which is extracted from a sample by optical means – excluding blackbody radiation – is given by the difference between the optical power which leaves the sample and the optical power that enters the sample, and can be expressed by (2.1) [48], without considering explicitly radiation trapping or reabsorption.

$$P_{\text{cool}}(\lambda_p) = P_{\text{abs}}(\lambda_p)\left(\eta_{\text{ext}}\frac{\alpha_r(\lambda_p)}{\alpha_r(\lambda_p)+\alpha_b}\frac{\lambda_p}{\lambda_f}-1\right), \tag{2.1}$$

where P_{abs}, α_{r}, η_{ext}, α_{b}, λ_{p} and λ_{f} are respectively, the absorbed optical power, resonant absorption coefficient, external quantum efficiency (EQE), background absorption coefficient, the pump and the emission wavelengths. Resonant absorption is one which leads to the excitation of an electron of the ion of interest in the cooling process, while background absorption accounts for all unwanted absorption, including the excitation by impurities which do not participate in the cooling process. The first two terms of the product in parentheses is the fraction of absorbed photons, which generate an escaped fluorescence photon, multiplied by the ratio of the mean energy of the fluorescence photons to the energy of the pump photons. Notice that this expression is still valid for a lossless ($\alpha_{\text{b}} = 0$) electrically-pumped device, by acknowledging that λ_{p} is the wavelength associated to the energy of the excitation, with P_{abs} as the product of the forward bias current and the applied voltage, and has been used in this form since early years of studies of electroluminescent cooling [88]. The emitted photons follow a spectral distribution, thus their wavelength is not unique but λ_{f} can be defined as the mean fluorescence wavelength, the wavelength associated to the mean photon energy of the emission, $\bar{E}_{\text{f}}$.

$$\bar{E}_{\text{f}} = h\bar{\nu}_{\text{f}} = h\frac{\int \nu\Phi_{\text{f}}(\nu)d\nu}{\int \Phi_{\text{f}}(\nu)d\nu}, \tag{2.2}$$

where Φ_f is the fluorescence photon flux spectral density and h is the Planck constant. The measured quantity in a typical optical spectrum analyser is the spectral power density $I(\lambda)$, which in a spectral window $d\lambda$, corresponds to a power $dP(\lambda) = I(\lambda)d\lambda$. The collected power by the instrument can be also related to the total photon flux $\Phi(\lambda)d\lambda$ or $\Phi(\nu)d\nu$, by multiplying it by the energy of each photon hc/λ, c being the speed of light in vacuum, which allows therefore the calculation of $\bar{E}_f$ (2.3).

$$\begin{aligned} dP(\lambda) &= I(\lambda)d\lambda = \frac{hc}{\lambda}\Phi(\lambda)d\lambda = \frac{hc}{\lambda}\Phi(\nu)d\nu, \\ \Rightarrow \Phi(\nu)d\nu &= \frac{\lambda}{hc}I(\lambda)d\lambda, \\ \Rightarrow \bar{E}_f &= h\frac{\int \frac{c}{\lambda}\frac{\lambda}{hc}I_f(\lambda)d\lambda}{\int \frac{\lambda}{hc}I_f(\lambda)d\lambda} = hc\frac{\int I_f(\lambda)d\lambda}{\int \lambda I_f(\lambda)d\lambda}. \end{aligned} \tag{2.3}$$

Thus the wavelength associated with the mean photon energy of the emission, which is $\lambda_f = hc/\bar{E}_f$ can be written as (2.4).

$$\lambda_f = \frac{\int \lambda I_f(\lambda)d\lambda}{\int I_f(\lambda)d\lambda}, \tag{2.4}$$

where $I_f(\lambda)$ is the spectral power density of the measured fluorescence [89]. A simplified diagram of the optical cooling process described by Eq. (2.1) is shown in Figure 2-1, where photons entering the material can undergo different processes, such as nonresonant absorption, excitation of an electron, thermalization and subsequent decay, radiatively as anti-Stokes photons, or nonradiatively in which case, the material absorbs several phonons and warms up locally. The emitted photon can escape the material, or get trapped and be subject to the same processes as the incoming photon. The excited or decayed electron is then thermalized, where phonons are annihilated leading to a local cooling of the bulk sample. If the nonresonant absorption and the multiphonon decay are sufficiently suppressed, the bulk material cools.

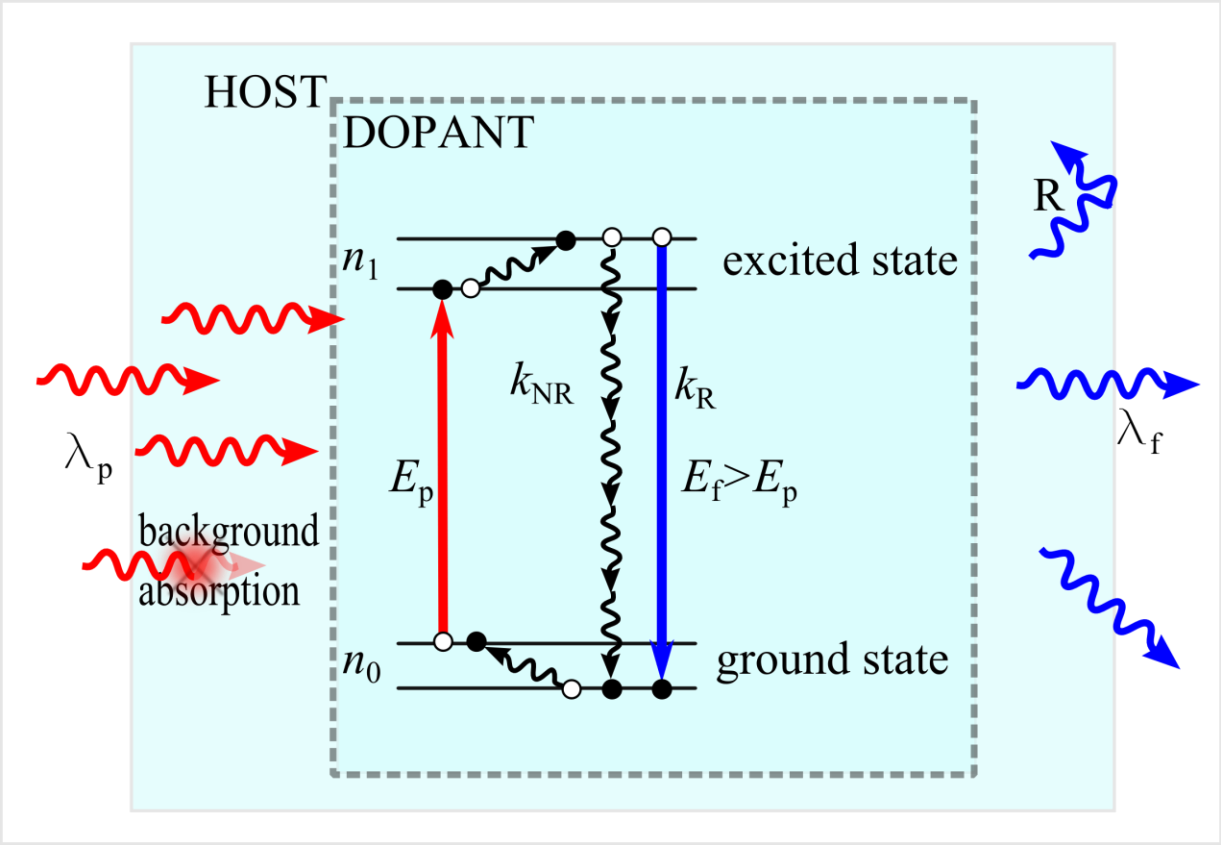

Figure 2-1: Simplified diagram of the optical cooling process upon absorption of a photon and emission of a blue-shifted photon. Also shown are the most important processes which can occur within the material. Incoming photons of wavelength λ_p (red arrows) enter the host material, and some of them can suffer multiple scattering and be absorbed in unwanted impurities (background absorption). The remaining photons interact with the dopant ion, exciting electrons from the ground manifold n_0 to the excited manifold n_1, where they are thermalized within the manifold. The electrons in n_1 return to the ground state by a nonradiative path through multiphonon (black arrows) relaxations at a rate k_{NR}, or by a radiative path, i.e. emitting photons at a rate k_R (blue line). The emitted photons (blue arrows) of wavelength λ_f can escape the material, or can be trapped as well and reabsorbed in the sample volume or reflected (R) at the surface. The electrons undergo thermalization, absorbing phonons from the lattice, and end up at a sublevel (horizontal lines) following a Boltzmann distribution. The emitted photons, as well as the reflected ones, can undergo all the same processes as the incoming photons.

It is practical to define a theoretical cooling efficiency in a material at a given pump wavelength as the ability of conversion of the absorbed power into heat lift or cooling power:

$$\eta_{\text{cool}}(\lambda_p) = \frac{P_{\text{cool}}(\lambda_p)}{P_{\text{abs}}(\lambda_p)} = \eta_{\text{ext}} \frac{\alpha_r(\lambda_p)}{\alpha_r(\lambda_p)+\alpha_b} \frac{\lambda_p}{\lambda_f} - 1. \tag{2.5}$$

In optical refrigeration experiments, the main quantities are the temperature change ΔT and the pump power, P_{p}. The temperature change is related to the cooling power and the heat load, and its maximum amplitude, ΔT_{max} is directly proportional to P_{cool}, for small values of ΔT. Also, for small values of P_{p}, the absorbed pump power is directly proportional to the pump power. Thus the experimental quantity $\Delta T_{\text{max}}/P_{\text{p}}$ is related to the cooling efficiency by Eq. (2.6).

$$\frac{\Delta T_{\text{max}}(\lambda_{\text{p}})}{P_{\text{p}}(\lambda_{\text{p}})} = \frac{P_{\text{cool}}(\lambda_{\text{p}})}{\kappa_{\text{th}}} \frac{\left(1-e^{-\alpha_{\text{T}}(\lambda_{\text{p}})L_{\text{s}}}\right)}{P_{\text{abs}}(\lambda_{\text{p}})} = \frac{A_{\text{L}}}{\kappa_{\text{th}}} \eta_{\text{cool}}(\lambda_{\text{p}}), \tag{2.6}$$

where κ_{th}, L_{s}, A_{L} are, respectively, the sample-environment thermal coupling constant, the sample length and its corresponding absorbance $(1 - \exp(-\alpha_{\text{T}}L_{\text{s}}))$, and $\alpha_{\text{T}} = \alpha_{\text{r}} + \alpha_{\text{b}}$. Although η_{cool} is a good measure of the efficiency of the cooling process in a given material, most of the time one is interested in knowing how much heat lift a sample can provide for a given pump power. Also (2.5) indicates that the cooling efficiency increases with the increase in the pump wavelength, but since the absorption coefficient drops in the long wavelength tail, increasing the pump wavelength is not always a good strategy to achieve maximum cooling power. While Eq. (2.5) is representative of the material and Eq. (2.6) can be readily used with experiments, it is convenient to define a cooling figure of merit Θ_{c} , Eq. (2.7) that is used easily in theoretical predictions as well as in the experimental analysis of the data.

$$\Theta_{\text{c}}(\lambda_{\text{p}}) = \frac{P_{\text{cool}}(\lambda_p)}{P_{\text{p}}(\lambda_p)} = A_{\text{L}}\eta_{\text{cool}}(\lambda_{\text{p}}) = \kappa_{\text{th}} \frac{\Delta T_{\text{max}}(\lambda_{\text{p}})}{P_{\text{p}}(\lambda_{\text{p}})}. \tag{2.7}$$

2.1.2 Optical cooling with rare-earth-doped solids

Rare-earth elements are divided in two groups in the periodic table: the lantanides and the actinides. The actinides are of less importance in lasers than the lantanides, due to the instability of the former, and they will not be discussed here. The more stable form of the lanthanides in condensed matter is in the trivalent level of ionization. They are characterized by the electronic configuration

[Xe]$4f^{12}6s^2$, with the outer shell configuration $5s^25p^66s^2$. As a result of the lanthanide contraction (the 4*f* electrons become increasingly more tightly bound with increasing atomic number *Z*), the 4*f* wavefunctions lie within the closed $5s^25p^6$ xenon shell, which shields the 4*f* electrons from the environment [90]. This results in a free-ion-like behaviour of the lanthanides in condensed matter, which make their optical behaviour highly predictable. Usually the lanthanides are incorporated in ionic crystals as trivalent ions, with electron configuration [Xe]$(4f)^{n+x-1}$. In the case of ytterbium, $x = 0$ and $n = 14$. The 5*s* and 5*p* shells are completely filled, thus the 4*f* states are well shielded, and therefore present narrow transition linewidths and show low variation in different environments. The manifolds can be labeled as $^{(2S+1)}L$, where *S* is the total spin and *L* the uppercase letter corresponding to the orbital angular momentum $l = 0, 1, 2, 3, 4\ldots$ for the orbitals *s, p, d, f,* g, … [91]. The energy levels are degenerated, and as the degeneracy is broken, additional quantum numbers are added to the energy level representation.

The energy level of a free ion can be calculated by solving the Schrödinger equation using the system Hamiltonian, constituting of a central field Hamiltonian H_0, and perturbation terms to account for Coulomb interaction H_{ee} and the spin-orbit coupling of the elections H_{so} [92]. H_0 is the sum of kinetic and potential energy of the *N* electrons:

$$H_0 = \sum_{i=1}^{N}\left(-\frac{\hbar^2}{2m_e}\nabla_i^2 + V(\mathrm{r}_i)\right), \tag{2.8}$$

where m_e is the electron mass and r_i the position of the *i*-th electron. The solution of the time-independent Schrödinger equation $H_0\Psi_0 = E_0\Psi_0$ is the product of single-electron wave functions:

$$\Psi_0 = \prod_{i=1}^{N}\left|n_i l_i m_l m_s\right\rangle, \tag{2.9}$$

where n_i, l_i, m_l and m_s are respectively the principal quantum number, the orbital angular momentum, and the degenerate magnetic and spin quantum numbers.

The Coulomb interaction between electrons can be expressed as the operator:

$$H_{ee} = \sum_{i<j=1}^{N}\frac{e^2}{4\pi\varepsilon_0\left|\mathbf{r}_i - \mathbf{r}_j\right|} - \sum_{i=1}^{N}\left(\frac{Ze^2}{4\pi\varepsilon_0 r_i} - V(r_i)\right), \tag{2.10}$$

Where *e*, ε_0 and *Z* are the electron charge, the vacuum permittivity and the atomic number, respectively. Electron-electron interaction causes splitting of the 4*f* states, in distinct *LS* levels.

Yb^{3+} has the electronic configuration [Xe]$4f^{13}$, i.e. almost a closed 4*f* shell, with a 4*f* hole of spin ½ , producing a ^{2}F manifold. This manifold is split due to the spin-orbit interaction, described by the operator:

$$H_{so} = -\sum_{i=1}^{N} \frac{1}{2m_e{}^2 c_0^2} \frac{1}{r_i} \frac{dV(r_i)}{dr_i} \mathbf{l_i} \cdot \mathbf{s_i}, \tag{2.11}$$

where c_0, $\mathbf{l}_i$ and $\mathbf{s}_i$ are respectively the speed of light in vacuum, the orbital angular momentum vector and the spin vector [93]. The spin-orbit coupling introduces a total angular momentum $J = |L + S|, \ldots, J = |L - S|$, where L and S are the total orbital angular momentum and the total spin. The *LS* levels are therefore split into *J*-manifolds. In the case of Yb^{3+}, which has $s = ½$ and $L = 3$, the spin-orbit coupling produces two manifolds $^2F_{7/2}$ and $^2F_{5/2}$. These two manifolds are separated by an energy gap $E_{LS} = \zeta(l + ½) = 7/2\ \zeta$, where ζ is the spin-orbit coupling parameter, which has value of 2918 cm^{-1} for the Yb^{3+} free ion [94]. Therefore, the $^2F_{7/2}$ and $^2F_{5/2}$ manifolds are separated by an energy gap of ~ 10213 cm^{-1}.

When the ion is embedded in a solid matrix, its electrons will be subject to an additional electrical field, and their energy levels will differ from those of the free-ion case. Therefore an additional perturbation to the Hamiltonian should be considered [94], due to the electrostatic crystal-field potential:

$$H_{cf} = \sum_{k,q} B_q^k C_q^{(k)}, \tag{2.12}$$

where $C_q^{(k)}$ are tensor operators and B_q^k are adjustable parameters, determined empirically from experiment. The crystal-field lifts the M_J-degeneracy of the $^{2S+1}L_J$ manifolds, and is called Stark splitting. Manifolds with odd number of electrons are split into $(2J + 1)/2$ Stark levels, while even-numbered manifolds split into $(2J + 1)$ Stark levels. Therefore Yb^{3+} is expected to have a ground manifold with 4 Stark levels and the $^2F_{5/2}$ manifold, referred to as the excited state, with 3 Stark levels. In the case of trivalent ytterbium, the determination of H_{cf} is difficult, since it has only two 4*f* multiplets [94], therefore not enough information can be obtained from spectroscopic measurements – 4 transitions in absorption and 3 in emission – to deduce the up to 27 empirical parameters required for the determination of B_q^k [95]. The position of energy levels are thus assigned directly from measurements. The Stark splitting is of the order of, respectively 400 cm^{-1} and 750 cm^{-1} for Yb^{3+}-doped $YLiF_4$ and $Y_3Al_5O_{12}$ crystals [96].

The strength of a transition between two states $|L, S, J, M_J\rangle_{i\to j}$ is given by Eq. (2.13) [97].

$$S_{i\to j} = \left|\langle i|\boldsymbol{\mu}|j\rangle\right|^2 = \left|\langle i|\boldsymbol{\mu}_{\mathrm{e}}|j\rangle\right|^2 + \left|\langle i|\boldsymbol{\mu}_{\mathrm{m}}|j\rangle\right|^2, \tag{2.13}$$

where $\boldsymbol{\mu}_{\mathrm{e}} = \sum e\boldsymbol{r}_i$ and $\boldsymbol{\mu}_{\mathrm{m}} = (\boldsymbol{L}+2\boldsymbol{S})e\hbar/(2c_0m_{\mathrm{e}})$ are the electric and magnetic dipole moments due to all 4*f* electrons. Transitions between states of same parity are forbidden due to the selection rules for the electric dipole moment, however they are observed due to the crystal-field admixing of states of opposite parity, in noncentrosymetric crystal fields [98]. The 4*f* states have the same parity, with $l = 3$. The electron in the 5*d* shell, above the 4*f* shell, have $l = 2$, therefore different parity to *f* electrons. Thus, the strength of the transition is ultimately determined by the strength of the crystal field responsible for generating the admixing of states. In practice the crystal field theory is only qualitative and still cumbersome to be attractive. In order to describe the transitions between electronic *f-f* states of rare-earths, one can use the Judd-Ofelt theory [92], which also requires knowledge of experimental cross-section data. The strength of the transition is then expressed by the sum of the products of the phenomenological Judd-Ofelt intensity parameters Ω_i times the squared matrix elements of the unit tensor operators between the initial and final states [99]. With the knowledge of Ω_i, one can calculate the strength of any absorption or emission transition, the fluorescence branching ratio from *J* to *J'*, and the radiative lifetime of the excited state. As with the crystal-field determination, Judd-Ofelt is not useful for Yb^{3+} [92], due to the few transitions presents in this ion. The contribution from each sublevel to the total radiative transitions is given by the branching ratio, which can in practise be extracted from the relative intensities of the experimental photoluminescence spectrum of the material under analysis. The inverse of the ratio of the radiative lifetime and the measured fluorescence lifetime is the quantum efficiency η_{e}. The major limits to η_{e} are due to nonradiative relaxations, which can be multiphonon relaxations, cross relaxations or cooperative upconversion processes. Multiphonon relaxations corresponds to the decay of an excited electron with the emission of phonons. The probability of this decay is given by a simple energy gap model [100].

Another factor which prevents the cooling efficiency to be higher is the small value of the energy gaps within a manifold due to generally small crystal-field splitting [94]. As one can see from a first glance at Eq. (2.5), the cooling efficiency increases if one is allowed to use longer pump wavelengths or shorter mean fluorescence wavelength, which in a first instance can be achieved through an increase in the crystal-field splitting. While this is generally true, e.g. for Yb^{3+}:fluorides

at room temperature [101], at low temperatures a smaller splitting may be beneficial since the sublevels are easier to populate. The population of higher levels is important for increasing the absorption at longer wavelengths but at the same time it decreases the mean fluorescence wavelength, due to the higher energy levels of the excited-state manifold.

An alternative way to obtain higher cooling efficiencies is by using a system in which the practical ratio λ_p/λ_f is high. Let us consider the ideal cooling efficiency (2.14), which is Eq. (2.5) with $\eta_{ext} = 1$ and with $\alpha_b = 0$.

$$\eta_{cool,ideal}(\lambda_p) = \frac{\lambda_p}{\lambda_f} - 1 = \frac{h\nu_f - h\nu_p}{h\nu_p} \equiv \frac{\Delta E_{practical}}{E_g}, \tag{2.14}$$

where $\Delta E_{practical}$ is the anti-Stokes shift due to the Stark energy-splitting and thermal population, and E_g is the electronic energy gap between ground and excited-state. The absorption at λ_p must also be significant, limiting $\Delta E_{practical}$ to be around $2.5 \times k_B T$, where k_B is the Boltzmann constant and T, the lattice temperature. The energy level diagram for trivalent lanthanide ions, as well as their ideal cooling efficiencies are shown in Figure 2-2.

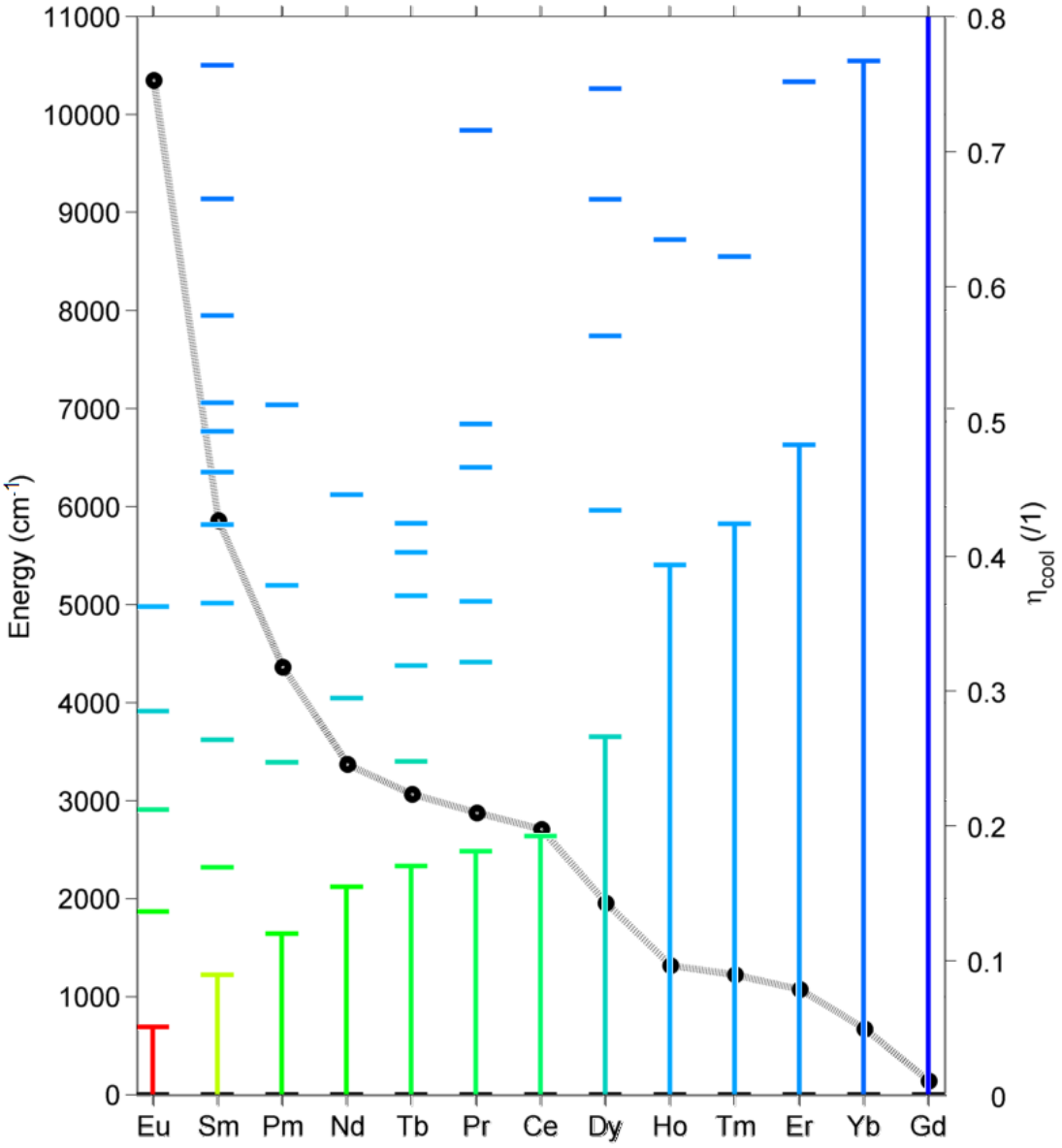

Figure 2-2: Left axis, colored data: Dieke energy diagram – truncated to 11000 cm^{-1} – for trivalent lanthanide ions, ordered by their first excited state electronic energy gap. The first electronic excited level is indicated by a column below it, and the colors correspond qualitatively to the photon necessary to excite that level. Right axis, black circles: ideal cooling efficiency, considering a reference anti-Stokes shift of 521 cm^{-1}, i.e. $2.5 \times k_B T$ at room temperature. Position of the energy levels from [102].

Taking the cooling efficiency of the ions in the lanthanide series, as in Figure 2-2, one can verify that $\eta_{cool,ideal}(Eu^{3+}) \gg \eta_{cool,ideal}(Er^{3+}) > \eta_{cool,ideal}(Yb^{3+}) > \eta_{cool,ideal}(Gd^{3+})$, i.e. Yb^{3+} should have almost

the worst performance. However, other factors also play a role, the most important one being the intrinsic nonradiative decay rate k_{NR}, which depends not only on the dopant but also on the host matrix.

The first form of nonradiative decay which an excited ion can undergo is due to multiphonon relaxation. While the energy gap is mostly defined by the dopant ion, the phonon distribution will depend on the host material. The higher the maximum phonon energy of the material, the higher is the probability that a multiphonon relaxation can bridge the ion energy gap. The rate of multiphonon relaxation k_{NR} is given by an exponential energy gap law [100], Eq. (2.15).

$$k_{NR} = \beta_{e1} e^{-\left(E_g - 2\hbar\omega_{max}\right)\alpha_{e1}}, \tag{2.15}$$

where β_{e1} is the electronic factor, E_g is the energy gap of the transition, $\hbar\omega_{max}$ the maximum phonon energy of the host and α_{e1} a constant for a given host. It can be shown that if one expects a material to intrinsically achieve > 90% of its ideal cooling efficiency, it should have a maximum phonon energy of not more than $E_g/8$ [102], where E_g is the energy gap of the electronic transition in consideration. That implies that not all the ions shown in Figure 2-2 will succeed in being cooled optically in known laser materials. Another consequence is that the high-energy-gap ions such as trivalent ytterbium have a larger range of possible host candidates, as is shown in Figure 2-3, together with some of the materials in which they had shown optical cooling.

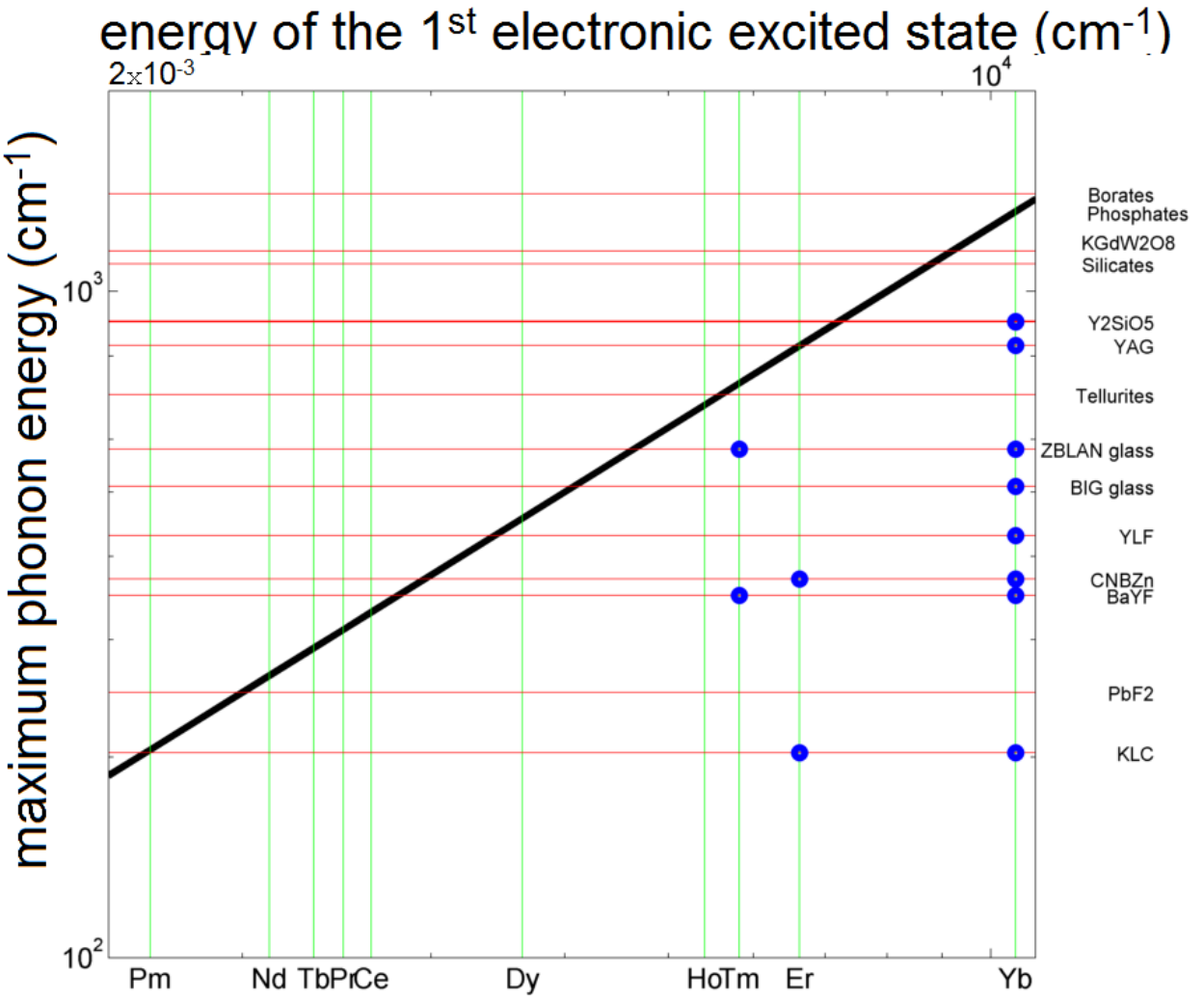

Figure 2-3: Maximum phonon energy (left axis) and first excited state energy (top axis) of some rare-earth-doped materials utilized in laser cooling experiments. The circles represent materials in which laser cooling has been observed. The black line represents $E_g/8$, the limiting maximum phonon energy of a host for efficient optical refrigeration, i.e. materials lying above that line are not expected to present efficient optical cooling. Inspired after [102].

All of the optically-cooled material combinations presented in Figure 2-3, fall below the $E_g/8$ line. While small energy gap lanthanide ions have the potential of higher cooling efficiency, it can be seen that no cooling is likely for any ion with E_g below that of Pm^{3+}, if embedded in a lattice of a KPb_2Cl_5 crystal (KLC). These very low phonon energy materials are not yet ubiquitous and present several fabrication and handling challenges. A list of typical laser hosts and their corresponding maximum phonon energies is shown in Table 2-1.

Table 2-1: Maximum phonon energy of laser materials.

Material	Maximum phonon energy (cm^{-1})	Refer.
Glasses		
Borates	~ 1400	[103]
Phosphates	1100 – 1200	[103]
Silicates	~ 1100	[103]
Germanates	~ 900	[103]
Tellurites	~ 700	[103]
Fluorozirconates	~ 500	[103]
ZBLAN	580	[104, 105]
$57ZrF_4$-$36BaF_2$-$4LaF_3$-$3AlF_3$ (ZBLA)	580	[106]
$43PbF_2$-$17InF_3$-$17GaF_3$-$4LaF_3$-$19ZnF_2$ (PIGLZ)	520	[106]
Fluorides		
InF_3	512	[107]
BaF_2-InF_3-GaF_3-ZnF_2-LuF_3-GdF_3 (BIG)	~ 510	[102]
Fluorochloride		
CdF_2-$CdCl_2$-NaF-BaF_2-$BaCl_2$-ZnF_2 (CNBZn)	~ 370	[102]
Sulfides (Ga, La)	~ 450	[103]
Crystals		
Chlorides		
KPb_2Cl_5 (KLC)	203	[108, 109]
Fluorides		
$LiLuF_4$ (YLuF)	430	[110]
$LiYF_4$ (YLF)	560	[111]
PbF_2	250	[112]
Oxides		
$Y_3Al_5O_{12}$ (YAG)	830	[113]
$KGd(WO_4)_2$	900	[102]
Y_2SiO_5	900	[102]

2.1.2.1 The energy structure of Yb:$Y_3Al_5O_{12}$ (Yb:YAG) crystals

Yb:$Y_3Al_5O_{12}$ (Yb:YAG) crystal lasers are ubiquitous, which is why this crystal has been studied extensively. Yb:YAG has a relative simple quantum structure, with only two manifolds, and negligible upconversion, excited-state absorption and concentration quenching. These properties make the theoretical analysis relatively simple, in which the crystal can be well approximated by a quasi-three-level system, although at low temperatures, e.g. 77 K it becomes a four-level-system. Brown [114], proposed a kinetic model which uses a formalism which does not need to subjectively determine the transition between the three-level to the four-level model, thus it works continuously for arbitrary temperatures. The upper state manifold $^2F_{5/2}$ contains three Stark levels, and the ground state manifold $^2F_{7/2}$ contains four Stark levels, as shown in the Figure 2-4. The Stark levels are labelled with indexes (p, q), where p = 1 for the $^2F_{5/2}$ manifold and p = 0 for the $^2F_{7/2}$ manifold, and q = 1 to $(2J + 1)/2$.

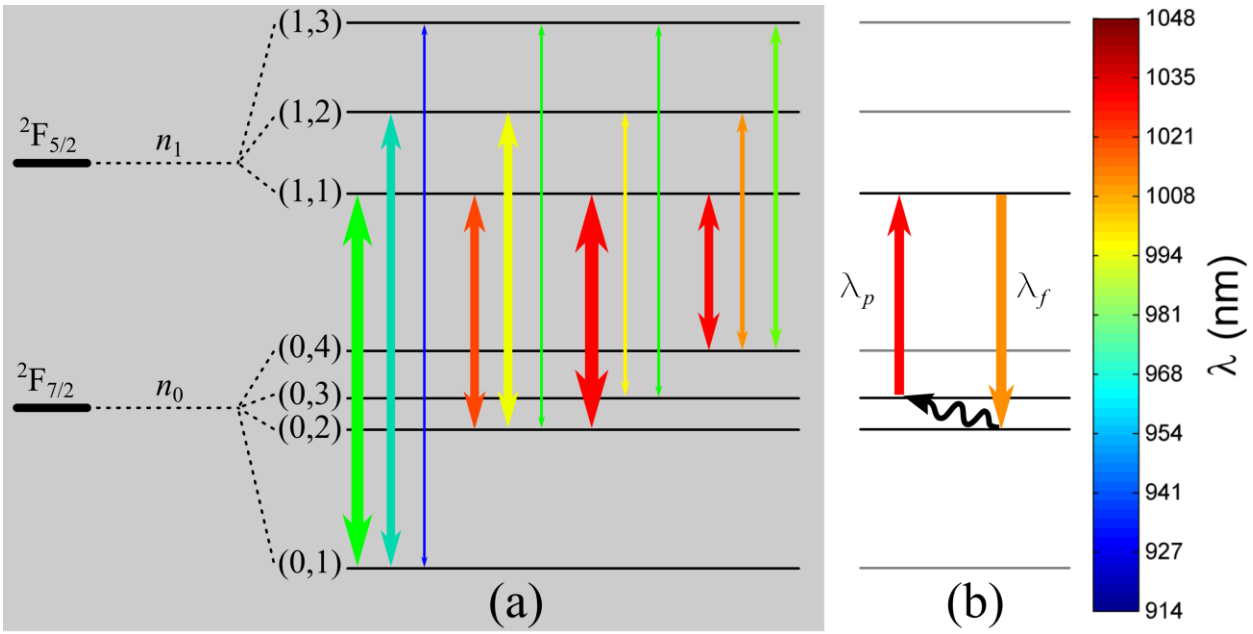

Figure 2-4: Yb^{3+}:YAG energy levels. (a) Possible radiative transitions. (b) Radiative excitation by laser followed by a mean fluorescent photon emission and electronic thermalization. Distances between sublevels are on a scale to their relative energy, and the corresponding wavelength is labeled by the line color. The thickness of the arrows is logarithmically proportional to a scaled relative branching ratio of the spontaneous emission.

Assuming that the atoms can undergo excitation or decay between the two manifolds, and that the total electron density is conserved, the ground and upper manifolds electron density n_0 and n_1 can be related to each other through the equations:

$$\frac{\partial n_1}{\partial t} = I_P \frac{\lambda_P}{hc}\left[n_0\sigma_a(\lambda_P) - n_1\sigma_e(\lambda_P)\right] - \frac{n_1}{\tau_{eff}}; \tag{2.16}$$

$$n_0 + n_1 = n_T, \tag{2.17}$$

where λ_P, h, c, σ_a, σ_e and n_T are respectively, the pump wavelength, Planck's constant, speed of light in vacuum, absorption and stimulated emission cross sections and the total density of active ions. $\tau_{eff} = (\gamma_R + \gamma_{NR})^{-1}$ is the effective lifetime of the excited manifold, and γ_R and γ_{NR} the radiative and non-radiative decay rates. The flux density of electrons in the excited state manifold is given by Eq. (2.16), where the first term on the right side is the flux density of pump photons, multiplied by the probability of an incoming photon being absorbed, minus the probability of stimulated emission. The second term accounts for the flux of photons which decay spontaneously, both through radiative and non-radiative paths. The conservation of total density of active ions is stated in Eq. (2.17).

The fact that the population of individual manifolds depends on the pump intensity, implies that the resonant absorption coefficient, $\alpha_r = \sigma_a n_0 - \sigma_e n_1$ also depends on the pump intensity. The values of n_i can be found from the steady-state solution of Eqs. (2.16) and (2.17):

$$\begin{aligned} &\frac{\partial n_1}{\partial t} = 0 = I_P \frac{\lambda_P}{hc}\left[n_0\sigma_a(\lambda_P) - n_1\sigma_e(\lambda_P)\right] - \frac{n_1}{\tau_{eff}} \\ &\Rightarrow n_1 = n_T\left(1 + \frac{\sigma_e}{\sigma_a} + \frac{I_s}{I_P}\right)^{-1}, \end{aligned} \tag{2.18}$$

where $I_s = hc/(\lambda_P\sigma_a\tau_{eff})$ is the pump saturation intensity. The resonant absorption coefficient dependence on the pump intensity I_P is written as

$$\alpha_r = \sigma_a n_0 - \sigma_e n_1 = \sigma_a n_T - n_1(\sigma_a + \sigma_e) = n_T\left[\sigma_a - (\sigma_a + \sigma_e)\left(1 + \frac{\sigma_e}{\sigma_a} + \frac{I_s}{I_P}\right)^{-1}\right]$$
$$= \alpha_{r0} - n_T(\sigma_a + \sigma_e)\left(1 + \frac{\sigma_e}{\sigma_a} + \frac{I_s}{I_P}\right)^{-1}, \quad (2.19)$$

where α_{r0} is the small-pump-intensity absorption coefficient, when n_1 tends to zero and $\alpha_r(I_P << I_s) = \sigma_a n_T$. The latter is a widely used form, which allows one to obtain easily one of these spectroscopic quantities from the knowledge of the other two variables.

The theory presented above highlight the basic principles of optical refrigeration, and is sufficient to understand and explain the microscopic optical processes related to this Thesis. The example of Yb:YAG is particularly important since it is similar to most work on LICOS, and it is the material used here. The later part shows the electron population dynamics under optical pumping, and predict a saturation effect, which will be used later to optimize the experiments.

2.2 Heat transfer, theory

2.2.1 Mechanisms of heat transfer

The main mechanisms of energy transport are conductive, convective and radiative heat transfers, and mass transport. Mass transport is negligible in typical optical cooling experiments, and it is therefore not considered.

2.2.1.1 Heat transfer by conduction

The power gain though conductive transfer of a body at temperature T_s, connected to a body at temperature T_∞ by a solid link is governed by the integral of Fourier's law of thermal conduction, given by Eq. (2.20).

$$P_c = k\frac{A_{ct}}{L}(T_\infty - T_s), \quad (2.20)$$

where k, A_{ct} and L are the solid link's conductivity, cross-sectional area and length, respectively. When the two bodies cannot form a continuous structure, but are in contact, the conduction is actually a mixture of the three processes of heat transfer, and the effective conductivity, link area and length depend on the experimental conditions such as surface roughness, temperature, contact

pressure, etc. Modeling the conductivity between nonconforming surfaces can be very difficult [115]. For non-matched surfaces, convection and even conduction through the interstitial fluid can occurs; also thermal radiation flows across the gap, making the specific processes complicated. These problems are simplified in vacuum, but still require careful analysis [116]. Thus, in most real-world situations, the analysis of the process is mostly based on empirical derived, experiment-specific parameters.

2.2.1.2 Heat transfer by convection

When not in vacuum, convection can be an important source of heat transfer. The rate of the absorbed power by a sample of temperature T_s immersed in a fluid at temperature T_∞ can be modeled though Newton's cooling law, given by Eq. (2.21).

$$P_{cv} = h_{cv} A_s \left(T_\infty - T_s \right), \tag{2.21}$$

where A_s is the samples's surface area, h_{cv} is the convective heat transfer coefficient, which depends on the temperature, and velocity of the fluid. More often than in conductive transfer, convective transfer is strongly dependent on the experimental conditions, although h_{cv} is often considered a constant. A quick look in the literature shows that, for the very specific case of silica in still air at room temperature, h_{cv} is generally assumed to be between 5 $W \cdot m^{-2} \cdot K^{-1}$ and 25 $W \cdot m^{-2} \cdot K^{-1}$, which shows that it is not accurate to consider a single value of 10 $W \cdot m^{-2} \cdot K^{-1}$, as is often used [117].

Although it is known how the convection heat transfer coefficient depends on the pressure in a free molecular flow region [118], i.e. at high vacuum, only one previous work on laser cooling has explored the viscous flow region [119], without a quantification of the transfer coefficient. In that work it was noticed that the cooling signal reduced by a factor 10 when the pressure was increased from 10^{-5} torr to 10^{-2} torr [119], and no cooling at all was measured at pressures above 1 torr.

2.2.1.3 Heat transfer by radiation

The third mechanism is radiative heat transfer. Although optical cooling is a radiative form of energy transport, here – as in the literature, the term radiative heat transfer for energy exchange through blackbody radiation only, is used. Considering two opaque concentric cylinders of surface areas A_1 and A_2, temperature T_1 and T_2 and emissivities ε_1 and ε_2 one can calculate the radiative heat transfer between them through the Eq. (2.22) [120].

$$P_{1\to 2} = -P_{2\to 1} = \frac{A_1\sigma(T_1^4 - T_2^4)}{\frac{1}{\varepsilon_1} + \frac{A_1}{A_2}\left(\frac{1}{\varepsilon_2} - 1\right)} = P_{1\to 2} = \frac{(T_1^4 - T_2^4)}{1+\chi_d}\varepsilon_1 A_1\sigma, \qquad (2.22)$$

$$\chi_d \equiv \frac{\varepsilon_1 A_1}{\varepsilon_2 A_2}(1-\varepsilon_2),$$

where σ is the Stefan-Boltzmann constant. It is easy to see that if one of the cylinders has a fixed emissivity ε_1, thermal radiation heat transfer can be minimized by minimizing χ_d. It can be also noticed that if the outer cylinder is a black-body ($\varepsilon_2 = 1$) at the temperature $T_2 = 0$ K, Eq. (2.22) reduces to the Stefan-Boltzmann law:

$$\frac{P_{1\to 2}}{A_1} = \varepsilon_1\sigma T_1^4. \qquad (2.23)$$

For semi-transparent materials this expression is modified to Eq. (2.24) [121]

$$\frac{P(\lambda)}{V} = 4\alpha(\lambda)n^2(\lambda)\sigma T^4, \qquad (2.24)$$

where V, α and n are the volume, the absorption coefficient and the refractive index of the sample, respectively. Several laser-active materials are semitransparent, and it is obvious that a complete analysis of their thermal emissivity is cumbersome. This also affects the temperature measurement by thermographic methods, since blackbody radiation from the direction of a semitransparent sample also includes the emission of its background.

The analysis of heat transfer uses relatively simple laws, but as it is described above, it requires a critical and careful implementation: it need to account for real-world parameters and particularities of different materials and environments. The heat transfer description presented here is general, and will be unified with the relevant photo-physical parameters of the samples in the Chapter 5, providing a model for the optical cooling experiment. In solids, heat conduction and convection are usually the main sources of heat dissipation at room temperature. At high temperatures – such as in light bulbs – , or when a very cold background is available – such as in space – heat transfer by black-body radiation can be the main path of heat dissipation. In optical cooling, the share of different paths for heat transfer depends on the design. Here, conduction is minimized while convection and black-body radiation are not modified by the use of vacuum or selective coatings, and the quantification of these contributions are discussed in detail in Chapter 5.

CHAPTER 3 SPECTROSCOPIC TECHNIQUES FOR OPTICAL COOLING OF SOLIDS

The measurement and understanding of the spectroscopic properties of materials are fundamental to the realization of laser cooling in solids. This chapter describes the instruments used for the spectroscopic measurements of the materials studied throughout this thesis. Standard commercial instruments such as absorption spectrometers are briefly described, while new techniques or a tailored combination of multiple instruments are explained and justified in more detail. Although some examples of the measurements performed are shown to illustrate the results, complete measurements are left to the corresponding section of the thesis, where the results are used.

3.1 Resonant-absorption spectroscopy

The absorption spectra of the samples were measured using a Perkin Elmer spectrophotometer, model UV/Vis/NIR Lambda 950. The more recent measurements shown in the Chapter 6 used a Perkin Elmer spectrophotometer, model Lambda 1050. These instruments use a tungsten-halogen light source, filtered by a scanning holographic grating and a slit. The resulting beam of 1-nm-bandwidth is spatially divided, one passing through the sample and another passing through a reference. A chopping scheme separates the attenuated beam and the reference, which are collected in turn by a photomultiplier tube for the visible wavelengths and a cooled Lead-Sulphide cell for near infrared wavelengths. The resulting transmission spectra, after reference subtraction, is collected and displayed in a computer. In the case of the solid samples used here, no reference is placed in the reference arm of the spectrometer, thus the internal absorption is calculated by subtracting the Fresnel reflection – for known materials such as YAG, or from the spectrum baseline in the case of new samples or when scattering is present.

3.2 Photoluminescence measurement techniques

3.2.1 Photoluminescence spectra

One of the fundamental quantities of LICOS is the external mean fluorescence wavelength, defined as the wavelength of a photon of energy corresponding to the mean energy of the escaping photons, given by Eq. (2.4). At this wavelength a lossless material present a transition between Stokes

heating to anti-Stokes cooling when pumped with a narrow bandwidth light source. All the photoluminescence spectra presented here were obtained using an Ando AQ6317B optical spectrum analyser (OSA) for the wavelength range 800 nm – 1750 nm, and a Thorlabs Splicco CCS100 charge-coupled-device spectrometer (CCS), for the wavelength range 350 nm – 700 nm. Depending on the type of the measurement, different setups were utilized. The basic setup consists of a pump laser, which is directed to the photoluminescent sample, and its fluorescence is collected by an optical fiber and directed to the OSA or CCS, as shown in the Figure 3-1. The more specific cases are presented in the following sections.

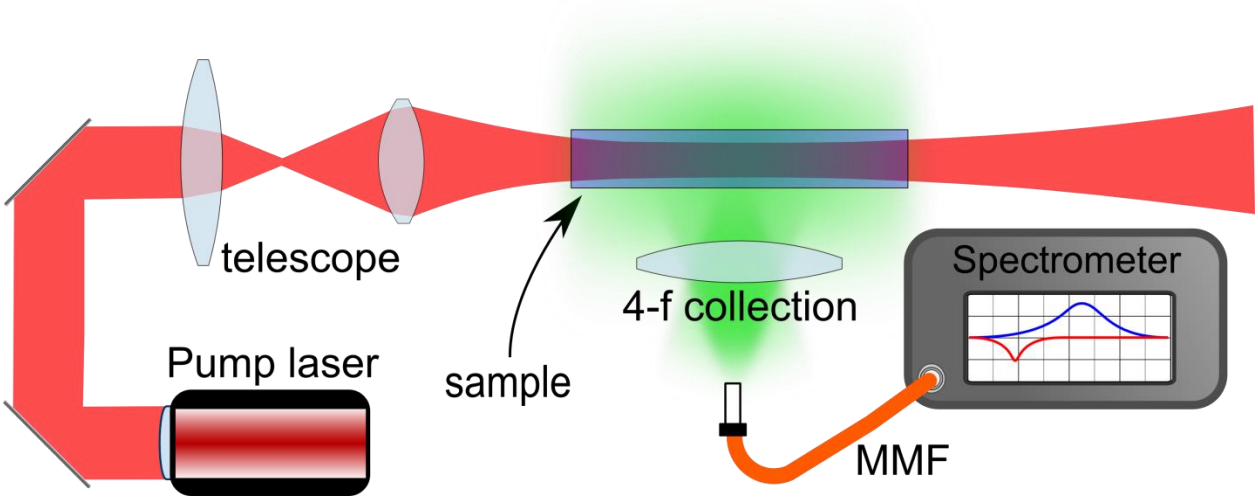

Figure 3-1: Diagram of the general optical setup for measurement of the photoluminescence spectra. The sample is placed at the waist of a collimated beam and a collection lens is placed at a 90^{o} angle at a distance 2*f*, where *f* is the focal length of the lens. The fluorescence is thus focused into a multimode fiber at a distance 2*f* from the lens, and directed to an optical spectrometer.

3.2.1.1 Double-chopping technique for photoluminescence measurements

Due to different pumping wavelengths used in the experiments, as well as to compare in-band and out-of-band pumping of multilevel systems, a filtering scheme was implemented to work for a wide wavelength range. Although a collinear polarization beam splitter could be used to separate the fluorescence signal from the intense pump, it limits the wavelength range, collection optics aperture, and would not work for highly scattering samples. Thus a simple method to perform

broadband collinear spectroscopy was developed, with a high pump rejection factor using a single optical chopper. The setup is shown in Figure 3-2.

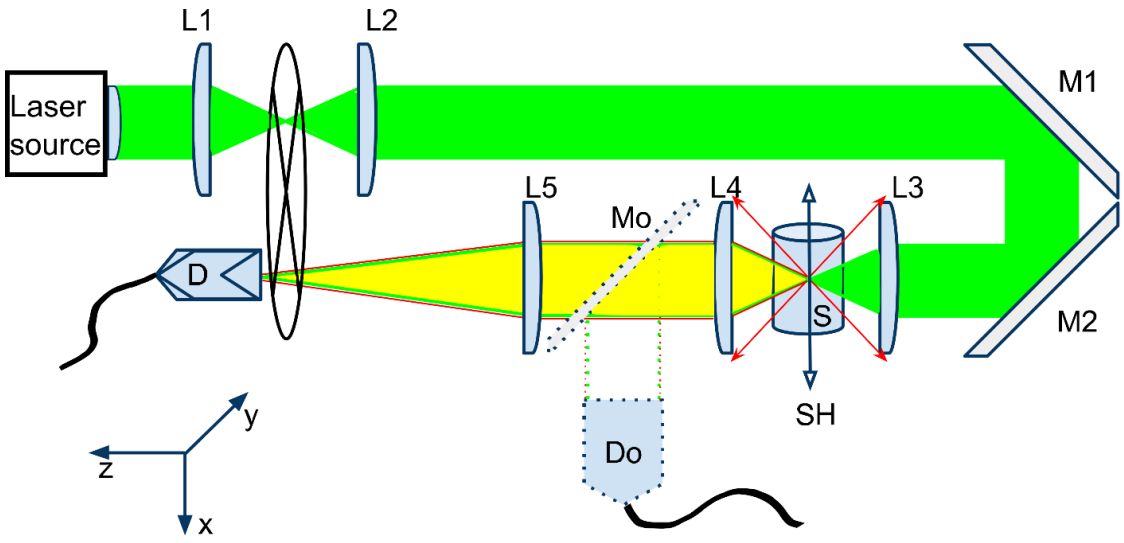

Figure 3-2: Double-pass chopping scheme for photoluminescence spectra measurement of long-lived excited state materials.

The method is based on a double-pass chopping scheme (Figure 3-2), where the input laser beam is modulated by an optical chopper wheel, and reflected back in the direction of the chopper, being focused into the sample *S*, and directed to the detector *D*. The pump beam is temporally filtered by adjusting the vertical position of the chopper wheel, so that it is blocked during the collection of the fluorescence signal. With this approach, the modulated input beam is filtered, meanwhile the quasi-continuous fluorescence signal is preserved, and reaches the detector without significant attenuation. In order to obtain a fast chopping time, the beams are focused in the plane of the chopper wheel by the mirrors L1 and L5. An optional mirror M_o is placed inside the telescope L5-L4, in order to measure un-filtered signals with large area photo detectors, for radiative lifetime measurements, for example. The double-pass chopping scheme also attenuates part of the fluorescence signal, since it reduces the average power of the pump laser, and the input into the detector. This attenuation comes from the mark-to-space ratio, which is generally equal to unity and gives -3 dB attenuation of a quasi-continuous signal. Using a chopper wheel of unity mark-space-ratio implies that there is always a time interval when both pump light and fluorescence are allowed to pass through the wheel, due to their finite focused beam waist radii. A chopper wheel

of greater-than-one mark-to-space ratio allows almost complete beam obscuration before the signal of the opposite beam is collected. The larger mark-to-space ratio can be achieved from conventional wheels by superposing two identical chopper wheels, with a phase difference. In this case, the attenuation can be expressed by $\alpha_{dB} = 10 \times \log(0.5 - \delta/T)$, where $2\pi\ \delta/T$ is the phase difference between the two wheels. A typical value of these parameters in the present experiment is δ/T of around 0.1, giving a attenuation of -4 dB. So the total attenuation experienced by the fluorescence signal is -8 dB, while the pump reaches the detector with an attenuation from -4 dB up to -50 dB (experimental), adjusted by changing the vertical position of the chopper wheel and the relative position of the focused pump and fluorescence. If the energy of the beams is constrained to a finite radius, the system should reject all the undesirable light, but in the experiments, a fraction of 10^{-5} of this light is collected at the detector.

3.2.1.2 Bifurcated probe

A bifurcated probe allows a single tip to be used to simultaneously pump a sample and to collect the emitted fluorescence. Since both the probe optics and pump optics are in a single device, no independent alignment is necessary. Also, the optical signals are delivered by optical fibers, thus one can measured a sample difficult to reach through free-space optics. An example of this situation is the measurement of the PL with the sample inside an environmental chamber. In order to preserve the compatibility between the probe input/output and the equipment available at the laboratory, a homemade probe was preferred instead of a commercial one. The pump optics consists of a single mode fiber which can be coupled easily to a pigtailed diode laser, or to a fiber which had been previously coupled to a Titanium-Sapphire (Ti:Sapph) laser. The collection is a multimode fiber with a core of 200 μm, which is coupled to the OSA for the infrared wavelength band or the CCS for the visible wavelength band. Both fibers are held together by a Pasteur pipette which is fused and stretched in order to have the exact inner diameter to tightly hold both fibers in parallel, as shown in Figure 3-3.

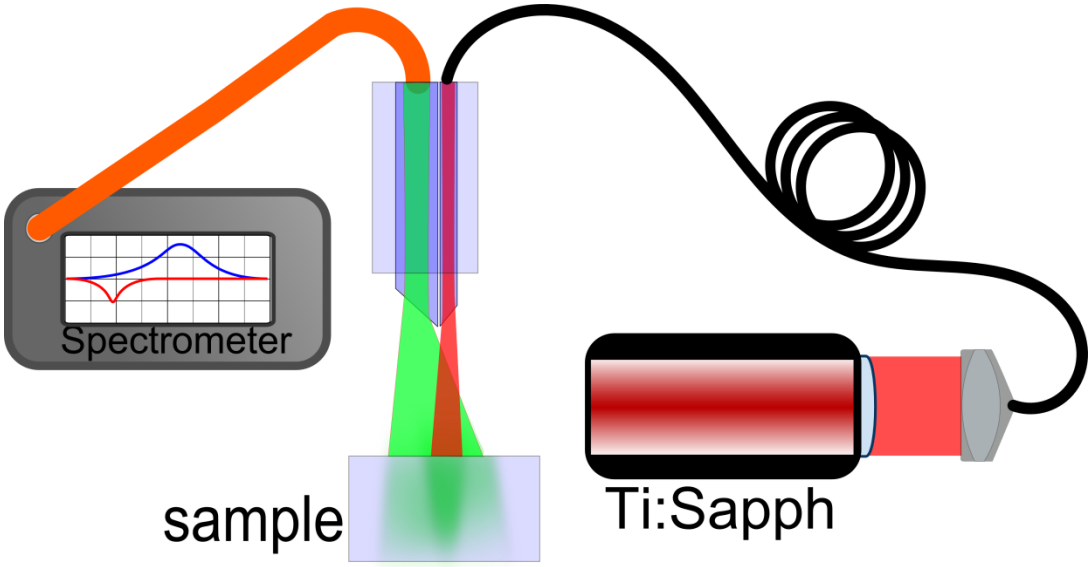

Figure 3-3: Diagram of the optical setup for measurement of the photoluminescence spectra using a bifurcated probe as pump and collection optics.

The bifurcated probe was used to obtain preliminary photoluminescence spectra of samples enclosed in an environmental chamber. Since the fibers are not lensed and no additional optics is used, the pump-probe region is not well delimited thus the spectra can be distorted due to reabsorption and spatial inhomogeneity. Therefore the obtained results using this probe are only qualitative.

3.2.1.3 Depth-dependent photoluminescence spectra

The exact mean fluorescence wavelength of the typical materials used for laser cooling differs significantly in the literature. For instance, for the work reported in this Thesis, a MFW = 1010 nm was measured for a 1-mm-thick, 3 at. % Yb:YAG sample at 296 K, while Ref. [122] reports a value of 995 nm for a 2.3 at. % sample from the same supplier. The same material is reported to have a MFW equals to 1007 nm [20, 123], 1008 nm [124], and 1009 nm [114]. The calculation using theoretical energies and branching ratios from [125] leads to an internal MFW equals to 1006 nm. From that it can be concluded that one should not expect to measure the external MFW shorter than 1006 nm for Yb:YAG. That indicates that our result is indeed consistent with what should be expected for a bulk sample.

Several factors – and errors – can lead to diverging values of the mean fluorescence wavelength. First, its value is temperature-dependent, so one should compare and report the measured value together with the temperature at which the experiment is performed. Common errors can be introduced by using number of photons instead of intensity in the Eq. (2.4), or raw nonlinear scaled measurements such as dBm or logarithmic scales. One should be careful to distinguish between the internal PL spectra, as emitted by the excited ion, and the external PL, which is measured outside a bulky sample, and depends on the probing and collection conditions, as well as the sample absorption, quantum efficiency, thickness, refractive index and shape, which accounts for the inner-filter effect, or simply reabsorption. Thus, it is useful to obtain the depth-dependent photoluminescence spectra, so that the intrinsic MFW as well as the external MFW of samples of different dimensions can be estimated, using a single sample for the measurement. This helps to rule-out samples in which reabsorption is too large to allow optical cooling, and to identify a sample with higher quantum efficiency – thus a less red-shifted eMWF – amongst similar samples. For liquid samples, the effect of reabsorption is observed easily without the need of changing the geometry, but simply by changing the concentration, as shown in Figure 3-4 for a sample of Rhodamine101 in ethanol.

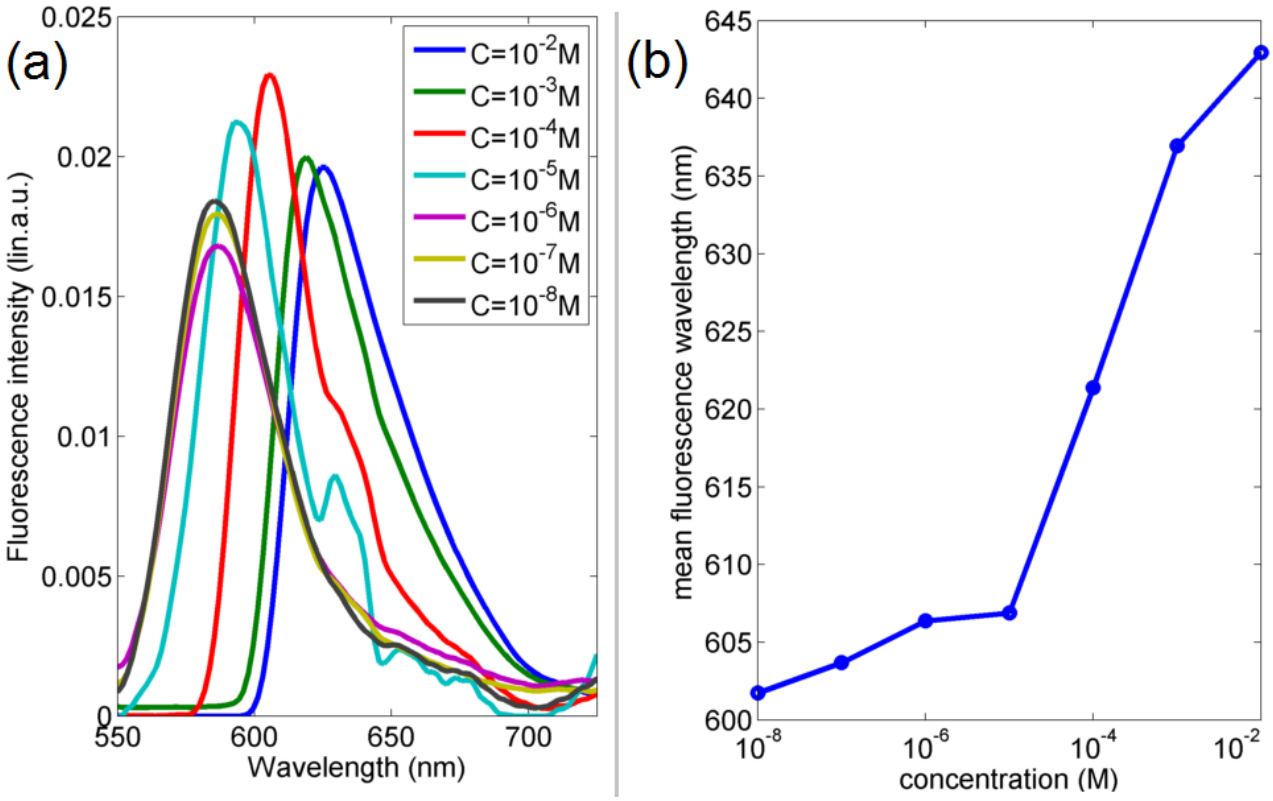

Figure 3-4: Fluorescence spectra (a) of Rh101:EtOH at different concentrations, and the resulting mean fluorescence wavelength (b). The pump and collection were aligned close to the surface of the vial where the samples were placed.

The data shown in the Figure 3-4 were collected using both pump and collection optics focused close to the surface of the vial containing the samples. As can be seen, even at the surface the effects of reabsorption are evident.

For the PL measurements, two configurations for depth-dependence were used. In the first one, a multimode fiber of 200 μm core diameter is placed next to the sample at a place where the collected power is maximized, and directed to the OSA. For this measurement, the collection volume and aperture are large thus the measured signal represents well the external PL. Since the MFW of Yb:YAG differ from one value reported on the literature, the PL was also measured by using a small probing volume, by using a collimating lens and a 65 μm-core-diameter fiber, which also acts as a pinhole, as the collecting part of the setup. The sample is moved transversely so that the PL at a large depth can be measured. The second setup is shown in Figure 3-5. In this setup, the sample is moved so that the pump beam is at the desired distance from the collecting

surface/window, and the probe optics is realigned to maximize the collected power, which indicates when the pump and probe overlap.

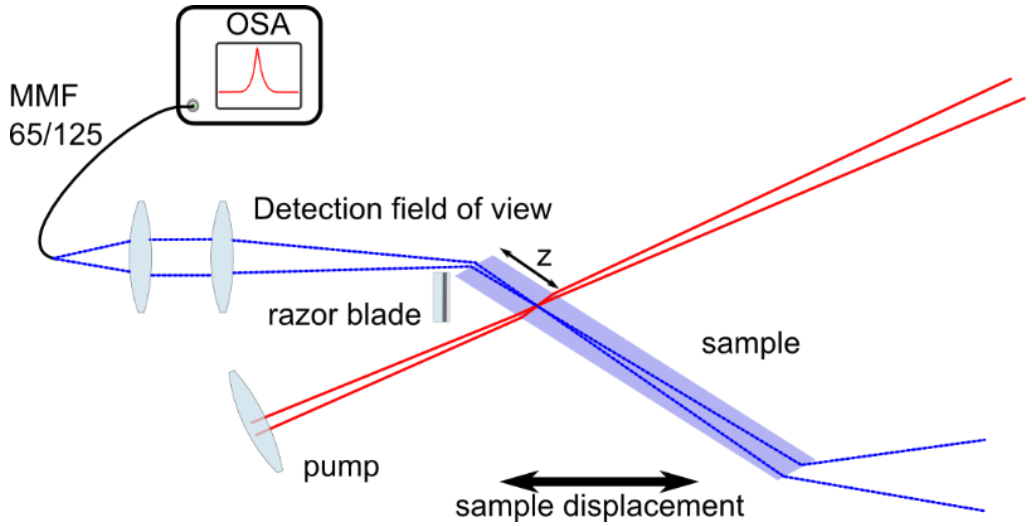

Figure 3-5: Diagram of the spectroscopic setup for depth-dependent photoluminescence measurements.

Using the setup of Figure 3-5 with a pump laser at 920 nm wavelength, the measured PL spectra of a 3% Yb:YAG sample is shown in Figure 3-6.

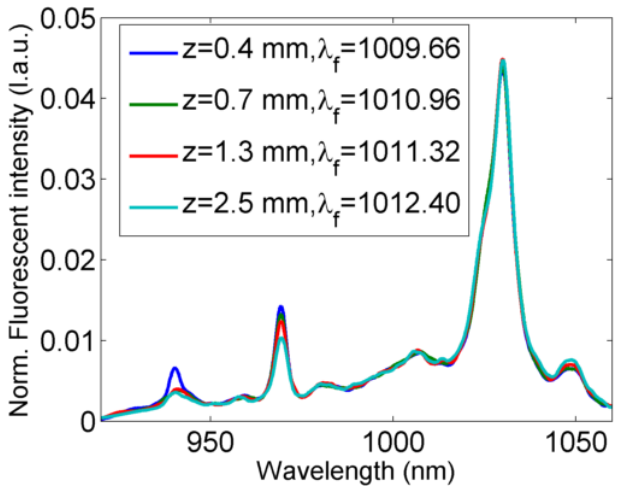

Figure 3-6: Depth-dependent photoluminescence spectra of a 3% Yb:YAG crystal.

From the spectra above one can estimate the internal MFW, or the "zero-thickness" fluorescence, by compensating the emission spectra using the absorption spectra and the depth at which the PL spectra was collected. By doing so, one can observe that the spectral structure converge when corrected for the depth (Figure 3-7), and the mean fluorescence wavelength approaches a value of 1009.5 nm. It can be concluded that the MFW at zero-thickness, a good estimate for the intrinsic MFW when trapping is disregarded, is 1009.5 nm.

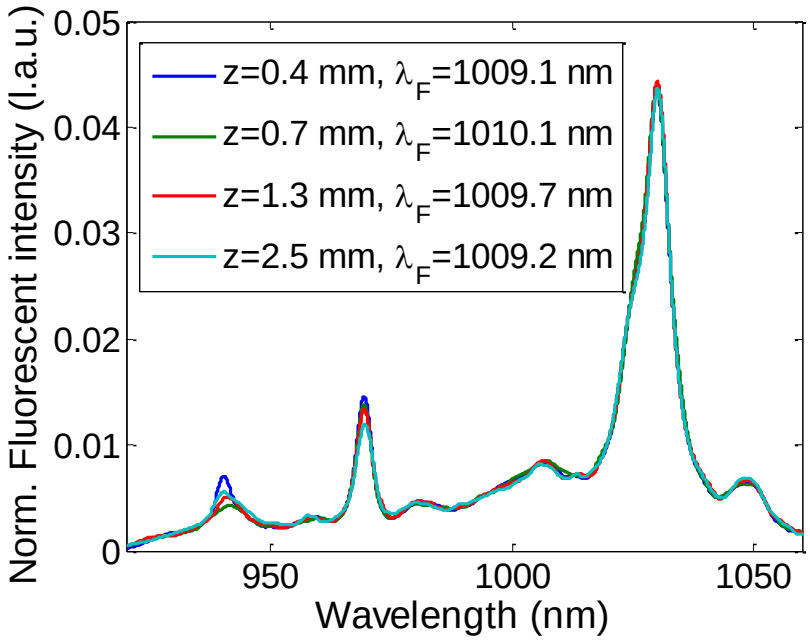

Figure 3-7: Photoluminescence spectra of a 3% Yb:YAG crystal, after correction for reabsorption. The labels indicate at which depth, *z* the uncorrected data is collected.

Although compensation for reabsorption is not as simple as discounting the absorption coefficient, the procedure can give us an idea of how short the values for the MFW can be. As the graph shown in Figure 3-7 indicates, the MFW measured at the surface is not expected to be much less than 1009.1 nm, as indicated by the trend shown in the uncorrected data in the Figure 3-6. The second method confirm that our measurements are consistent and are a better reference than the previous reported value for the MFW of the Yb:YAG sample. Unless otherwise stated, the method used for the PL spectra measurement throughout this work is the first one, since it measures the external MFW, probing a large volume and with little alignment.

3.2.2 Luminescence lifetime

The measurement of the luminescence lifetime can be made in various ways. In the initial experiments, the lifetime was measured in the time domain with an oscilloscope. A homemade circuit with two parts was made to amplify the collected signal from a photodiode, and for triggering the oscilloscope when the pump electronics was turned-off. Although the system works well, it takes a long time for the pump laser to restart, making it difficult to have several measurements within a reasonable time. The measurements presented in this thesis were made with a new setup, using a large area photodiode, a commercial amplifier and a mechanical chopper. The use of the mechanical chopper allows several measurements to be averaged in a short time. In this setup, the beam from a Ti:Sapphire laser is focused onto a 2-slot chopper wheel. The chopped beam is collimated, attenuated to ~ 20 mW of power and loosely refocused into the sample. At an angle which avoids both transmitted light and specular reflection (Figure 3-8), a 4-*f* telescope collects and directs the light from the sample to a silicon photodiode of 13 mm^2 area (Thorlabs SM05PD1B). The signal is amplified by a benchtop transimpedance amplifier (Thorlabs PDA200C) and displayed on an oscilloscope (Tektronix TDS7104). For some measurements in which scattering can be significant, an edge filter is used to block the light at the pump wavelength.

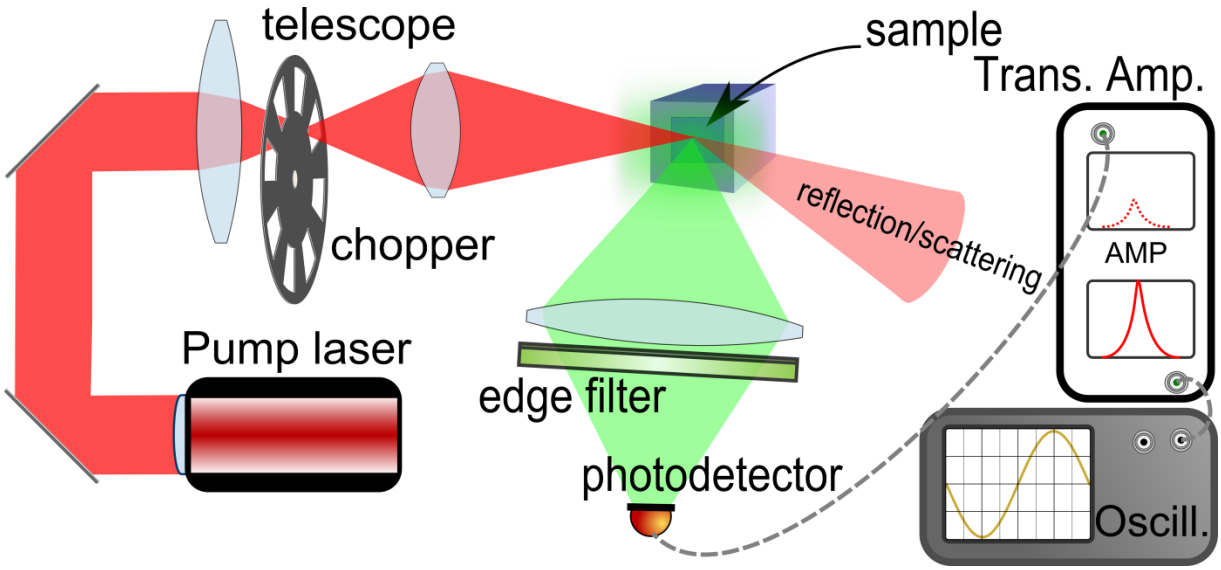

Figure 3-8: Diagram of the experimental setup used for excited-state lifetime measurements.

In the setup shown in the Figure 3-8, using a chopping frequency of 14.00 Hz, a signal drop from 90 % to 10 % of its maximum value in 12 μs is obtained, which therefore gives the temporal

response of the system. This is more than enough for the samples used in this thesis, which have a lifetime on the order of 1 ms.

3.3 Quantum efficiency

The measurement of quantum efficiency is extensively performed for the characterization of fluorophores for biomedical applications, LEDs for illumination, etc. Due to the stringent requirements of optical refrigeration, the knowledge of the quantum efficiency of the materials being studied is of fundamental importance. The external quantum efficiency is defined as

$$\eta_e = \frac{N_{\text{emi}}(\delta\lambda)}{N_{\text{abs}}(\delta\lambda)}, \tag{3.1}$$

where N_{abs} and $\delta\lambda$ are the number of absorbed photons and the single-manifold bandwidth, respectively, and N_{emi} is the number of photons which are emitted and escape the material. It is relatively easy to measure the η_e for a dye, since geometric parameters can be removed and ratiometric methods can be employed. Even then, a reference is needed with a known η_e. These are available mainly in the visible and have uncertainties of ~ 5%, for specially purified dyes not commercialized [126]. For a solid sample, the problem is more complicated since it is not always possible to have a reference with same optical geometry, and a full-spherical measurement may be needed such as by an integrating sphere. Since the geometry and concentration of fluorophores – or active ions – are fixed, reabsorption effects are hard to exclude.

The method introduced in Ref. [127], which is used here, consists of measuring the relative spectral photon number density in the detector in three situations: A, when the pump beam is directed towards the empty Ulbricht integrating sphere (ISp); B, when the sample is inside the ISp and the beam is directed onto the ISp wall; C, when the sample is inside the ISp and the beam is directed onto the sample. The setup utilized in this Thesis is represented in Figure 3-9. The output from a Ti:Sapphire is kept at a constant p-polarization using a Glan-Thompson polarizer, then ~ 1 % is tapped by a glass plate, and the reflection is monitored by a Keithley 6487 Picoammeter. The transmitted beam is focused into the integrating sphere entrance port and directed to the center of the sphere. The diffused light from the sphere walls is collected by a multimode fiber of 200 μm diameter and directed to an Ando AQ6317B optical spectrum analyser (OSA). The OSA calibration is verified using a helium-neon gas laser of wavelength 632.8 nm, and measured a value of 633.0

nm, indicating a 0.1 nm accuracy. The data is collected and processed by a computer, which measures 50 spectra, while normalizing them to the tapped optical power, between the measurements of two spectra.

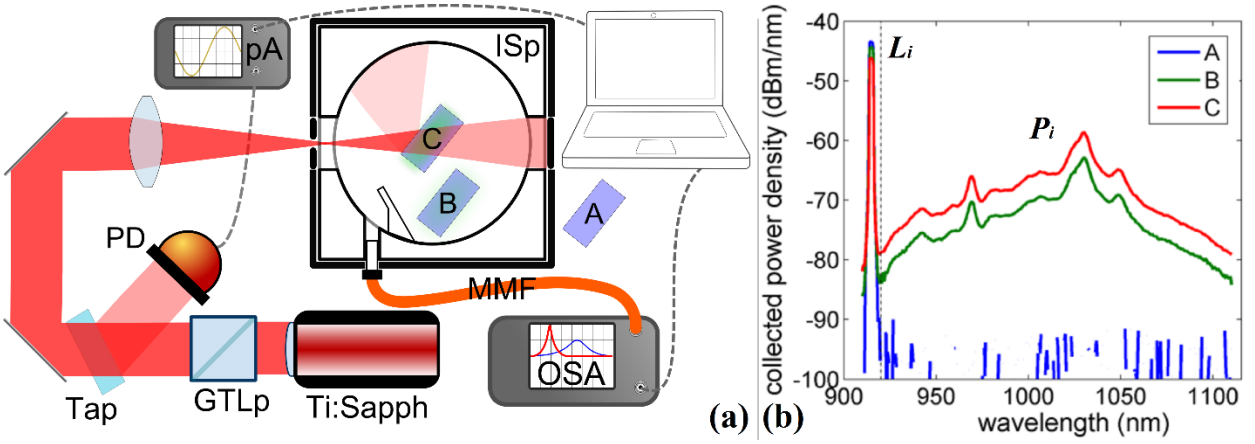

Figure 3-9: (a) Diagram of the setup utilized to measure the external quantum efficiency of the samples by the integrating sphere method. The beam from a Ti:Sapphire laser is polarized with a Glan-Thompson polarized (GTLp) and focused onto the entrance of the integrating sphere (ISp). The polarized beam is tapped by a glass plate (Tap) and the power measured by a photodiode connected to a picoammeter (pA). The diffuse light from the ISp is collected by a multimode fiber (MMF) and measured by an optical spectrum analyser (OSA). (b) Example of collected data for a Yb:YAG sample.

The detected numbers of photons are spectrally separated into two regions: laser and photoluminescence, and are labelled respectively by L_i and P_i, with i being A, B or C, depending on the setup configuration as described above. If the original measurand is spectral power density, it should be multiplied by the corresponding wavelength in order to have the proportional spectral number of photons density. The quantum efficiency is calculated using (3.2).

$$\eta_{\text{ext}} = \frac{P_{\text{C}} - (1-A)P_{\text{B}}}{L_{\text{A}} A}, \qquad A \equiv 1 - \frac{L_{\text{C}}}{L_{\text{B}}}. \tag{3.2}$$

Although the method above is an absolute method, it needs all the instruments to be stable and well calibrated. Alternatively, the whole setup must be calibrated, using a reference. Commercial quantum efficiency references in the infrared region are scarce and not sufficiently tested. For instance, a careful measurement of the η_{ext} of IR26, a dye for the wavelength region around and

above 1 μm, shows its value to be $4.8(2) \times 10^{-4}$ [128, 129], while it is generally assumed to be 5×10^{-3} [128]. In order to avoid such uncertainties, a sample of 3%:Yb:YAG crystal was used, for which the η_{ext} had been measured previously to be 0.9914 by a calorimetric method [34]. A similar sample had $\eta_{ext} = 0.988$ measured by photothermal deflection [122]. These values are very reliable, due to the strict conditions which the sample needed to meet in order to achieve optical refrigeration.

As seen in this chapter, many setups can be used to perform the same photoluminescence measurements, but can result in different measurands. For instance, a bifurcated probe can be used for qualitative measurements of the fluorescence. A depth-dependent measurement is used to estimate the intrinsic mean fluorescence wavelength and a depth-dependent pumping without shaping of the collection optics is sufficient to measure the external MFW. New quantum efficiency references, based on optically-cooled samples, are proposed to calibrate the absolute quantum efficiency setup in order to evaluate new samples.

CHAPTER 4 THERMOMETRY IN OPTICAL COOLING

Thermometry is essential for the characterization of laser-induced cooling of solids (LICOS). Such importance is acknowledged by the fact that a significant amount of work on LICOS is dedicated to the study of thermometric techniques. This chapter dedicates to the study of thermometry for LICOS.

Despite the prevalence of thermometric techniques in many fields of science and technology, there is a need to develop tailored solutions for the thermometry in laser cooling experiments. LICOS experiments can have intense fluorescence, which is absorbed easily by opaque sensors and lead to heating. Non-contact techniques are plagued by the variability of optical properties, and cross-sensitivities of the different samples used for LICOS.

In the first section a review of the most common thermometric techniques used in LICOS is presented, and the second section describes the studies which have been performed in this Thesis in order to demonstrate and consolidate a new technique for temperature measurement of optical cooled samples.

4.1 Theory and review of the thermometric techniques

The investigation of optical refrigeration needs a method for measuring the temperature of the optical cooled sample. The very basic principle of thermometry requires that a thermometer has a negligible thermal mass in comparison to that of the measured sample, so that the temperature of the latter is undisturbed and the thermometer temperature corresponds to the initial value of the sample temperature. In optical cooling, the intense fluorescence which leaves the sample can be absorbed by an opaque sensor, which in turn can warm the sample. Thus not only the thermal mass is important, but the sensor cannot be in contact with the sample during PL emission, i.e. during pumping. The sensor could be placed far away from the sample, or alternatively it could be transparent to the PL. Another possibility is to use the temperature-dependent properties of the sample to perform an indirect measurement of the temperature. All these paths were explored in laser cooling investigations, and are described in the following sections.

4.1.1 Indirect methods of temperature measurement

The indirect thermometric methods use parameters other than the temperature itself to estimate the temperature of the samples. In the case of optical cooling, these parameters are often related to the thermo-optical properties of the sample. The main advantage of such methods is that one does not need an additional device as a sensor, thus the probe thermal load can be zero and can reveal details such as the internal temperature of the sample. They can also provide a fast way to qualitatively estimate the temperature dynamics. The main disadvantage is that, since the sample is its own thermometer, its calibration is valid for a fixed experimental condition and sample. If the experiments are performed under different conditions, one must ensure that none of the interrogated parameters of the sample are changed, or one should compensate for that, which can be cumbersome. These techniques depend on constant recalibration, and are therefore less flexible and are more prone to errors than direct methods.

4.1.1.1 Photoluminescence thermometry

The measurement of the temperature of fluorophore-doped materials through their photoluminescence spectra, or photoluminescence thermometry is a common technique which allows temperature probing in laser crystals and of biomarkers at nanoscale [130-132]. It is based on the thermalization of excited electrons, which when decaying radiatively, emit photons with an average energy depending on the occupation of the Stark sublevel, thus on the temperature [133]. The photoluminescence signal can be measured in the form of the spectral shape, polarization, lifetime or integrated power within a band. The latter, using two or more bands is termed fluorescence intensity ratio (FIR), and it is the most commonly used scheme in laser cooling experiments, where it is usually termed differential luminescence thermometry (DLT). Initial works were, however, based on the full photoluminescence spectra [133-135]. The main disadvantage of the collection of the full PL spectra in DLT is the longer measurement time, compared with the measurements using a few bands. The diagram of a typical DLT setup is shown in Figure 4-1.

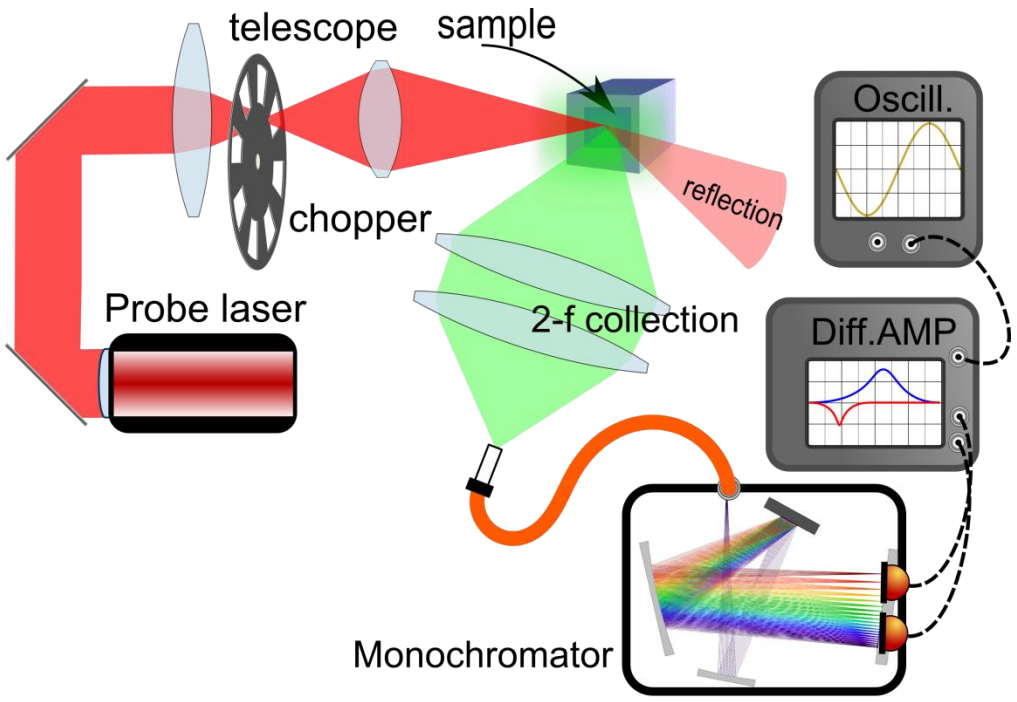

Figure 4-1: Diagram of the typical differential luminescence setup utilised for measuring temperature in laser cooling experiments. The high-power pump laser for the cooling is omitted for clarity.

In DLT, one uses at least two bands so that the fluctuations of the probe power can be cancelled. The temperature dependence is usually determined beforehand by measuring the photoluminescence spectra of the sample, as the sample's temperature is actively driven by a conventional temperature controller such as an environmental chamber, controlled thermoelectric modules or a cryostat. Several works have used DLT to measure temperature drop under laser irradiation [35, 36, 56, 134-143]. Contrary to the opaque contact sensors, DLT is used during optical pumping, which also acts as the probe laser. The temperature measured by this technique is not the bulk average temperature, but depends on the probing region. One strong effect that is generally neglected is fluorescence reabsorption, which distorts the measured spectrum, depending on the depth of the probe region in the sample. Thus, although the previous measurements may have been correct, the calibration is valid only for a certain optical system configuration. This is verified easily by all the diverging results of the mean fluorescence wavelength, which arises mainly from the use of samples of different geometries. As an example, the spectra and mean fluorescence wavelength of samples of different sizes (Figure 4-2) were measured inside an

environmental chamber, with the collection optics (bifurcated probe) not tightly fixed in respect to the sample, thus moving due to the calibration chamber vibrations.

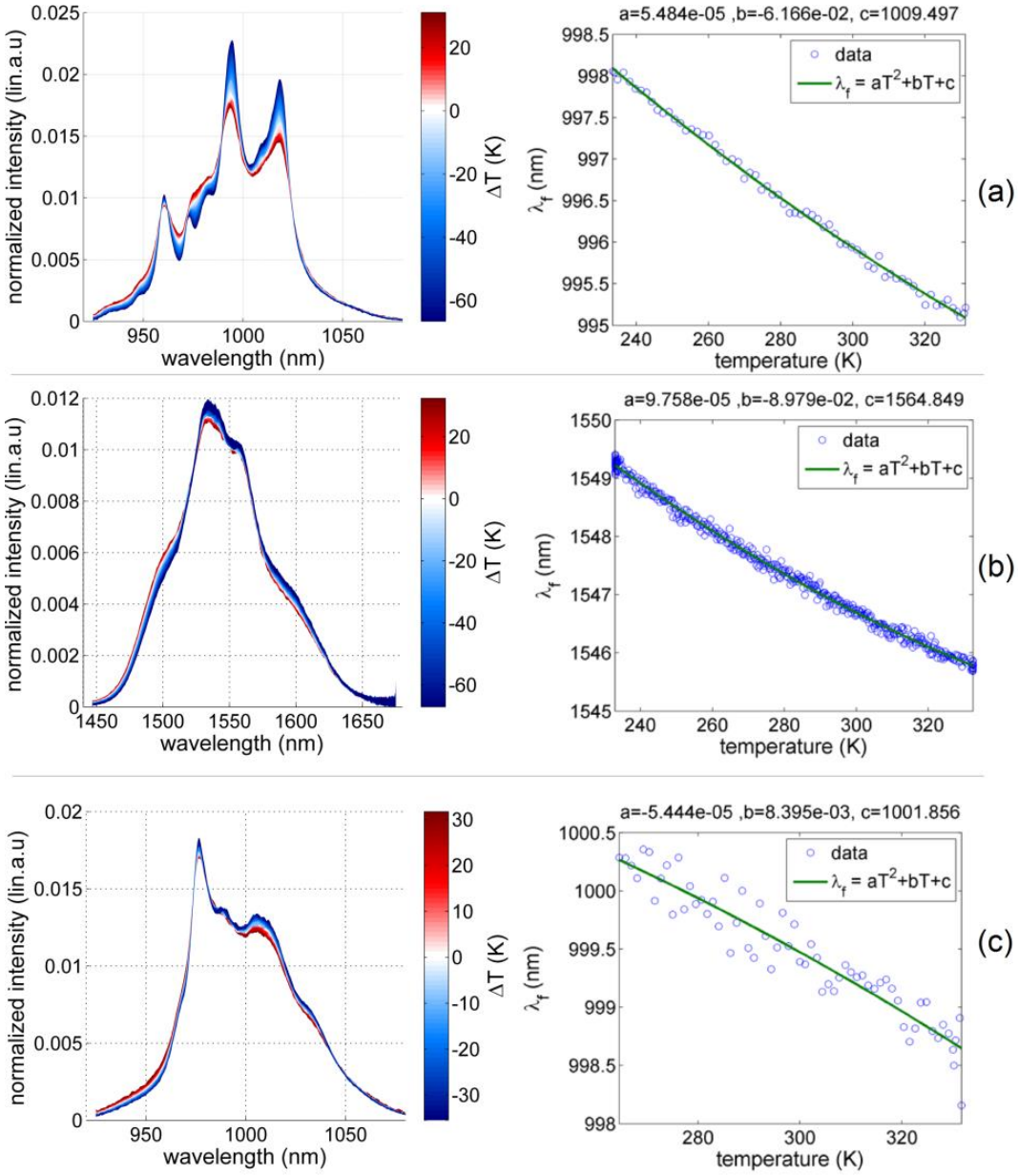

Figure 4-2: Photoluminescence spectra (left) and mean fluorescence wavelength (right) dependence on the temperature difference from room temperature, for samples of different lengths l_s. (a) Yb:YLF nanocrystals, l_s < 0.5 mm. (b) Er:ZBLAN, 0.5 mm < l_s < 1 mm. (c) Yb:CLYSiAl glass-ceramic, l_s = 2 mm.

It is clearly seen in Figure 4-2 that the same setup gives different stabilities for different samples. In the experiment above, the probe measured slightly different volumes and depths, which leads to larger variations in larger samples – since for a tiny sample the maximum depth is fixed to its size.

For very small samples or very high intensities, the reabsorption effects are dependent on the pump intensity, thus the fixed probe-power calibration is not valid. Conversely, if one uses a high probe power during calibration, the sample temperature is not the same as the reference environment, thus the photoluminescence spectra does not correspond to that temperature, but to the unknown temperature of the sample.

4.1.1.2 Thermo-optical methods – Thermal lens

Thermal lens (TL) occurs when a temperature gradient with a transverse component to a passing optical beam, is present inside a thermo-optical-active medium. By monitoring the shape and direction change of the optical beam, one can deduce the lens, or refractive index profile, formed inside the material [144]. This technique is used by several research groups to measure thermal and optical properties of transparent media, and assumes several configurations and names, depending on the parameter being measured. The basic principles of thermal lens measurement is shown in Figure 4-3, where a laser beam passes through an absorbing sample and its divergence is changed by the thermal lens due to the radial temperature change created by the beam itself.

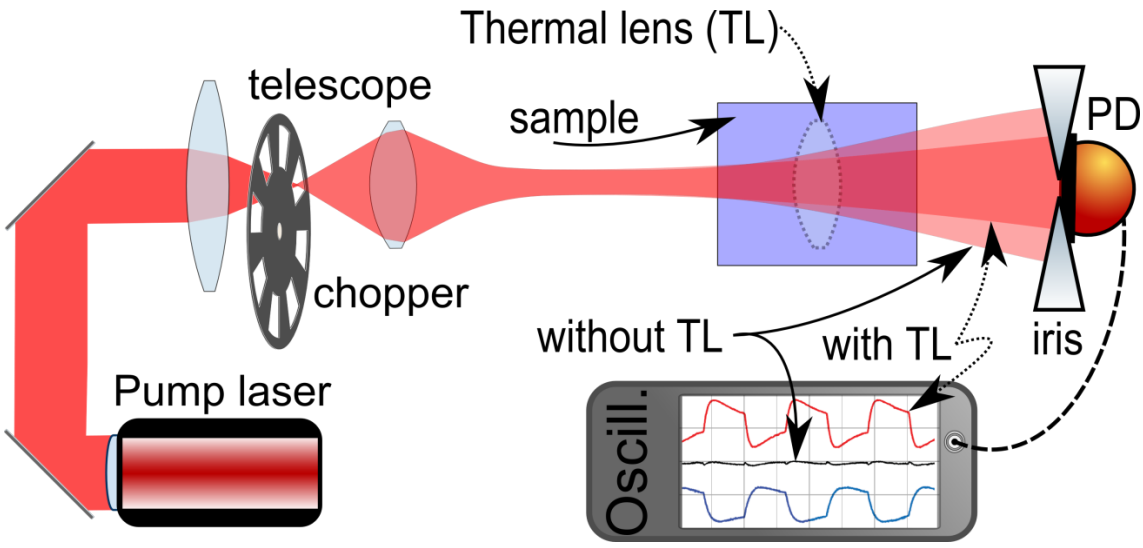

Figure 4-3: Basic thermal lens setup, where the sample is placed at a distance of one Rayleigh range from the beam waist, and the beam power at its center is measured by an iris/pinhole and photodiode (PD). The phase of the cooling signal is opposite to the one from heating.

The setup shown in Figure 4-3 can be modified, for example to monitor the position rather than the power of the probe beam, by using a transversally displaced probe beam (Figure 4-4), which is deflected by the thermal gradient and its position determined by a quadrant detector, thus high sensitivity can be achieved by placing the detector far away from the thermal lens. The latter technique is called photo-thermal deflection spectroscopy (PTDS), and is the main thermal-lensing technique used in laser cooling experiments [12, 19, 39, 145, 146]. In contrast to the conventional thermal lensing experiment (Figure 4-3), where pump power fluctuations can be erroneously interpreted as thermal lensing, in the PTDS the signal is encoded in space as well. In the PTDS the probe beam is deflected in the opposite direction when the sign of the thermal lens changes from positive to negative, i.e. the phase of the cooling signal is opposite to the phase of a heating signal, thus it can be directly interpreted. Another commonly used form of TL called Z-scan uses a strongly focused beam in an axially translatable sample [147, 148], to measure nonlinear refractive indexes and absorption, and recently used to measure the background absorption of semiconductors for laser cooling [149]. Several other configurations are possible, in order to use different combinations of samples and detectors.

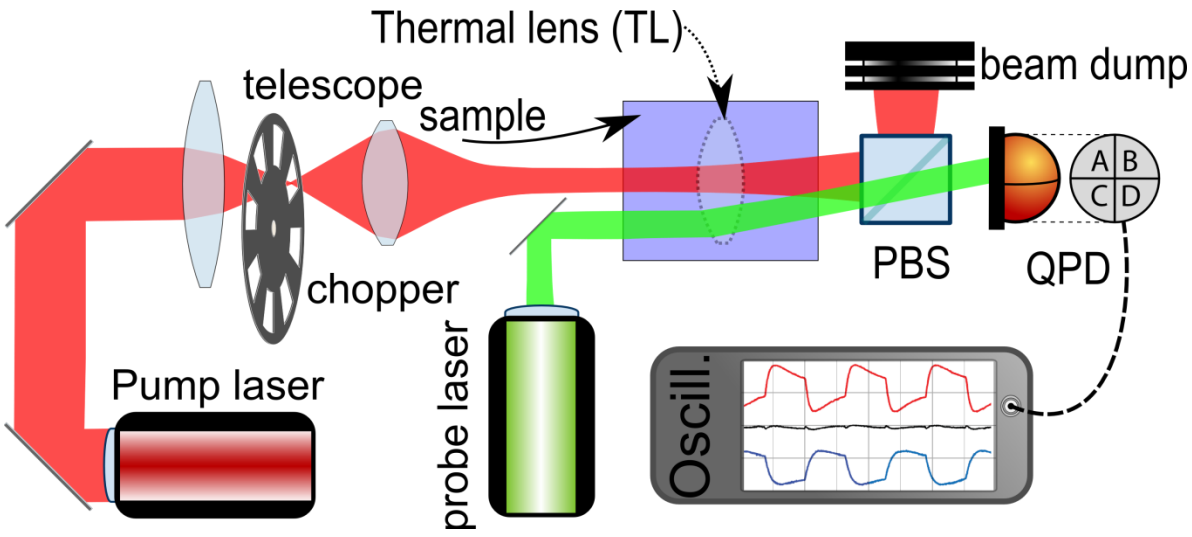

Figure 4-4: Diagram of the basic photothermal deflection setup utilised for measuring temperature in laser cooling experiments. The probe and pump laser have orthogonal polarization and are separated at the polarizing beam splitter (PBS). The deflection of the probe beam is measured in a quadrant photodetector (QPD).

The thermal lens signal is often expressed as the fractional intensity change $S = \Delta I_{probe}(\infty)/I_{probe}(0) - 1 = \Delta I_{probe}/I_{probe}(0)$, where I_{probe} is the center intensity of the probe beam [150]. The recovery of ΔT from ΔI_{probe} is not straightforward. It depends strongly on the particular experimental setup, as well as the arrangement of its components. For instance, for a given calibration, the experimenter should keep fixed the sample geometry, longitudinal and transversal position of pump and probe beam waists, to cite a few. Ideally one should perform the calibration by generating a reference thermal lens inside the material – which is not practically possible. Instead, one relies in the modeling of the whole experiment, which depends on the precise knowledge of several physical properties of the analysed sample and the use of a good model, which is difficult even for well-known materials [123], for instance bulging has been shown to account to almost half of the TL-measured thermo-optic coefficient of a Nd:YVO_4 rod [151].

Since PTDS is based on the refractive index changes, one needs to distinguish between contributions from the temperature change to the contributions from the pump-induced population changes in the ground and excited states, which modifies the absorption, thus the broadband refractive index [26, 152]. While this population-lens effect is important to be measured for laser design, and although it can be compensated [153, 154], it poses an additional complication to

recover the temperature in laser cooling experiments. In general, while providing a fast way to qualitatively measure the heating/cooling of samples, as shown in the first experimental demonstration of optical cooling of solids [19], PTDS does not provide readily the absolute value of the local temperature. Another approach of relatively simpler analysis, based on thermo-optical properties, could be implemented by measuring the total optical path length change of the sample rather than its gradient, which can be done for example using interferometry, discussed in the next section.

4.1.1.3 Thermo-optical method – Interferometry

Another thermo-optical method of temperature measurement based on phase-shift is the interferometric method. As in the photothermal deflection technique, a temperature change modifies the samples local refractive index, as well as its length, thus changing the local phase of a passing optical beam. To measure temperature-induced path-length modification, one has simply to place the sample in one arm of an optical interferometer, and monitor the relative phase between the beam traversing the sample and a reference beam from the same optical source.

The phase difference $\Delta\phi$ of the interfering beams is therefore given by (4.1) [155], where ϕ_0 is an arbitrary constant.

$$\begin{aligned} &\frac{\Delta\phi(T)}{2\pi} = \frac{p_{\mathrm{L}} L(T)}{\lambda}\left(n(T) - n_0\right) + \phi_0, \\ &\Rightarrow \frac{d\Delta\phi}{dT} \cong \frac{2\pi}{\lambda}\, p_{\mathrm{L}} \left\{\left(n(T_0) - n_0\right)\frac{\partial L}{\partial T} + L(T_0)\frac{\partial n}{\partial T}\right\}, \end{aligned} \tag{4.1}$$

where T, L, n, n_0 and λ, are respectively the temperature, length and refractive index of the sample, the refractive index of the reference arm and the wavelength of the optical source. p_{L} is the number of beam passes inside the sample, which depends on the particular configuration, e.g. $p_{\mathrm{L}} = 1$ in a Mach-Zehnder interferometer and $p_{\mathrm{L}} = 2$ in a Michelson interferometer. The quantity in brackets has been found to be $= -L \times 6.6 \times 10^{-6}$ K^{-1} for Tm^{3+}:ZBLANP [156], i.e. approximately 0.07 K^{-1} phase change in a 10 mm-long sample, thus a sub-K resolution can be achieved in a simple interferometric setup.

Contrary to PTDS, interferometric thermometry can be used to estimate the temperature of the bulk sample, since it does not need a thermal gradient therefore can probe an unpumped region, or where the pump profile doesn't change significantly. It is rather surprising why the interferometric

technique is not widely used in laser cooling experiments, but one of the possible reasons is the need of an additional laser beam in the optical setup, as well as the sensitivity of the technique to vibrations and path length changes e.g. in the chamber windows. Interferometric measurements have been reported in only three laser cooling experiments, one with cooling [156]. Only heating was observed in the other two experiments [157, 158], including in a Yb:YAG sample from Scientific Materials [157], for which a similar sample had been optically-cooled [34, 122].

4.1.1.4 Thermal cameras

The first successful quantitative measurement of the temperature in a laser cooling of solids experiment [19] was made with the use of a thermal camera. In that experiment, the temperature of a Yb:ZBLAN sample was measured using a liquid-nitrogen-cooled indium antimonide (InSb) infrared camera, sensitive in the 3 μm – 5 μm wavelength range. Since ZBLAN is transparent at wavelengths below 5 μm, they had to attach a tiny gold mirror with a blackened back surface attached to the sample, which lead to other complications such as absorption of the fluorescence. A way of circumventing this limitation, as well as avoiding the use of cryogens is the use of broadband thermal cameras, based on micro-bolometers. Bolometers are however less sensitive than photodetectors, thus cannot be employed in low-intensity blackbody radiation present in cryogenics optical refrigeration, and can be limited by the target material transparency. For instance, KPb_2Cl_5, an important laser cooling host, is transparent in the mid-IR window where the micro-bolometers are sensitive [159]. Although popular low resolution devices have started to become available in the market, research-grade thermal cameras are expensive and their use depends on specific mid-IR transparent optics. The main advantage of the technique is the readiness for operation.

Although the use of a thermal camera is a fast way to obtain qualitative results, the interpretation of the signal can be tricky. Not only the fact that different materials have different emissivities to be compensated for, but one must take into account the sample thickness, surface roughness, the background temperature for semi-transparent samples, to cite a few. For powdered samples, the effective emissivity is generally higher than the corresponding solid and increases with porosity [160]. Low resolution can also be an issue for exploratory experiments where the temperature change is small, e.g. [37] reports the use of a thermal camera with 0.1 K resolution to measure a total signal of 0.3 K. Despite these constraints, the technique is extensively used in laser cooling

experiments [22, 23, 47, 122, 161-167] and sometimes presents problems such as detector saturation [167], preventing temperature collection during the whole experiment.

4.1.1.5 Brownian motion tracking, perspectives

It is a well-known fact that a microscopic object immersed in a fluid will undergo Brownian motion – a random motion due to the collision with the fluid particles. The first explanation of the Brownian motion was given by Einstein [168], and confirmed experimentally by Perrin [169] – a difficult task which contributed to the latter being awarded a Nobel prize, due to its deep consequences to the understanding structure of matter. Nowadays the tracking of the Brownian motion of particles can be made automatically, with the help of video microscopy [170] and computer analysis [171], and laser scattering data [172].

The temperature of a fluid can be estimated by the measurement of the mean square displacement $<r^2>$ of a particle immersed on it, due to Brownian motion, and can be quantified by the equation (4.2) [173].

$$T = \frac{\pi \eta_f(T)}{k_B \Delta\tau d_n} r_p \langle r^2 \rangle, \tag{4.2}$$

where $\eta_f(T)$, r_p, k_B, $\Delta\tau$ and d_n are respectively, he viscosity of the fluid, the particle radius, the Boltzmann constant, the observation time interval and the dimensionality.

The relation of temperature and mean square displacement as shown in (4.2), is deduced from Stokes-Einstein diffusion theory, and assumes thermal equilibrium between the fluid and the particle, which is not the general case in laser cooling. The same problem arises in the study of hot trapped particles, and one can assign an effective temperature [174] to the solvent of well-known thermo-physical properties, as the temperature of a isothermal gas that would cause the same Brownian fluctuations of the particles [175].

4.1.2 Direct methods of temperature measurement

The direct thermometric methods are based on the zeroth law of thermodynamics. The temperature of the sample is measured by knowing the temperature of the sensor in thermodynamic equilibrium with the sample, and if the sensor is calibrated, one can assign an absolute temperature to the

sample. It implies that the measurement of the temperature is independent on the internal processes occurring inside the sample.

4.1.2.1 Platinum resistor

While platinum resistors, or resistance temperature detectors (RTDs) were not used directly in laser cooling experiments, these sensors are easy to use, are accurate and reliable. The temperature is estimated by measuring the resistance between the two leads of the sensor. Since it uses precisely trimmed platinum embedded in glass or ceramic, it does not change its properties with time, and it is interchangeable. Due to these properties, they are used in all experiments which require calibration using a third sensor. The main reason they are not used directly in laser cooling experiments is the relatively large size. Instead, the contact thermometer of choice for initial laser cooling experiments is the thermocouple; 50 μm-diameter versions can be easily found commercially.

4.1.2.2 Thermocouples

Thermocouples (TCs) were the first sensor to be used to monitor the temperature of a solid upon optical refrigeration [15]. Although in that first work no refrigeration was observed, TCs were used later in successful laser cooling experiments [159, 176-179]. The physical principle of the thermocouple is based on the Seebeck effect, in which a voltage is produced between two regions submitted to different temperature in a metal. The potential difference in a thermocouple depends on the temperature difference of its tip (measurement junction) and its reference junction (cold junction). One of the several ways of measuring temperature using a thermocouple is shown in Figure 4-5.

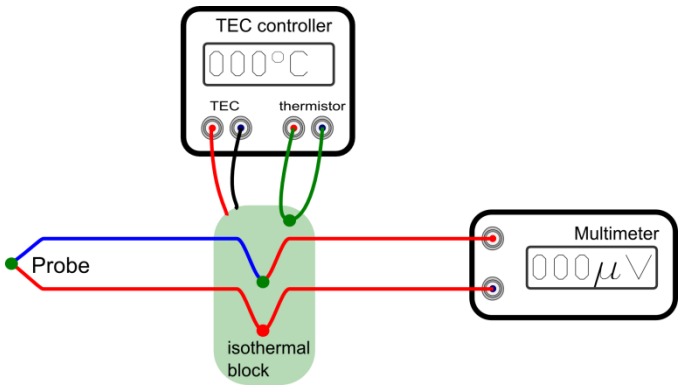

Figure 4-5: Interrogation scheme for the measurement of temperature using a thermocouple, with active control of the reference junction temperature.

While TCs are an ubiquitous temperature sensor, they have some drawbacks, especially in laser cooling experiments. The intrinsic drawbacks are, 1) the need of a reference with temperature as stable as the desired resolution one wants to measure, and 2) the small signal produced when the reference temperature is close to that being measured, thus making the measurement more prone to noise. In optical cooling experiments, other drawbacks emerge: 3) the size of the sensor and 4) its opaqueness. The former can be solved easily by choosing a small enough TC – but this often means handling a very fragile sensor, and which can present drift due to morphological and chemical changes. Since it is metallic, it also can be a significant source of heat load due to heat conduction along the wires. The opaqueness introduces a constraint: the thermocouple must have an automatic positioning system, and cannot measure the sample temperature during optical pumping – otherwise it will absorb the emitted fluorescence and will warm up.

In this work, due to the relative simplicity, and – being a contact method – reliability, the initial optical cooling experiments used a fine wire micro-thermocouple. At first an active heat bath as the cold junction plate was designed. It consisted of a carbon paper receptacle coupled thermally to a copper plate whose temperature is measured by a thermistor and controlled by a thermoelectric cooler. The system is isolated from the environment by Styrofoam walls, and a thin Teflon tube guides the thermocouple inside the receptacle. This system works very well, and does not require the preparation of a passive bath – which could take hours or days, and would last only a few days. The active system requires maintenance – due to thermal paste drying and moving parts – and the proximity of a fan used to cool the thermoelectric plate inserts vibration and air flow in the system.

It is therefore an additional source of errors, thus a simpler and more compact solution is desired in the long term. Electronic cold junction compensation is well known and widely used in handheld thermocouples. These often come with poor resolution and depend on the internal temperature of the interrogator, measured by a thermistor. Since the signal of a thermocouple is the voltage generated by the Seebeck effect, is becomes very small – and susceptible to noise – when the TC leads are at a similar temperature as the TC tip. The circuitry used in the electronic cold junction (ECJ) is composed of dissimilar metals, thus can produce a significant Seebeck voltage which may overcome those from the TC. In order to avoid these problems, a TC interrogator was assembled, consisting of a precise electronic cold junction compensator and an ultra-low-noise amplifier, tightly packed and thermally coupled with thermal paste, insulated inside a matchbox-sized aluminum box and fed by a stable voltage from 9V batteries. The amplified output is sent by an SMA cable to a benchtop multimeter, which is read by a computer with MATLAB. Due to its external simplicity and compactness, the interrogator is attached directly to the cooling chamber so that no extension leads are required.

For the TC and ECJ calibration, both the TC and RTD are placed in contact, inside an environmental chamber, and the reading of the sensors are compared when the RTD temperature is stable to within 20 mK/measurement, i.e. ~ 20 mK/s. The steady-temperature points are shown in Figure 4-6, together with the best quadratic polynomial fit.

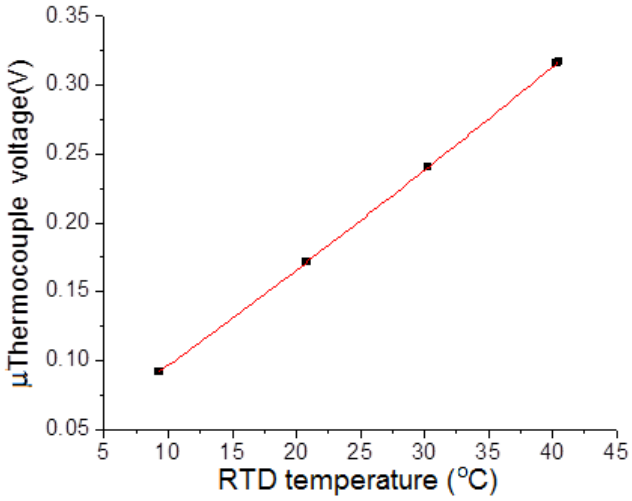

Figure 4-6: Calibration curve of the microthermocouple, showing its voltage versus its temperature measured by a RTD, as well as the best quadratic curve fit (red).

From Figure 4-6, one can find which function relates the measured voltage to the μTC absolute temperature T as $V_{\mu TC}(T) = [21(2) + 6.9(1)\times(T - 273.15\ K)/K + 0.008(1)\times(T - 273.15\ K)^2/K^2]$ mV, indicating a temperature coefficient of ~ 7 mV/K, which is much easier to measure than the intrinsic coefficient ~ 50 μV/K without amplifying electronic cold junction compensation. Since the thermocouple cannot be used during pumping, a microcontroller was programmed, allowing the final and initial position to be set of a servo-motor, which holds the TC, and another motor which flips a shutter mirror. Thus the TC is precisely placed on the top of the sample as soon as the pump beam is blocked, and leaves it before the pump is allowed to pass. A photo of the supporting setup is shown in Figure 4-7. It uses a series of plastic tubes of different diameters which prevent the fine wires from twisting at the end, as well as for strain relief and fine tuning the curvature of the sensor tip.

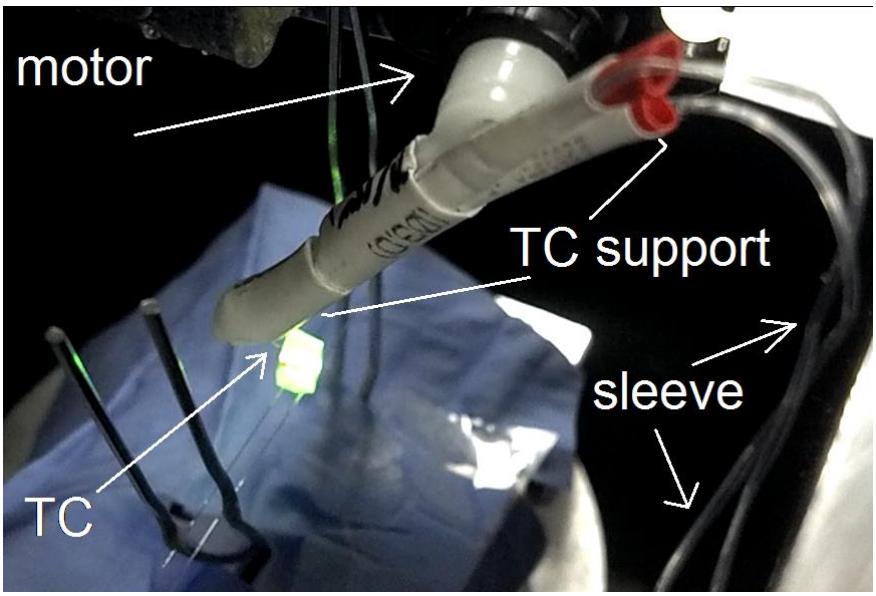

Figure 4-7: Photograph of the inside of the cooling chamber in initial tests. A small servo-motor controls the position of the thermocouple support. The 1-mm^3 sample (green) is pumped on purpose so that it is easier to see the thermocouple due to the green light scattering.

After confirmation of the reliability of another contact method (fiber Bragg grating, described later in the thesis), the thermocouple was used for monitoring the chamber temperature only, and not the sample temperature.

4.1.2.3 Two-band differential spectral metrology

The physics behind the two-band differential spectral metrology (2BDSM) is the same as the PTDS discussed in the section 4.1.1.1. The main difference relies in the fact that the measured luminescence in the 2BDSM originates from a probe placed on the surface of the laser cooled material instead of being the material itself, as in DTL.

The technique was developed by Seletskiy [28], who used a gallium arsenide (GaAs) plate as the luminescent probe, pumped with a low power probe laser operating at a 650 nm wavelength. The luminescence from the probe is collected by a 600 μm diameter optical fiber, then separated in two spectral bands by a monochromator and each portion of the separated light is directed to a balanced photodetector, and the results displayed on an oscilloscope. In the 2BDSM, the signal is proportional to the point intensity of the luminescence $I(\lambda,T)$ as:

$$S_{\mathrm{2BDLT}}(\delta\lambda,T)=\frac{I(\lambda_1,T)-I(\lambda_2,T)}{I(\lambda_1,T)+I(\lambda_2,T)}, \tag{4.3}$$

where λ_1 and λ_2 are the two detected wavelengths. It can be seen from (4.3) that the signal is unaffected by fluctuations in the probe laser power. The technique has several advantages over the previous PTDS method. Firstly, the temperature is measured at the surface of the material, thus providing a signature of bulk cooling/heating instead of only local cooling/heating. Secondly, one does not have to compensate for any effects occurring inside the sample, which could otherwise distort the signal and be difficult to interpret. Thirdly, as with all the direct methods, once the probe is calibrated, the measured sample can be changed without the need of a recalibration of the system.

There are some factors which prevents the use of the 2BDSM in laser cooling thermometry. The first is a problem of availability: the GaAs probe is not available off-the-shelf. While one research group has applied the technique in several experiments [26, 27, 58, 180-182], the application of the method depends on a several components, and requires careful optical alignment so that the calibration corresponds to the reading during the cooling experiment. Additionally, the photoluminescence curve calibration is valid for a fixed value of optical power at the probe [183], thus may also be sensitive to the fluorescence from the cooled device. Since it is a pump-probe technique, it depends on the temperature variation to provide an accurate reading. Thus, long term measurements are not feasible. The last drawback relates to its relative opaqueness. While a thin high-purity GaAs probe is transparent at current laser-cooling bands centered at wavelengths 1 μm,

1.5 μm and 1.9 μm, it is opaque for wavelengths below 900 nm, thus cannot be used for evaluating new materials which can emit in this region. All these issues can be solved by the use of a passive optical fiber sensor, as it will be discussed in the next section.

4.2 Fiber Bragg gratings

Fiber Bragg gratings (FBGs) are an ubiquitous optical component, being used in fiber lasers, optical signal manipulation and contact temperature sensing to cite a few [184]. FBGs have been used as temperature sensor in harsh environments, from explosive atmospheres to nuclear reactor cores. FBGs are insensitive to below-optical-frequency electromagnetic radiation, have low chemical and optical sensitivity, and have small a footprint, constituting a remarkable temperature sensor [184]. The most common type of FBG is based on a silica fiber, which is transparent in the range 300-2000 nm, and which makes it suitable for sensing under intense fluorescent light in a LICOS experiment. It also constitutes a very small heat load, given its small radius of 125 μm, which can be further reduced typically down to 14 μm [185], and may even be written inside the cooled material.

There are many ways of fabricating a FBG. The one used in the present work was fabricated using a 213 nm laser [186], using a Talbot interferometer [184]. An overall diagram of the writing and interrogation of a FBG is shown in Figure 4-8. In this diagram, two laser beams from the same ultraviolet source are made to interfere at a focus where an optical fiber is placed. The photosensitive core undergoes a periodic modification on its refractive index, with the same spatial period as the interference pattern. Light from a broadband source is injected in the fiber core, and a narrowband undergoes multiple small but resonant reflections, adding to a significant reflected power, and a dip in the transmission spectrum.

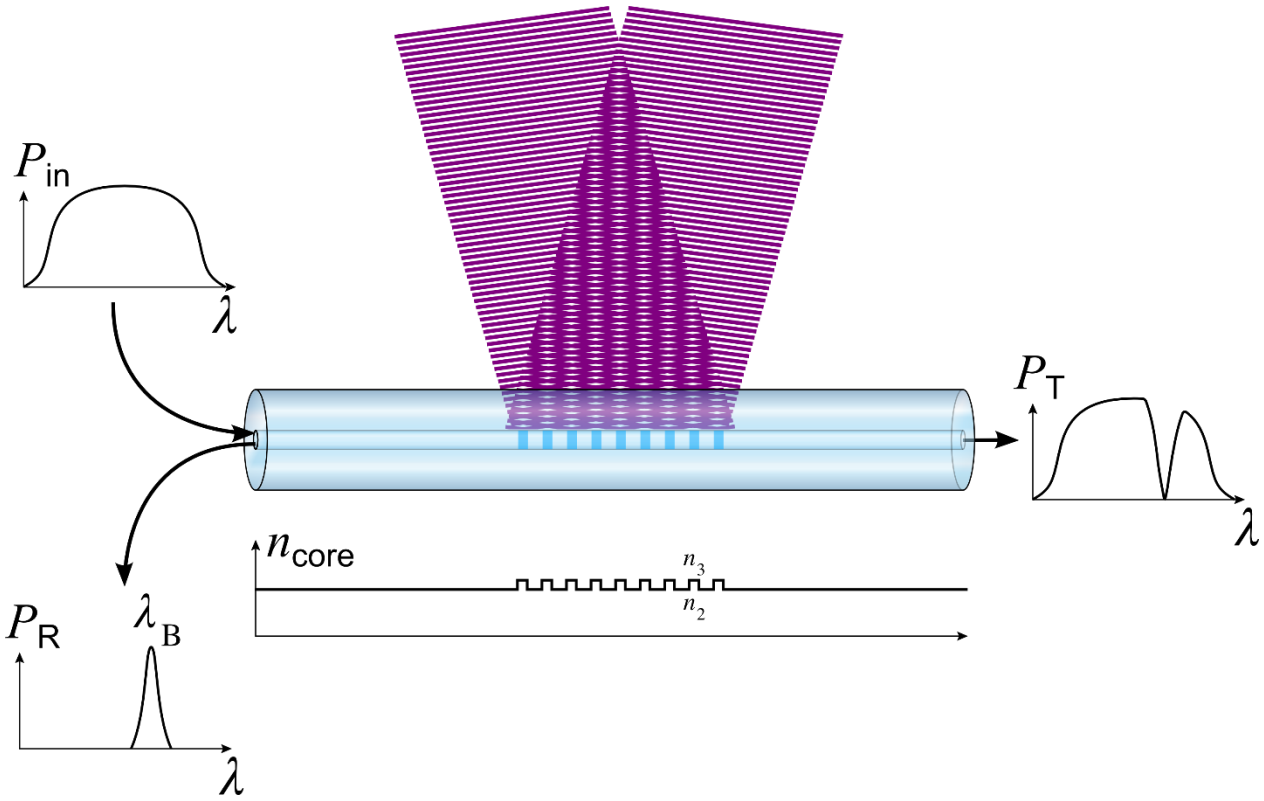

Figure 4-8: The principles of fiber Bragg grating inscription and operation. The FBG is placed in the interfering region of two laser beams, and the refractive index of its core is periodically modified. A broadband source injected to the fiber has its power filtered at the Bragg wavelength λ_B, thus present a sharp reflection and a dip in the transmission.

The reflection peak λ_B, called the Bragg wavelength, is related to the spatial period of refractive index modulation Λ and the effective mode index in the fiber n_{eff} by $\lambda_B = 2n_{eff}\Lambda$. A temperature change of the FBG modifies its geometry, and therefore changes Λ, but mainly modifies the effective index of the propagating mode. These changes are represented by an overall thermo-optic coefficient ξ, which leads to a change of the Bragg wavelength with changes of the temperature:

$$\Delta\lambda_B = \lambda_B \xi \Delta T. \tag{4.4}$$

Numerous methods of detecting the Bragg wavelength shift $\Delta\lambda_B$ have been developed. Usually, spectral methods are slow and have low sensitivity, but are accurate and do not need prior calibration. For the LICOS experiments described here, power at a single-wavelength method was used, which is referred to as the Bragg wavelength interrogation by monochromatic power

(BWIMP). Owing to the steep slope of the FBG spectrum at the edge of the bandwidth, one can have a high variation in the reflected or transmitted monochromatic power for a small variation in the temperature. To assess this sensitivity, a thermistor, a platinum resistance temperature detector (RTD) and a FBG were placed in a copper block inside a Styrofoam box, and the temperature allowed to change passively over 8 h. A laser tuned to the long-wavelength edge of the FBG main peak was launched into the FBG and the transmitted power was read in a power meter. The signal from the three sensors is plotted in the Figure 4-9.

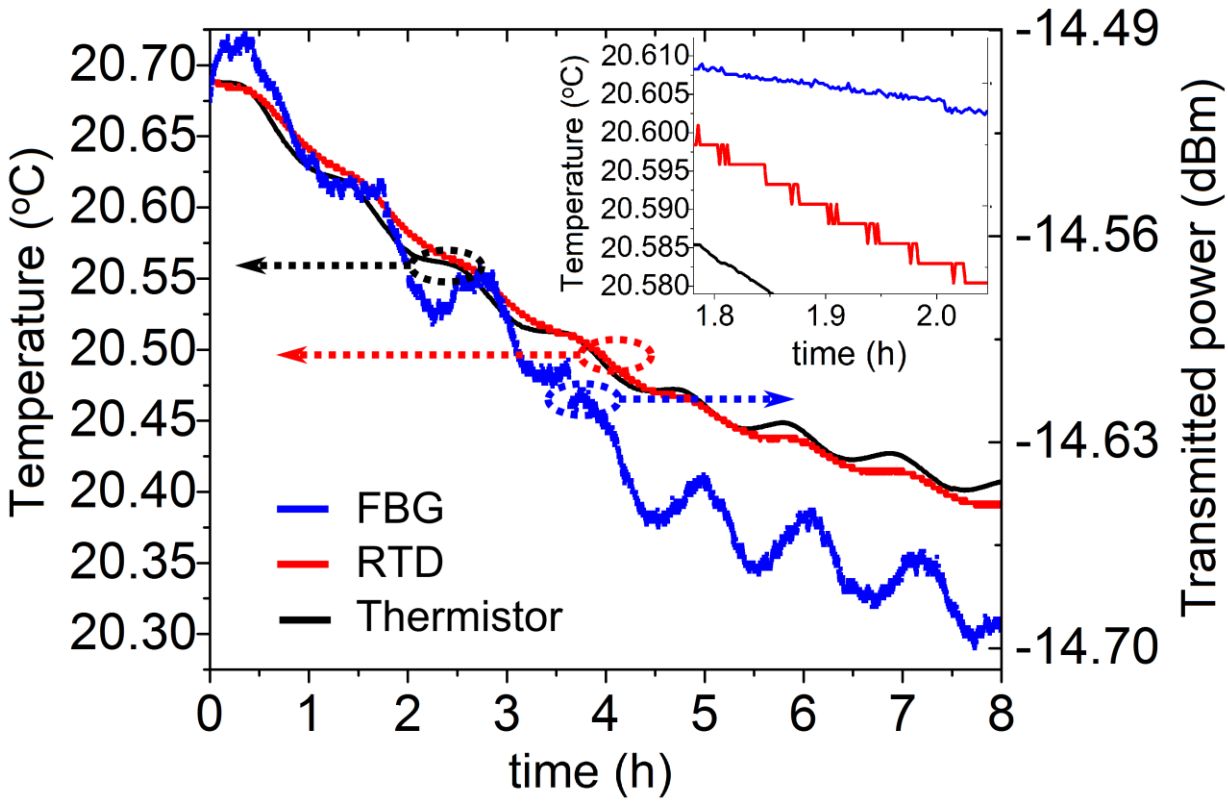

Figure 4-9: Temperature variation over time in an insulated copper block, as measured by a thermistor (black) and RTD (red), and qualitatively by the narrow-wavelength laser probe transmitted though and FBG (blue). Inset: Zoom at a region of monotonic temperature change.

By looking at a section of monotonic temperature change (inset in Figure 4-9), one can observe that the RTD has a resolution better than 3 K, and the variation of the FBG transmission corresponds to a temperature resolution of 750 μK. This technique is faster and more sensitive than

spectral methods, but requires prior knowledge of the FBG spectra (Figure 4-10), and is susceptible to wavelength drift of the probe laser. When a wide range of temperatures can be expected, it is better to have a weaker FBG, with a wider reflection edge bandwidth, so that one does not reach the top or bottom of the slope (Figure 4-10b), where the relation between power and wavelength cannot be represented as a unique single valued function. An alternative way to solve this problem is to use a reading algorithm which forces continuity to the measured value, similarly to phase-unwrapping used in interferometry [187]. The wider-slope is used rather than the latter approach, so that the measured signal is free of calculation errors, and is thus unambiguous.

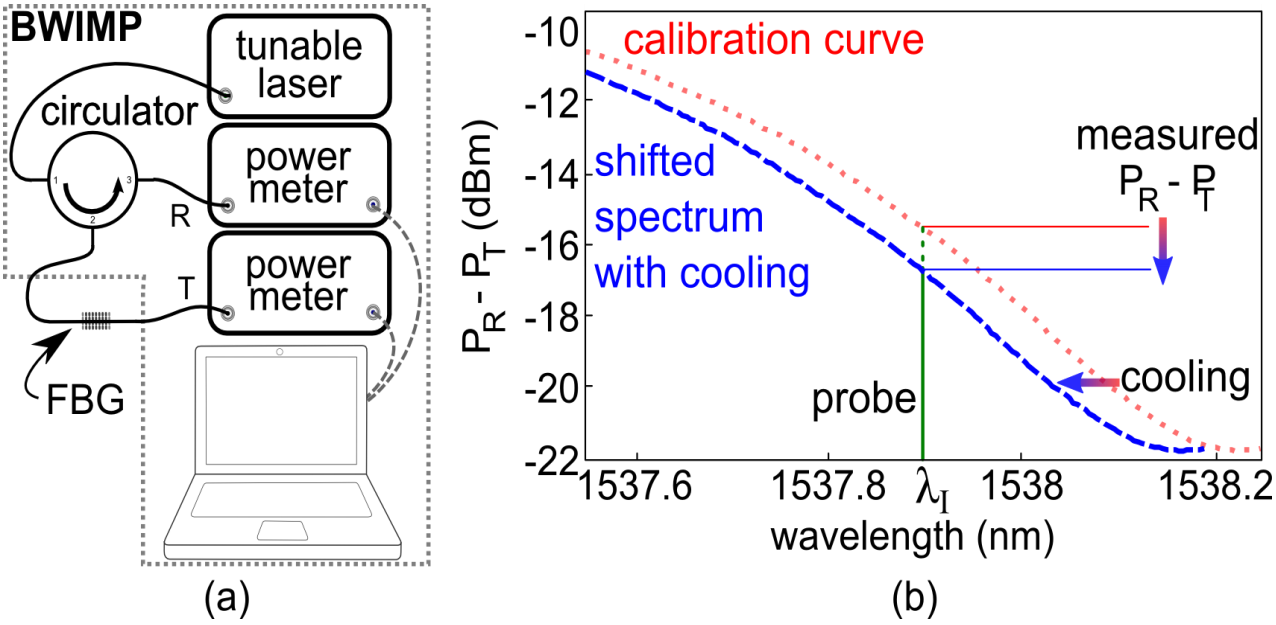

Figure 4-10: FBG interrogation method based on reflected and transmitted power. (a) Experimental setup. (b) Measured reflection/transmission power spectra from the FBG before the cooling experiment (right). The curve on the left is a representation of the shifted spectra after a temperature drop, and the corresponding power change measured by the power meters when the fiber is interrogated at a single wavelength λ_I (continuous line). Notice that at the bottom of the P_R - P_T, one cannot assign a single wavelength to a given measured power.

For calibration, a broadband source is connected to an optical circulator, with the second port connected to the FBG. The reflection is directed to the circulator's third port and measured by an Ando AQ6317B optical spectrum analyser, controlled by a PC. For measurements of $\Delta\lambda_B$ during cooling, the shift in the Bragg wavelength within the FBG's bandwidth, the circulator's input port

is connected to a narrow linewidth laser source at wavelength λ_I and the reflected, P_R and transmitted P_T powers, respectively, are measured by optical power meters, interrogated by a PC. A computer code written in MATLAB® controls the instruments and determines the corresponding $\Delta\lambda_B$ from the calibration curves P_R (λ), P_T(λ), the chosen value λ_I and the measured P_R and P_T.

4.2.1 Low temperature measurements with FBGs

Although low temperature optical cooling is not experimentally studied in this thesis, a sensor to be practical for optical cooling must demonstrate cryogenic capabilities. It happens that the sensitivity of an FBG decreases with decreasing temperature, and the way it happens is not well established. This was the motivation to pursue an investigation on the behaviour of the FBGs at low temperatures. Here, the experimental setup used in the investigation is presented, as well as the main results. The full discussion on the modeling and the FBGs material properties are given in Ref. [188].

It has been noticed that sensitivity to temperature of the wavelength of a standard FBG is around five-fold smaller at 77 K (LNT) than it is at 295 K (RT), in addition to being a nonlinear function [189, 190]. The values presented in the literature vary widely [189-192], and could be attributed to the use of different fabrication processes and coatings, to the different compositions of the fibers, or in some cases, poor resolution of the bare FBG measurements. For FBGs to become ubiquitous in the cryogenic regime, further studies must be performed. Here three different fibers are used – including one with no dopant in the core, and a high-density of measurements in the temperature domain are taken to make sure discontinuities, which were observed in a previous report [190], are not missed.

4.2.1.1 FGB fabrication

Three FBGs made from different materials were fabricated, in order to assess the composition effect on their low-temperature behaviour. The 3 mm long FBGs were produced using a Q-switched 100 mW Xiton Photonics laser source operating at a wavelength of 213 nm, as described in [186]. The laser produces pulses of 7 ns duration with an energy of 10 μJ. The gratings are imprinted using the scanning phase-mask interferometer technique [184]. A mirror on a linear translation stage was used to scan the fiber, and a cylindrical lens of 20 cm focal length is used to

focus the light on the fiber, which is held at the intersection of the beams, using a PhotoNova Inc. BraggTune® Interferometer. The details of the three FBGs are summarized in the Table 4-1.

Table 4-1: FBG's details

Label	**Fiber type**	**Manufacturer/Part#**	**λ_B(RT) (nm)**
BorFBG	Boron/Germanium-doped silica core, photosensitive	Redfern	1549.06
GerFBG	Germania-doped silica core, standard	Corning, SMF 28	1552.40
PurFBG	Pure silica core, fluorine-doped cladding	Fibertronix, FX-PC-SM-01-01-01	1523.83

Although GerFBG and PurFBG are not intrinsically photosensitive, all the FBGs were written in non-hydrogenated fibers, using ns-long 213 nm radiation pulses, rather than the femtosecond lasers typically used for these fibers. The reflection peak of the PurFBG is weak compared to the other FBGs, thus its spectrum could not be measured in transmission. The reflection spectrum of the PurFBG and the transmission spectra of the others are shown in Figure 4-11.

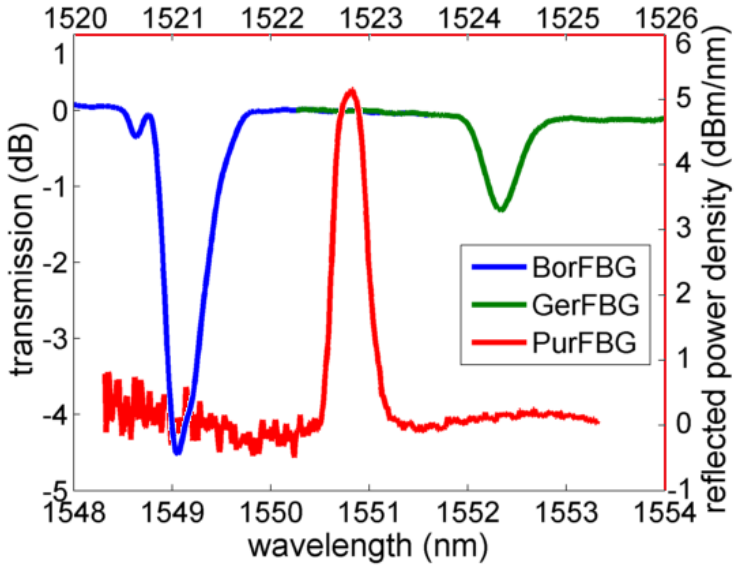

Figure 4-11: Spectra of the fabricated FBGs. Bottom and left axes: Transmission of the BorFBG and GerFBG. Top and right axes: Reflection of the PurFBG, normalized to the profile of the probe.

Since the operating wavelength of the PurFBG is on the unflatened, low power, left tail of the broadband erbium-doped fiber probing source (BBS), its reflection spectra shown in Figure 4-11 is the reflection data normalized by the spectral profile of the BBS. All the fibers had their coating stripped-off at the FBG section. Since the fibers have no coating and are not embedded in a substrate, they are referred to as “bare fibers”, avoiding the ambiguous definition of “non-embedded”, which can include coated fibers as well as uncoated ones.

4.2.1.2 Passive temperature sweep from 77 K to 295 K

In order to characterize the FBGs, a passive temperature sweeping system was used, consisting of a minichamber which is allowed to exchange heat slowly with two temperature baths, laboratory air and liquid nitrogen (LN_2). A diagram of the experimental setup is shown in the Figure 4-12. The mini-chamber is an aluminum circular rod of 25 mm height and 25 mm diameter, with two ports around its center, one with a pt-100 platinum resistor (RTD) and a steel needle of 780 μm outer diameter as the fiber receptacle. Both the RTD and the needle are placed in holes filled with thermal grease. The fiber is cut after the FBG, inserted into and attached to the upper side of the receptacle, thus it is free to move longitudinally with negligible friction. The small diameter of the needle allows little or no temperature gradients inside it, and together with the high thermal emissivity of silica, provide good thermal coupling between the aluminum rod and the FBG. A small volume of 0.25(10) L of LN_2 is placed in a 1.0 L glass dewar, where the mini-chamber is subsequently immersed without touching the bottom of the dewar, and the top of the dewar is closed with aluminum foil to prevent turbulence from room air. This allows overnight evaporation of all LN_2 while keeping the mini-chamber temperature steady enough to allow thermalization between the sensors.

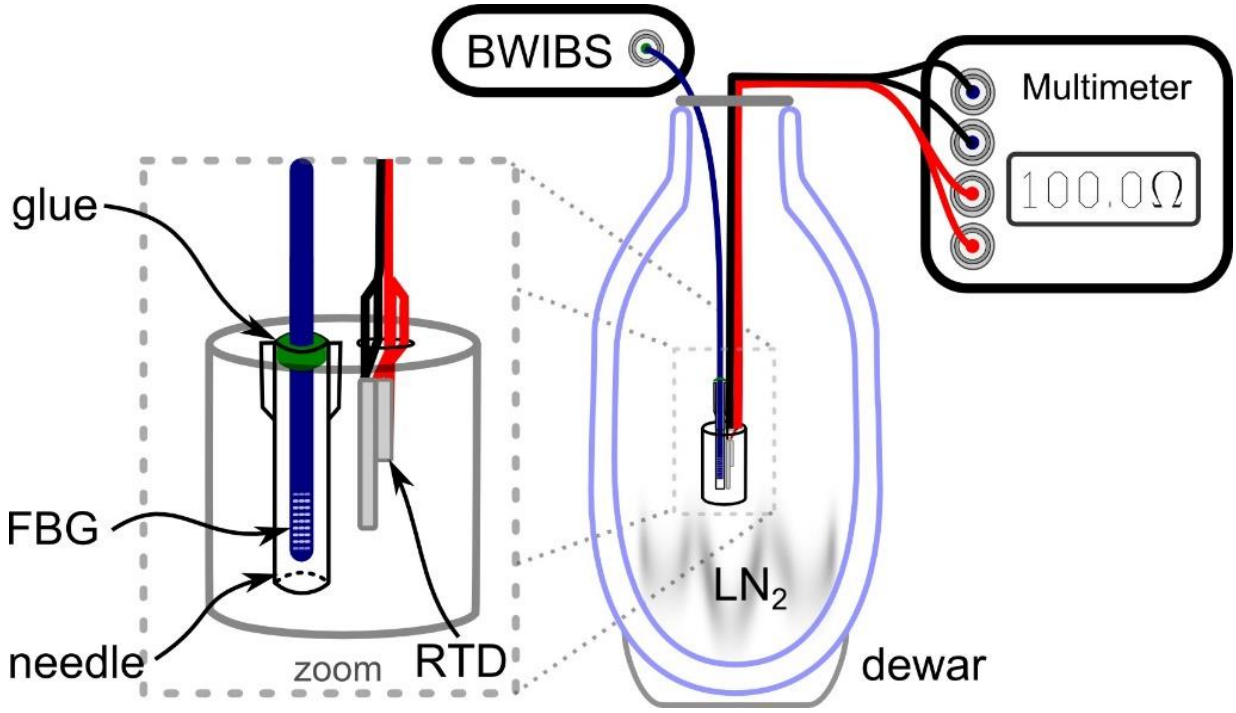

Figure 4-12: Temperature control microchamber diagram. The diagram of the Bragg wavelength interrogator with broadband signal (BWIBS) is shown in Figure 4-13.

Due to the large range of temperatures involved, the electrical resistance variation of the RTD wires must be compensated, which is done by a 4-wire resistance interrogation scheme using an Agilent 34401A benchtop multimeter. The measured resistance is converted to temperature using a 6th order polynomial which is fit to the inverse of the combination of both 2nd order (T > 273.15 K) and 3rd order (T < 273.15 K) Callendar-Van Dusen's resistance equation from [193], so that a single equation can be used for the whole measurement range: $T(R) = \sum_{i=0}^{6} \tau_i R^i$, where τ_0 = 31.336(4) K, τ_1 = 2.2002(3) K·Ω^{-1}, τ_2 = 34.295(62) × 10^{-4} K·Ω^{-2}, τ_3 = -18.617(62) × 10^{-6} K·Ω^{-3}, τ_4 = 74.33(31) × 10^{-9} K·Ω^{-4}, τ_5 = -14.521(7) × 10^{-11} K·Ω^{-5} and τ_6 = 11.551(70) × 10^{-14} K·Ω^{-6} are the fitted coefficients of $T(R)$, which provide a root-mean-square deviation of 13 mK in the range 65 – 350 K.

4.2.1.3 Wide-range FBG interrogation system

The reflection spectra of the FBG is measured by an ANDO AQ6317B optical spectrum analyzer (OSA) connected to the third port of an optical circulator (Figure 4-13), whose first port is fed by a C-band broadband source (BBS) model BBS 1560+2FA00 from JDS Uniphase. The optical

circulator transmits the power from the first to the second port, where the FBG is connected. The reflected power from the FBG enters the second port and is directed to the third port.

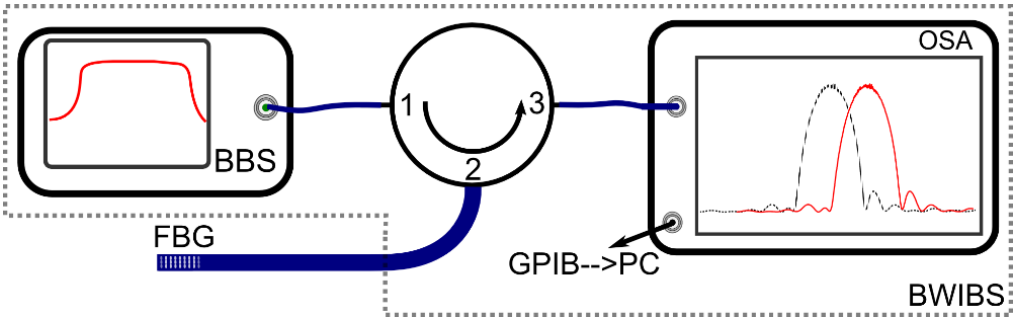

Figure 4-13: A schematic diagram of the Bragg wavelength interrogator with broadband signal (BWIBS) and a FBG.

The FBG reflection spectra is then measured by the OSA with a 500 pm resolution, and has its center wavelength λ_{THR} determined to within 1 pm resolution using the 5 dB envelope threshold function (THR) of the OSA. A personal computer then extracts both the spectra and λ_{THR} information from the OSA. The Bragg wavelength resolution can be further increased with digital processing of the spectra. A six-order Fourier (F6 method) series presented a good fit to the reflection spectra of all the FBGs, thus it was used to calculate the Bragg wavelength shift $\Delta\lambda_{B,F6}(T) = \lambda_B(T) - \lambda_B(RT)$ with a resolution $2\sigma < 0.2$ pm for the BorFBG and GerFBG, and $2\sigma < 0.5$ pm for the PurFBG.

4.2.1.4 Results on the FBGs behaviour at low temperatures

Assuming that the FBGs are at the same temperature as the RTD, one can plot the Bragg wavelength shift as a function of the RTD temperature, as shown in Figure 4-14. One can easily see some anomalous data for the BorFBG at ~ 85 K when using the THR method during the cooling process. Using exactly the same raw spectrum, but analysed with the F6 method, the previously anomalous points lie on a smooth curve. During the slow minichamber thermalization, or heating, the data from both methods overlap. The analysis concentrates on the data during the heating process, since it is slower than the cooling, as more time is allowed for the FBG and the RTD to thermalize. No hysteresis was observed in any of the FBGs, as expected for both Germania and boron-doped silica, but so far unknown for F-SiO_2, whose CTE presents hysteresis at high

temperatures [194]. Due to the poorer resolution of the THR method, and possible misreading, only the data from the F6 method are considered, which is shown in the Figure 4-14 for all the FBGs.

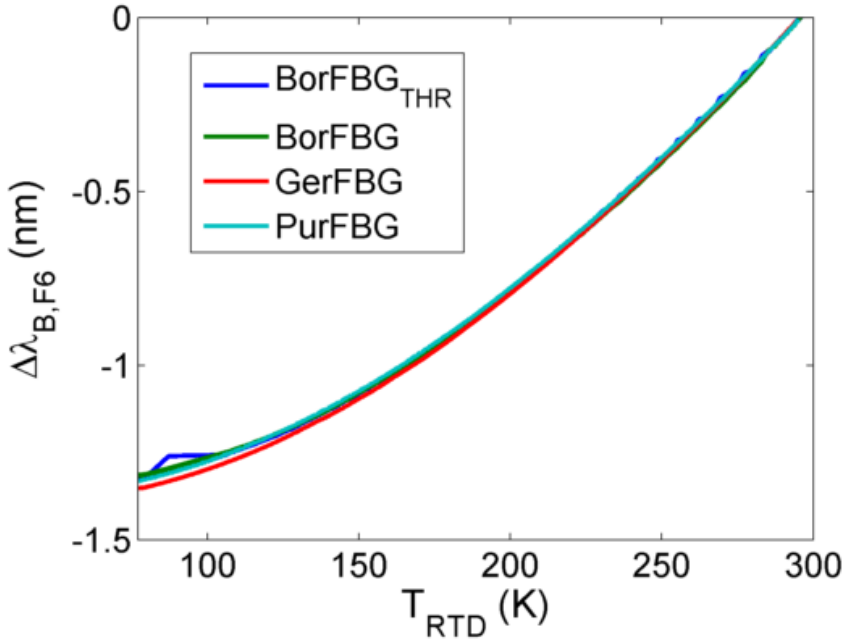

Figure 4-14: Total Bragg wavelength shift as a function of the RTD temperature, as recovered by the F6 method for the three FBGs and by the THR method for the BorFBG (in blue color). The abscissa error is smaller than the graph line width.

From the data shown in the Figure 4-14, one can fit a degree 3 polynomial to each Bragg wavelength curve $\lambda_B(T) = \Sigma_p \lambda_p T^p$, with the coefficients λ_p given in the Table 4-2.

Table 4-2: Bragg wavelength coefficients

coefficient \ FBG	BorFBG	GerFBG	PurFBG
λ_0 (nm)	1547.8819(2)	1550.8793(1)	1521.4620(3)
λ_1 (× 10^{-3} nm/K)	-2.7808(32)	-2.4224(27)	-1.9696(51)
λ_2 (× 10^{-5} nm/K^2)	3.0644(20)	3.0467(16)	2.7772(30)
λ_3 (× 10^{-8} nm/K^3)	-2.2558(37)	-2.3234(30)	-1.9865(53)

By simply taking the first derivative of the polynomial form of $\lambda_B(T)$, it is straightforward to calculate $\Psi_T(T)$ and thus $\xi(T)$ from the values shown in Table 4-2, using the expressions:

$$\Psi_T(T) = \left.\frac{\partial \lambda_B(T')}{\partial T'}\right|_T = \sum_{p=1}^{3} p\lambda_p T^{p-1},$$
$$\xi(T) = \frac{\Psi_T(T)}{\lambda_B(T)} = \frac{\sum_{p=1}^{3} p\lambda_p T^{p-1}}{\sum_{p=0}^{3} \lambda_p T^p}. \quad (4.5)$$

The wavelength temperature sensitivity $\Psi_T(T)$ is shown in Figure 4-15(a). In order to better quantify the fiber material properties, it is convenient to express the Bragg wavelength thermal coefficient $\xi(T)$, shown in Figure 4-15(b), rather than the Bragg wavelength sensitivity Ψ_T.

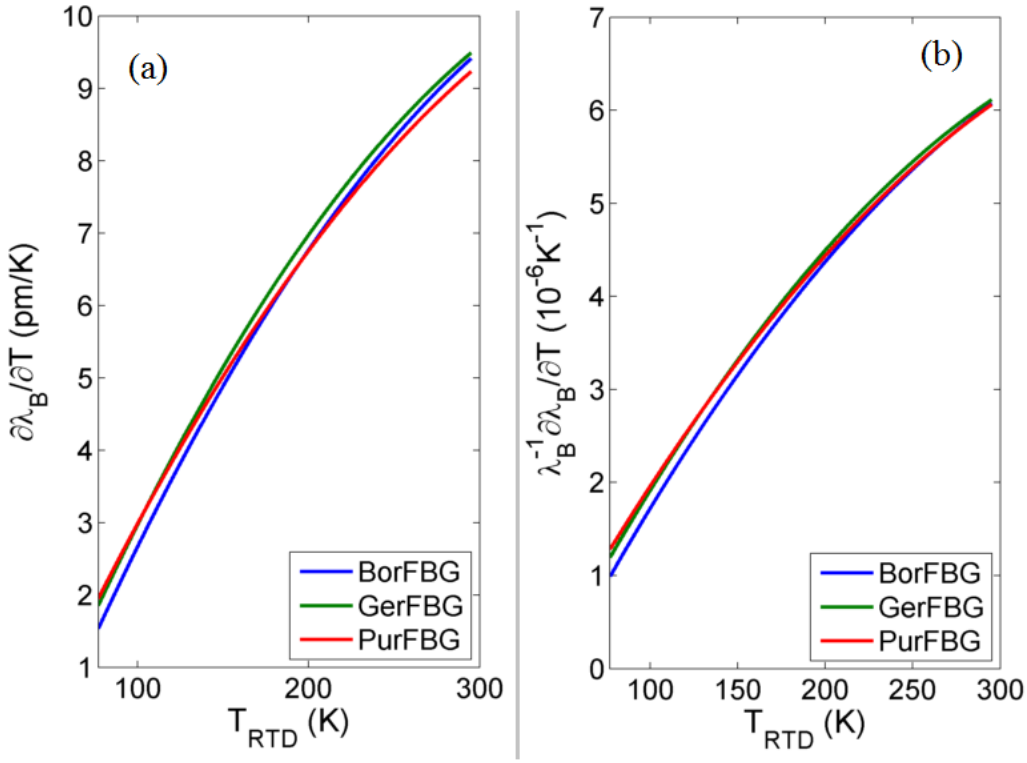

Figure 4-15: Temperature dependence of the three FBGs' sensitivity. (a) Bragg wavelength temperature derivative, Ψ_T for the three fibers, from the adjusted curves. (b) The Bragg wavelength thermal coefficient ξ, also for the three fibers tested.

The Bragg wavelength thermal sensitivity Ψ_T of the PurFBG at RT is smaller than for the other two FBGs. This can be explained due to the lower thermal expansion coefficient of the fluorine-

doped cladding compared to the pure-silica cladding of the doped fibers. Since the PurFBG was fabricated with a shorter Bragg wavelength than the others, one should expect a smaller absolute thermal sensitivity by a fraction equal to the ratio of its Bragg wavelength to the one of the other fibers. Here it is clear that the PurFBG has indeed a thermal coefficient ξ(RT) smaller than the other two FBGs, which have essentially the same ξ(RT). At LNT the effect is inverted and the PurFBG has the largest value of ξ.

One can clearly observe the nonlinearity of the FBG from the results shown in Figure 4-14 and Figure 4-15, as observed before by [189, 190]. Here a high density of points (~ 50/K) was used, and contrary to the quantitative values observed in some previous works [190, 192], a continuous nonlinear curve is obtained, with no anomalous effects or inflexion points in the temperature range from 77 K to 295 K. Surprisingly, the FBGs with considerably different composition, strength and center wavelength show essentially the same behavior at low temperatures. The use of the pure-silica-core FBG ruled out dopant concentration in the core as the main factor contributing for the observed nonlinearity. Coating effects were also eliminated as the bare FBGs are completely free to move inside their receptacle.

The FBGs' relative nonlinear sensitivities were shown to differ slightly, mainly due to different compositions. The nonlinearity can be accurately modeled using a temperature-dependent thermal expansion coefficient in conjunction with a nonlinear thermo-optic coefficient, as it is shown in details by Soares de Lima Filho [188]. Resolutions down to 0.5 K can be obtained using a weak pure-silica-cladding FBG and 0.25 K with boron-doped and germanium-doped silica fibers at liquid nitrogen temperature.

One issue to be addressed in the laser cooling community with FBG sensors is the divergent reports of their weak performance at cryogenic temperatures. The FBG behaviour could be measured and modeled from room temperature down to 77 K, without noticing any unpredictable problem with the technique. Sub-K resolutions can be obtained at 77 K and above, with common optical spectral analysers even at low wavelength resolution setting. With this issue resolved, the FBG can be compared with the other sensors used in laser cooling. A summary of the relative merits of the thermometric methods described in this section are presented in the Table 4-3.

Table 4-3: Principal thermometric methods used in optical refrigeration experiments, and their relative merits.

Method	Pros	Cons
Thermocouple	- Off the shelf - Accurate - Sensisive	- Cannot measure during pumping - Fragile - Sensitive to electromagnetic interference
Fiber Bragg grating	- Off the shelf - Accurate - Sensisive	- Cross sensitivity to stress requires care - Can suffer from probe wavelength drift, if not using a broadband interrogator
2BDSM	- Accurate - Sensitive	- Experimental-phase sensor - Limited wavelength range - Difficult mounting
Thermal camera	- Off the shelf - Minimal thermal load	- Material and environment dependent - Low sensitivity - May suffer from optical interference (parameter is cross sensitive)
Luminescence, DLT	- Sensitive - Minimal thermal load	- Material dependent - May suffer from optical interference (parameter is cross sensitive)
Thermal lens, PTDS	- Sensitive - Minimal thermal load	- Material dependent - May suffer from optical interference (parameter is cross sensitive)

Table 4-3: Principal thermometric methods used in optical refrigeration experiments, and their relative merits. **(cont'd)**

Interferometry	- Sensitive - Minimal thermal load	- Material dependent - May suffer from optical interference (parameter is cross sensitive) - Sensitive to vibration
Brownian motion	- To be explored*	- Limited to small particles - Environment dependent - Method is not yet mature

* The technology haven't been sufficiently tested in laser cooling experiments.

From Table 4-3 one can select the thermometric method which best adapts to the needs of a particular laser cooling experiment. With exception of the latter, based on Brownian motion, all the methods described in are well-developed techniques. The most used techniques, PTDS and DLT, allow fast analysis of local laser cooling with a simple setup, thus they can also be an option for qualitative measurements. Quantitative measurements can be easily performed with thermocouples. However, due to the particularities faced in laser cooling, such as intense optical fields and the use of new materials, it is reasonable to avoid opaque sensors and techniques which depends on the materials properties. By using a direct method, one can avoid the need to know several parameters of a sample which is still under preliminary analysis. For early explorations in the optical cooling field of research, the methods which are available off-the-shelf are tempting, being able to provide rapid results with little assembly. For long-term research, one may prefer a reliable, quantitative method, which works for any sample. Both characteristics are found in fiber Bragg grating sensors, thus it is expected that in the long run they will be the thermometer-of-choice in solid-state laser refrigeration research.

CHAPTER 5 EXPERIMENTS ON OPTICAL REFRIGERATION

5.1 Design – heat transport and photophysics

5.1.1 Design of the sample holder

Due to the difficulties mentioned in the last section, in order to obtain generally valid results without much concern over the heat transfer processes, the design of a sample holder starts by estimating an upper value for the conductive transfer losses, then minimizing them to a negligible value. In that way, one can consider only the convective and radiative losses, which are both proportional to the surface area of the sample, thus can be calculated together in a single coefficient. A design in which the sample under analysis is supported by thin, low conduction fibers, e.g. single-mode optical fibers, made from fused silica, is considered. The fibers are held by thin steel posts at room temperature, as shown in Figure 5-1.

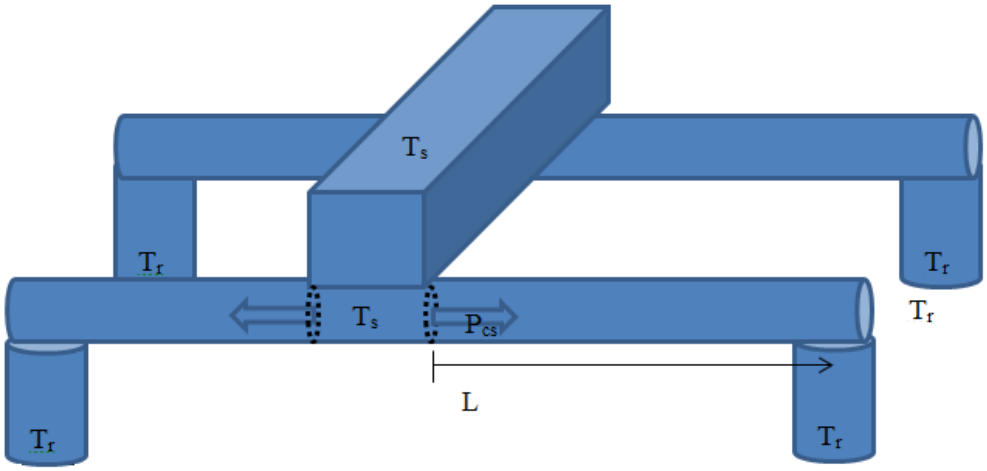

Figure 5-1: Diagram of the sample holder for the heat transfer calculations.

For the configuration above, the fiber section underneath the sample is considered to have the same temperature of the sample T_s, and the fiber section above the metallic post is assumed to have the same temperature of the post T_r. The exposed fiber is assumed to have a temperature distribution respecting Poisson's equation with the appropriate boundary conditions. Each section of fiber, from the sample to a post of the sample holder, and the post itself, can be regarded as a dissipating fin connected to the sample. The heat load from each fin is the sum of the heat flux P_{cs} across the

transversal section, plus the heat load from the section below the sample. The fiber, assumed to have a diameter of 125 μm, also contributes to the effective sample mass and surface, resulting in an additional heat load (Figure 5-2).

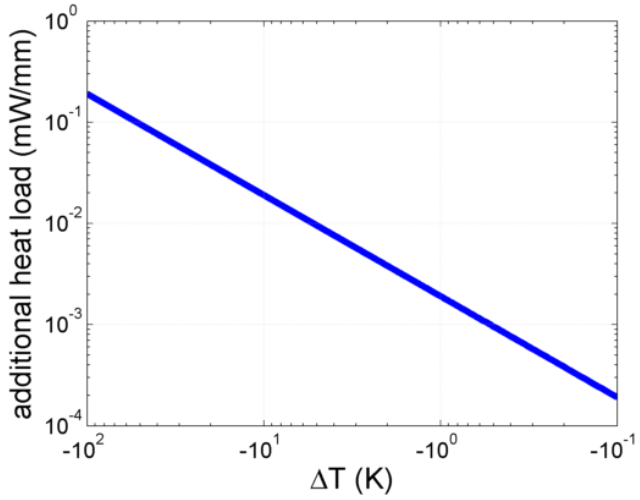

Figure 5-2: Additional heat load on the system as a function of the temperature difference between the sample and environment due to the increase in the total surface area, using a 1-mm-long, 125 μm-diameter fiber under the sample.

It is therefore expected that the sample have an additional heat load of 1.7 μW/K per millimeter of additional fiber (Figure 5-2). One can calculate the effect of the fiber holders and/or a fiber sensor. Considering a 1-mm-edge, 10-mm-long YAG square rod, each contacting fiber corresponds to an additional volume of 0.00123 V_{sample}, an additional exposed area of 0.00207 A_{sample}, an additional thermal capacity of 0.00071 C_{sample}, and an additional time constant of -0.00136 $\tau_{h,\ sample}$. One can notice that the time constant decreases, as expected since the thermal capacity increase ratio is lower than the increase in the surface area.

The values of the total fin load, as a function of the temperature difference between sample and holder, and the fiber length are shown in Figure 5-3.

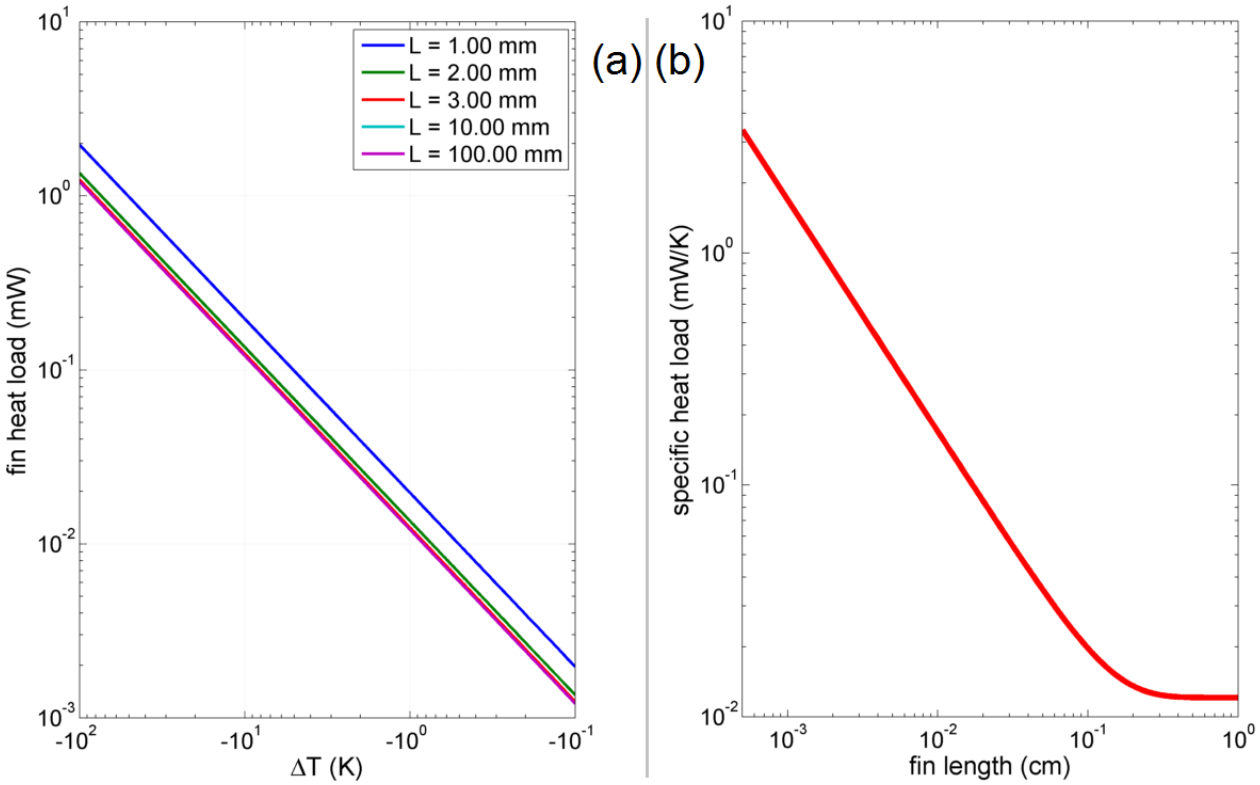

Figure 5-3: Total heat load of the fin to the sample as a function of the temperature difference between the sample and the environment (a), and as a function of the length (b) of the 125 µm-diameter silica fin.

Observing Figure 5-3 one can notice that independent of the total length of the fiber, there is an effective maximum length of the fiber load, which will thus contribute to the effective thermal capacity of the sample. It is shown that the thermal load, by convection, conduction and radiation for a 3 mm-long or more fiber is 0.10 mW for a temperature difference of 8.8 K, or a fin total heat load of 11.4 µW/K per fin, for any fin longer than 3 mm. In our case, the total length of the fiber is 20 mm, so it is within the calculation range. For a 3-fiber contact, the sample holder heat load is $P_{\text{load,holder}}$ = 3 fibers × 2 fins/fiber × 11.4 µW/K·fin^{-1} = 68.4 µW/K**.** Although contact resistance could be a problem in the assumption that the fiber has the same temperature as the sample, the experiments have shown that the air film above the sample – in some cases even for 0.5 mm – has essentially the same temperature as the sample.

5.1.2 Model for the calorimetric experiments

For simplicity, considering a radiatively grey sample at temperature T_s enclosed by a blackbody at temperature T_r, one can find that the sample will exchange heat with the environment at a rate P_{load} given by the equation (5.1) [31].

$$P_{load}(T_s) = A_{surf}\varepsilon\sigma_B\left(T_r^4 - T_s^4\right) + \left(h_{cv}A_{surf} + k\frac{A_{ct}}{L}\right)\left(T_r - T_s\right), \tag{5.1}$$

where A_{surf}, ε, σ_B, h_{cv}, k, L and A_{ct} are surface area of the sample and its thermal emissivity, the Stefan-Boltzmann constant, the convective heat transfer coefficient, solid's link thermal conductivity, length and cross-sectional area, respectively. If the conductive heat transfer is negligible, and for temperature changes small enough so that the blackbody radiative heat transfer is linearly proportional to $\Delta T = T_s - T_r$, Eq. (5.1) can be reduced, without loss of generality, to the form of Eq. (5.2).

$$P_{load}(T_s) = -A_{surf}h_{eff}\Delta T, \tag{5.2}$$

where h_{eff} is an overall heat transfer coefficient, which can be obtained directly from a calorimetric experiment. One can estimate h_{eff} from the heating time constant τ_h – when there is no pump, using (5.3).

$$\tau_h = \frac{C}{h_{eff}A_{surf}}, \tag{5.3}$$

where C and A_{surf} are the heat capacity and surface area of the samples. h_{eff} in this case is related to other heat transfer parameters of the sample-environment by

$$h_{eff} = h_{cv} + \sigma_B\varepsilon 4T_r^3. \tag{5.4}$$

For large temperature drops, the error introduced by the linearization of the Stefan-Boltzmann law is not negligible, and depends on the emissivity of the sample. As an example, the heat load range for a laser cooling experiment is calculated using a 10 mm-long sample of square cross section 2 × 2 mm^2, and h_{eff} = 20 W·m^{-2}·K^{-1}, and the results are shown in Figure 5-4.

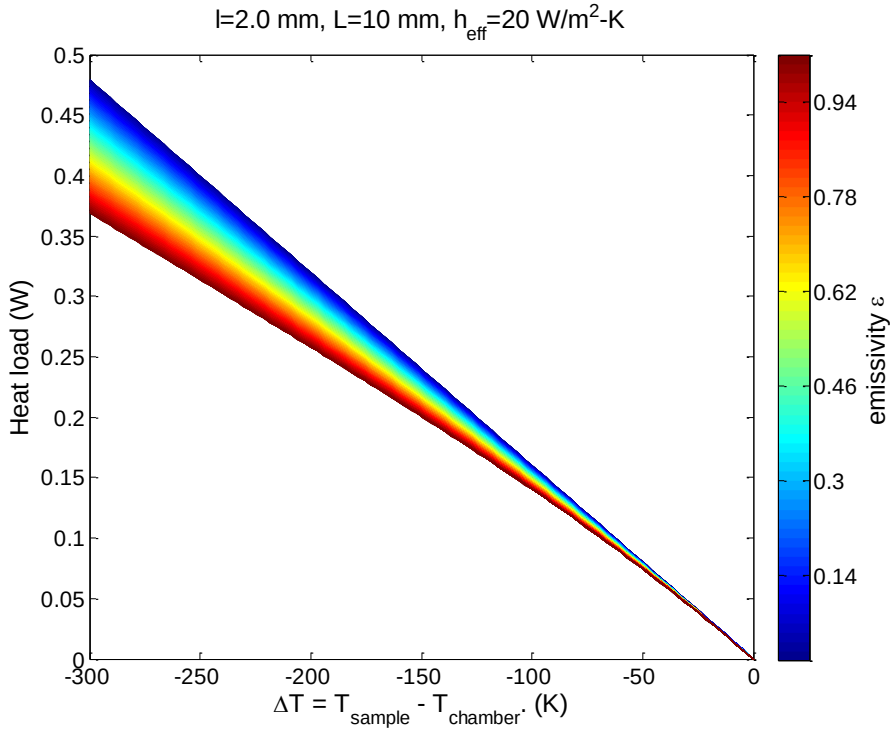

Figure 5-4: Total heat load dependence on the temperature drop from 300 K. These are calculated based on the experimental value of h_{eff}, but considering the error due to the linearization of the Stefan-Boltzmann law. This consideration leads to the broadening at large temperature differences, depending on the value of the emissivity.

While for temperature drops in the order of 10 K the error is < 1%, it starts being significant for lower temperatures, adding up to 10 % for a 100 K temperature drop. The use of an effective heat load is not only convenient, but it is a good choice. For convenience, a commonly used value for h_{cv} in simulation is 10 $W \cdot m^{-2} \cdot K^{-1}$ [117], i.e. almost half of h_{eff}, a relation also found in [123, 195]. Since the value of h_{cv} is strongly dependent on the sample and chamber surfaces, geometries and orientation as well as the air velocities [196, 197], it can range from 5 $W \cdot m^{-2} \cdot K^{-1}$ to 25 $W \cdot m^{-2} \cdot K^{-1}$ and the most accurate thing to do is to measure it, coupled to ε, as it is done in the present work.

In a laser cooling/heating experiment, the steady-state temperature T_∞ of the sample will be achieved when the cooling/heating power equals the heat load imposed by the environment, i.e. $P_{load}(T_\infty) = P_{cool}(T_\infty)$, which leads to:

$$-A_{\text{surf}}\,h_{\text{eff}}\,\Delta T = P_{\text{abs}}(\lambda_p)\eta_{\text{cool}}(\lambda_p) = P_{\text{p}}(\lambda_p)A_{\text{L}}(\lambda_p)\eta_{\text{cool}}(\lambda_p)$$
$$\Rightarrow \frac{\Delta T_{\infty}(\lambda_{\text{p}})}{P_{\text{p}}(\lambda_{\text{p}})} = -\frac{1}{A_{\text{surf}}\,h_{\text{eff}}}A_{\text{L}}(\lambda_{\text{p}})\eta_{\text{cool}}(\lambda_{\text{p}}) = \frac{1}{\kappa_{\text{th}}}A_{\text{L}}(\lambda_{\text{p}})\eta_{\text{cool}}(\lambda_{\text{p}}), \tag{5.5}$$

which is the same as Eq. (2.6). Thus the sample-environment thermal coupling coefficient is indentified as $\kappa_{\text{th}} = -A_{\text{surf}}h_{\text{eff}}$.

5.2 Cooling of Yb:YAG at normal conditions of temperature and pressure

The sample used in the experiments described here is a commercially available ultra-high purity, 3 at.% Yb^{3+}:YAG crystal, purchased from Scientific Materials Corp. The crystal is 10 mm long, with Brewster-cut square cross-section of 1 mm edges. The absorption spectrum (Figure 5-5a) was measured using a Perkin-Elmer Lambda 19 spectrophotometer in the range 400 - 2500 nm. The fluorescence spectrum under a pump wavelength of 940 nm was measured perpendicularly with a 65 μm core diameter silica fiber connected to an Ando AQ6317B optical spectrum analyser and it is shown in the Figure 5-5b.

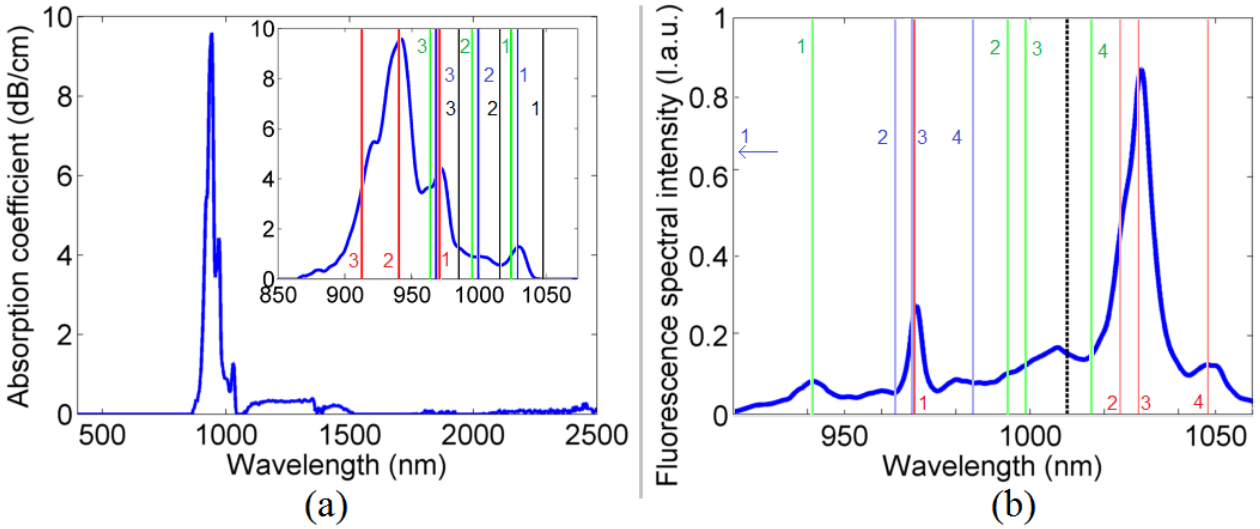

Figure 5-5: Absorption (a) and emission (b) spectra of the Yb:YAG crystal. The inset in (a) is a zoomed-in detail of the most important wavelength region 850 nm to 1060 nm. (b) shows the normalized fluorescence spectral density, and the vertical black dashed line shows the calculated mean fluorescence wavelength. The continuous vertical lines in (a) represent the position of the absorption transitions $(1, p) \rightarrow (2, q)$, with p = 1 (red), 2 (green), 3 (blue) and 4 (black) and q = 1, 2 and 3 as labelled in the graph. The continuous vertical lines in (b) represent the position of the emission transitions $(2, q) \rightarrow (1, p)$, with q = 1 (red), 2 (green) and 3 (blue), and p = 1, 2, 3 and 4 as labelled in the graph.

From the fluorescence spectrum one can obtain λ_F = 1010(1) nm, which is in line with the value λ_F ~ 1009 nm from the theoretical prediction [114], with our calculations using data from Ref. [125], and other works [20, 123, 124]. Another publication reported λ_F = 995 nm [122], using a crystal from the same company. However one should not expect a red shift of more than 2 nm in the external fluorescence of our 1 mm thick sample in comparison with its internal mean fluorescence wavelength; hence our measurement is consistent with the theoretical prediction.

5.2.1 Calorimetry, part I: Cooling spectroscopy and thermal parameters

For laser cooling experiments, the sample was supported by a sample holder consisting of four 1 cm long, 125 μm diameter silica fibers, held by eight steel posts of 1 mm diameter, attached to an aluminum plate. The holder was placed inside a matt black-painted aluminum chamber with 2 silica windows for pumping. A thermocouple TC is used to measure the chamber temperature. The

temperature difference ΔT is given by the temperature measured by the TC subtracted by the temperature of the chamber. The complete experimental setup is depicted in the Figure 5-6.

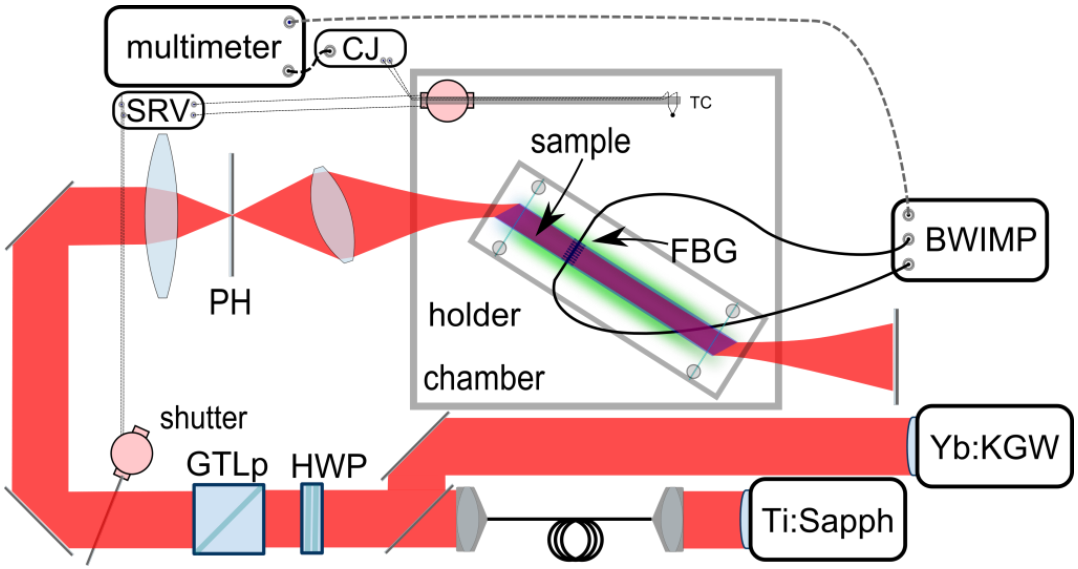

Figure 5-6: Experimental setup used to measure LICOS. Both a Yb:KGW laser and a CW Ti:Sapphire laser is used to pump the sample. The Ti:Sapphire output is directed to the cooling setup through an optical fiber. The pump power is reduced by rotating a half-wave plate (HWP) placed before a Glan-Thompson prism (GLTp). The beam is filtered by a pin-hole (PH) at the focus of a Keplerian telescope used to condition the beam to the desired diameter. A servo-motor controller (SRV) is used to drive the thermocouple (TC) and a shutter. An electronic cold junction compensator (CJ) provides a reference for the TC.

The Bragg wavelength temperature sensitivity was measured to be 9.9 pm/K. With a Bragg reflection bandwidth of 616 pm, the total measurement range is 62 K. This can be increased if the probe laser is tuned continuously as the Bragg wavelength shifts, or by the use of a broadband source, as used in the calibration procedure.

The output of a remote CW Ti:Sapphire laser is coupled to a single mode, HI 1060 Flex fiber, and its collimated output focused into the sample (Figure 5-8a). The steady-state temperature is recorded, as the Ti:Sapphire laser wavelength was manually tuned using a tuning micrometer. The wavelength of maximum temperature drop was measured to be 1030 nm, as also found in Ref. [122] for a similar sample. The estimated, measured and previously reported cooling figure-of-merit are shown in Figure 5-7. In this part of the experiment, the pump power was not measured at

the sample, and the values from the literature do not explicitly refer to the cooling power, thus the values are normalized to be shown in the same scale.

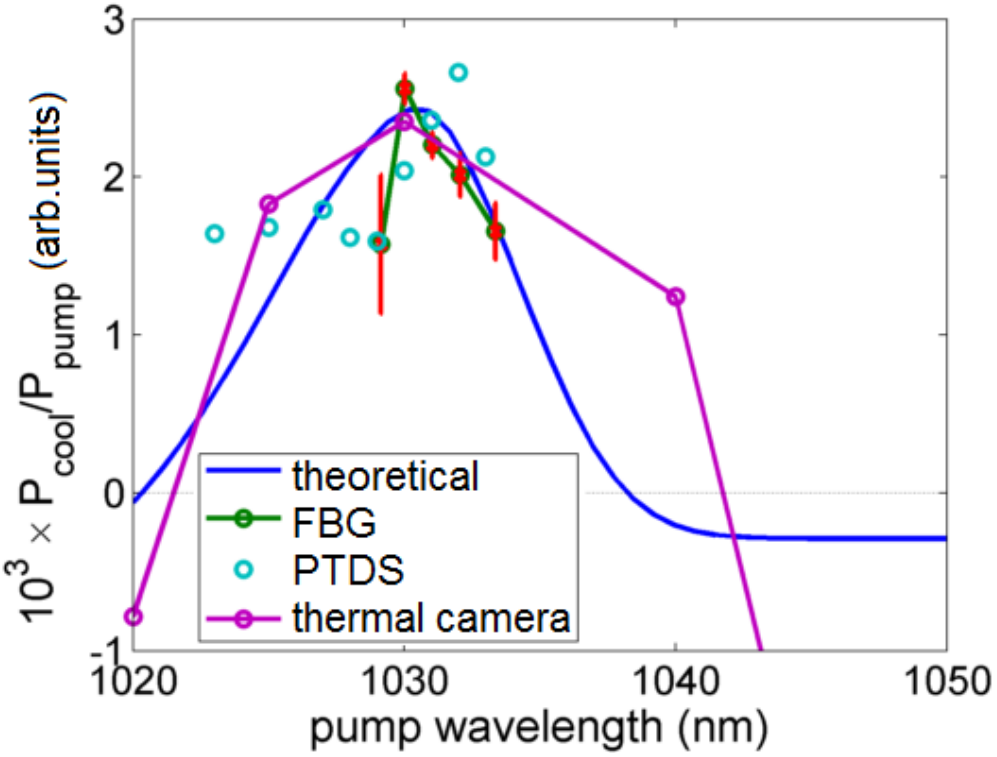

Figure 5-7: Cooling figures of merit as a function of the pump wavelength, estimated by different methods. The expected cooling figures-of-merit from absorption and emission spectra are shown in the blue curve, and the normalized values measured by a FBG (green) in this work, as well as photothermal deflection spectroscopy (cyan) and thermal camera (purple) results from [122] are also shown.

In order to measure thermal parameters such as the thermal time constant and the effective heat transfer coefficient, as well as to assess the system's sensitivity, the sample was pumped at different power levels (Figure 5-8b and Figure 5-8c) at the optimal pump wavelength of 1030 nm using the Ti:Sapphire laser. In Figure 5-8b one can observe a temperature transient at the relatively low pump power of 17 mW, with a resolution of ~ 10 mK, which corresponds to a Bragg wavelength measurement of 0.1 pm. The principal limitation comes from the probe wavelength stability, nominally 5 pm/h. By measuring both the reflected and transmitted powers from the FBG, one can compensate for probe power variation.

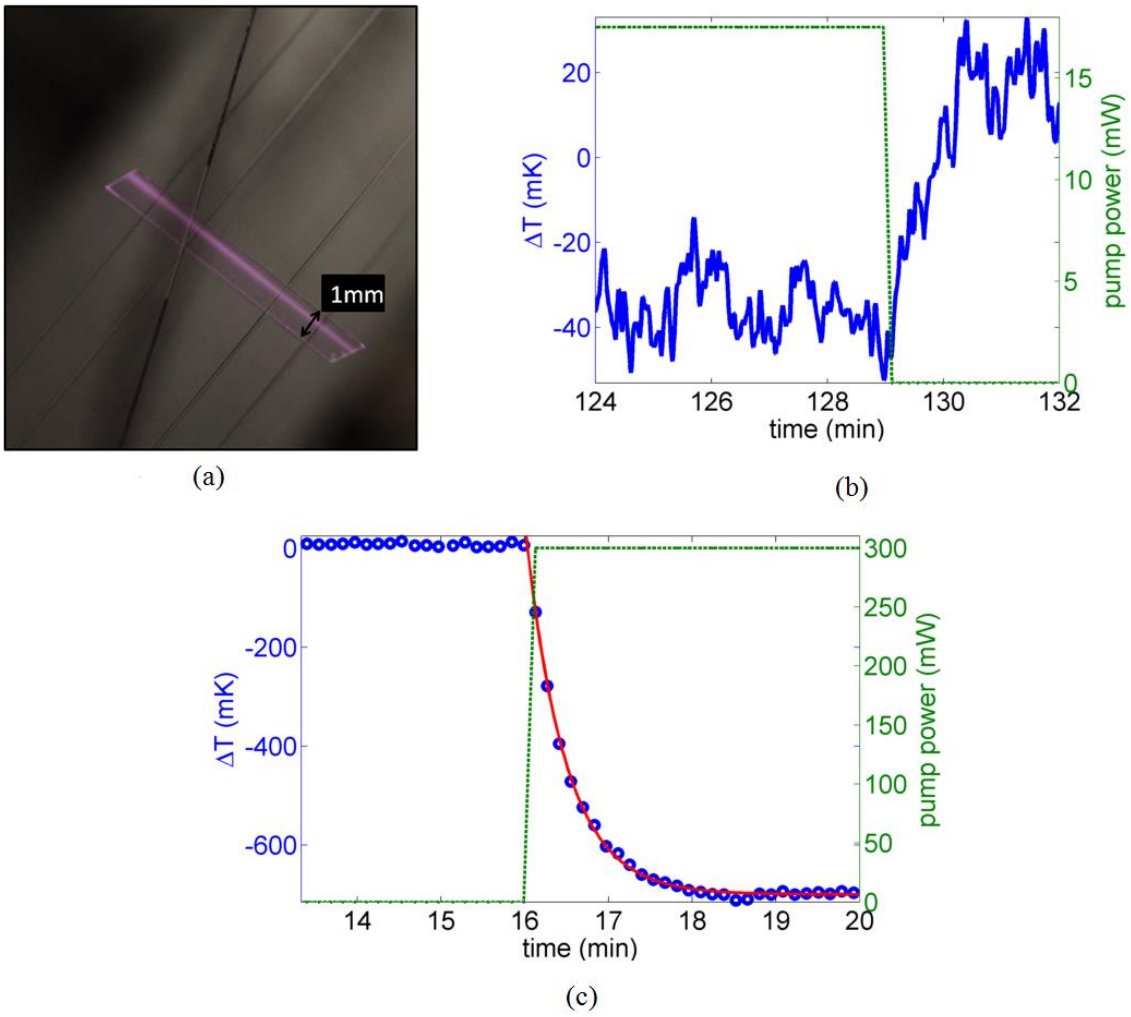

Figure 5-8: Cooling of a 1 mm square cross section Yb:YAG crystal. (a) Sample being pumped. (b) Temperature dynamics as a function of time, as the laser is switched on and off, at the pump power of 17 mW. (c) Temperature dynamics as a function of time, as the laser is switched on and off, at the pump power of 300 mW. Also shows a fitted exponential decay curve (continuous line). The dotted line in (b) and (c) is pump power.

From the fitting shown in Figure 5-8c, the thermal coupling time constant was calculated to be τ_h = 29.4(1) s. The thermal parameters of the sample are summarized in Table 5-1.

Table 5-1: Thermal parameters of the sample

Parameter	value	units
Mass density ρ	4550 [198]	$kg.m^{-3}$
Volume V	1.0×10^{-8}	m^3
Specific heat c_h	590 [198]	$J.kg^{-1}.K^{-1}$
Thermal capacity C_h	26.8×10^{-3}	$J.K^{-1}$
Surface area A_{surf}	4.2×10^{-5}	m^2
Thermal coupling time constant τ_h	29.4	s

A lumped-capacitance model for the thermal behaviour of the sample estimates $h_{eff} = C_h/(\tau_h A_{surf}) = 22\ W.m^{-2}.K^{-1}$, where C_h is the heat capacity of the sample. The use of a constant value of h_{eff}, ignoring the nonlinear behavior of the radiative heat transfer, can lead to an acceptable error of 1% in the estimation of the heat load, for a large range of convective heat transfer coefficients and emissivities from 0 to 1. For convenience, a commonly used value for h_{cv} in simulation is $10\ W.m^{-2}.K^{-1}$ [117], i.e. almost half of our value for h_{eff}, a relation also found in Refs. [123, 195]. Since the value of h_{cv} is strongly dependent on the sample and chamber surfaces, geometries and orientation as well as the air velocities [196, 197], it can range from $5\ W.m^{-2}.K^{-1}$ to $25\ W.m^{-2}.K^{-1}$ and the most accurate thing to do is to measure it, coupled to ε, as it is done in this Thesis. However this error can be up to 10 % for a temperature drop of 100 K.

5.2.2 Calorimetry, part II: Background absorption

One key requirement in materials for laser cooling is a very small background absorption α_b. Usually its value is inferred from the fitting of the cooling efficiency as a function of the pump wavelength, or from the zero-crossing wavelengths, where the sample neither cools nor warms. Here, α_b is measured directly, using the calorimetric method with a FBG, and an off-band pump laser. Since the wavelength 1550.1 nm is far from the resonant absorption band, this wavelength was chosen to pump the sample for the measurement of background absorption. Since 1550 nm is near the absorption band of trivalent erbium, and it may be a contaminant present in Yb:YAG, a narrow linewidth laser of < 90 pm bandwidth is used. At 1550 nm, the room-temperature absorption cross section of Er^{3+}:YAG was measured at the same level as the noise floor in a 10 nm-wide

window [199-202], so the pump used here is safely out-of-band. The same setup as shown in Figure 5-6 was used for this measurement, but with an IPG ELR-70-1550-LP 1550nm ytterbium-erbium fiber laser as the source of optical power. When using an input power of 2170 mW an equilibrium temperature difference of 688 mK was observed (Figure 5-9).

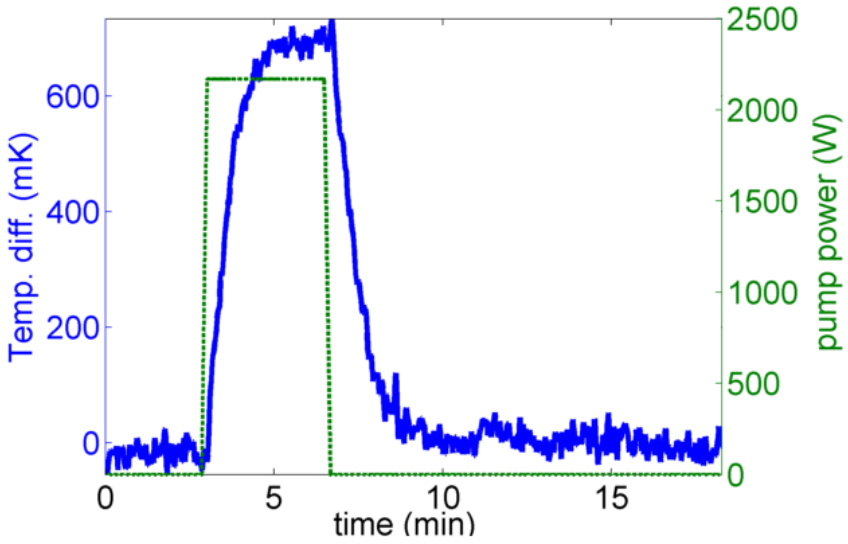

Figure 5-9: Sample's temperature dynamics under out-of-band 1550 nm pumping, as measured by the FBG, discounted the rise on the chamber temperature, measured by the TC. Dotted curve: pump power.

From Eqs. (2.6) and (5.3), with $\kappa_{th} = -A_{surf}h_{eff}$, and the parameters shown in Table 5-1, $P_{heat} = \alpha_b L_s P_p$ = 627 μW, and the background absorption coefficient of α_b = 627 μW/(L_s × 2170 mW) = 2.89 x 10^{-4} cm^{-1} is calculated. This is within the interval for the reported optically cooled materials. For instance Epstein [122], reported an α_b = 2.2 x 10^{-4} cm^{-1} in a 2.3%Yb:YAG crystal from the same supplier. This difference indicates that the impurities responsible for the sample heating scale with the dopant concentration C_{YbIII}, and that the value of the α_b/C_{YbIII} measured here differ by only 0.7% with the result found in [122], although measured in a completely different and direct fashion.

5.2.3 Optimization of the pump power and sample dimensions

5.2.3.1 Experiment with high pump power

In order to observe the maximum temperature drop under the high thermal load from the environment, the crystal was pumped with 4.2 W from a commercial Yb:KGW laser. The laser

emits 10 ps pulses at 1029 nm at a repetition rate of 600 kHz, which can be regarded as effectively continuous wave for this experiment. This pump laser is not tunable so it was not operating at the optimal pumping wavelength for cooling. The Gaussian beam diameter at the sample is $2w_0 \sim 0.67$ mm. In the single pass configuration the chamber heated by 1.68 K (Figure 5-10a) from which a temperature drop of 8.8 K of the crystal is achieved (Figure 5-10b), for 1.0(1) W of absorbed power.

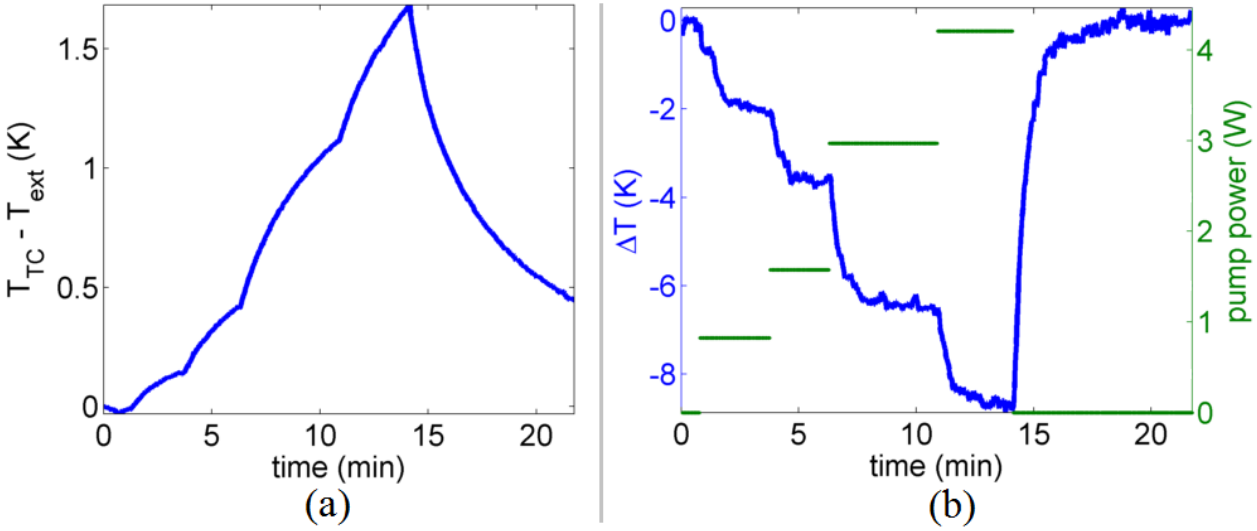

Figure 5-10 Temperature dynamics as the laser pump power is increased from 0 W up to 4.2 W. (a) The chamber temperature variation, measured by the thermocouple. (b) The difference between the temperature of the Yb:YAG crystal measured by the FBG and the chamber temperature. Before 0 s the crystal was shortly pumped for test purposes, which explains the finite temperature difference at 0 s, but which stabilized after ~1 min.

Using the thermal parameters from Table 5-1 and the observed temperature drop of 8.8 K in Eq. (5.5), one can calculate that the value of the cooling power, and heat load by the environment in the steady-state case is 8.0 mW. The last key parameter in LICOS to be calculated, η_e can be finally obtained from the measurements presented so far, and from the value σ_e (1029 nm) = 2.0×10^{-20} cm^2 [203]. With Eq. (2.1) one can obtain $\eta_e = 0.9914$ which is close to within 1% to typical values obtained in the literature [122]. The temperature drop of 8.8 K is also close to the 8.9 K obtained in vacuum [122]. The increased heat transfer factors from the environment used here are compensated for by choice of more optimal geometries. The Gaussian beam diameter at the sample is $2w_0 \sim 0.67$ mm, filling it completely and reducing absorption saturation effects. Also a small cross section sample reduces the total heat load, thus allowing a larger temperature drop. However

the sample cannot be decreased indefinitely since it poses experimental difficulties for manipulating it, and more importantly, can limit the power which can be used without detrimental saturation effects.

5.2.3.2 Simulations with further optimization

In this section, $P_{cool}(T_s,P_{pump}) = P_{load}(T_s)$ is solved for T_s, as a function of the sample edge d, the external quantum efficiency and the pump power (Figure 5-11a). If one allows 1% loss of the pump power due to truncation, the pump beam radius should be $w_0 = 0.67d/2$, a relation that will be implicit in the discussion below. This also keeps the active area of the sample overfilled in order to reduce saturation. The experimental values used are, σ_a(1029 nm, 300 K) = 6.8×10^{-22} cm^2 and λ_f (1029 nm, 300 K) = 1010 nm from this work, σ_e(1029 nm, 300 K) = 2.0×10^{-20} cm^2 from Ref. [203]. The temperature dependence was estimated with the relation $\sigma_a(T) = \sigma_a(300\text{ K})[1 + 0.005\Delta T\text{ K}^{-1}]$, from the data in Ref. [122]. $\sigma_e(\lambda_p, T) = k\sigma_{eRC}(\lambda_p, T)$, where $\sigma_{eRC}(\lambda_p, T) = \sigma_a(\lambda_p, T)Z_u\exp[hc(1/\lambda_{ZL} - 1/\lambda_p)/(k_BT)]$ is the McCumber formula [204], and the correction factor for the McCumber relation $k = \sigma_e(300\text{ K})/\sigma_{eRC}(300\text{ K})$. λ_{ZL} = 964.7 nm, and Z_u = 1.13 [205]. The cross sections calculated this way shows a similar dependence with the temperature as the dependence shown in Ref. [206], which was calculated at 1030 nm using the dataset from Ref. [207].

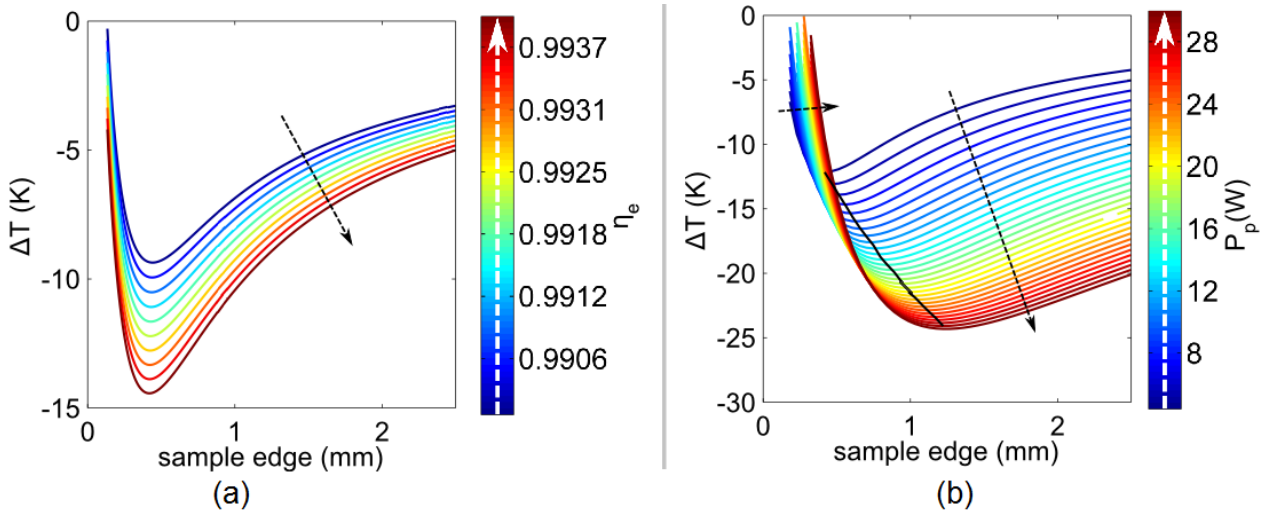

Figure 5-11: Calculated steady-state temperature of Yb:YAG in air as a function of the sample edge dimension d. (a) For different EQEs, when pumped with 4.2 W at 1029 nm. (b) For a EQE = 0.9914, for different pump powers. Solid line: the optimal d for the corresponding pump power. Dashed arrows indicate the direction of the curve ordering in respect to the parameter in the colorbar.

The solution of $P_{cool}(T_s,P_{pump}) = P_{load}(T_s)$ for several d allows the determination of the size at which one should observe the maximum temperature drop for a given pump power. An optimized sample with d = 0.43 mm will cool by ΔT = -12.1 K for the available pump power of 4.2W. Our sample dimensions would require a pump power of 20.8 W to achieve its maximum temperature drop of ΔT = -21.3 K. However with more power available the temperature of the present sample could be further reduced to $\Delta T(d$ = 1.0mm, 30W) = -23.8 K, for 30 W of power. Surprisingly a larger sample could experience a larger drop in the temperature, for a sample of d = 1.2 mm one could observe $\Delta T(d$ = 1.2mm, 30W) = -24.3 K. If the pump power is increased, one would observe a larger temperature drop, until certain power values, above which the efficiency decreases and can cross the cooling/heating region, as shown in Figure 5-12 for the 1-mm sample.

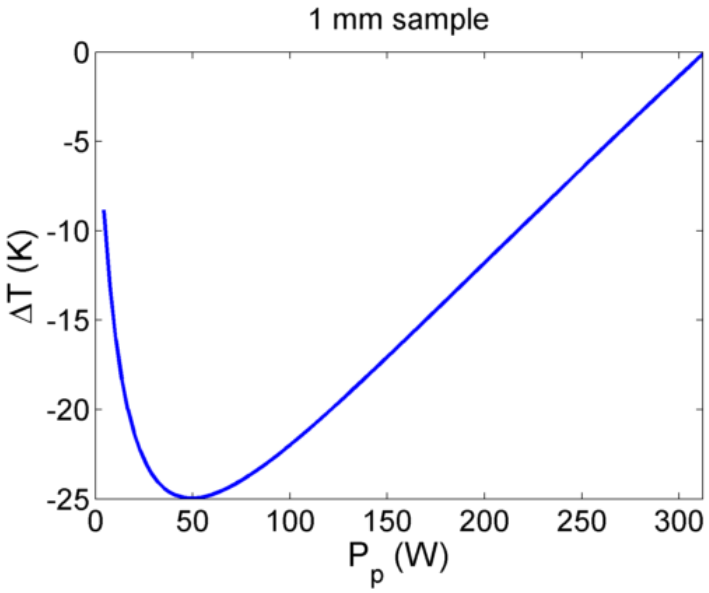

Figure 5-12: Calculated steady-state temperature of a 3% Yb:YAG of 1-mm square cross section in air as a function of the pump power.

The maximum temperature drop, limited by saturation for the 1-mm sample is -25 K, for a pump power of 50 W, as shown in Figure 5-12, for a fixed sample edge. This temperature drop is larger than the -23 K at the optimal/matched power of 20.8 W, but it is evident that the process is much less efficient. Further increase in the pump power is detrimental for cooling, up to a point where there is no cooling at all.

That result is clear evidence of how saturation effects can play a role in optical refrigeration. As can be seen from Figure 5-11, the minimum achievable temperature of a sample is more affected by saturation, when *d* decreases from the optimal value, than by the increase in the sample mass when *d* increases from its optimal value.

The main physical quantities for laser refrigeration were obtained with the use of an FBG, and they are in line with the values reported in the literature. Pumping our sample in a single pass scheme with 1.0 W of absorbed power, a temperature drop of 8.8 K was achieved, although the sample was coupled radiatively to the chamber walls and maintained in air. As a comparison, previous reports could observe a temperature drop of 8.9 K in vacuum, for a 1.8 W of absorbed power [122]. The difference can be explained by the fact that our sample is closer to having the optimum dimensions than the sample used in previous reports, although this data is not available. The theoretical model and the simulations using experimentally derived data fit our experimental results reasonably well.

5.2.4 Further tests - cooling of a large load

The ultimate goal of a conventional refrigerator is to cool an external heat load. This is the main threshold which LICOS separates from other optical cooling technology: in LICOS the fluorescence from the excited ions takes away heat from the solid matrix, not from the ions themselves. As external loads, one can thus consider the laser-cooled solid itself, the diffusion-cooled solid as a whole, the sensor used as a temperature probe [58], the supporting structures [56], or the surroundings gray walls or air [34], and ultimately an additional solid load to be refrigerated. The refrigeration of an external payload could bring optical cooling to the niche of indirect refrigeration of microelectronic components, before one can optical-cool a semiconductor itself. In the short term, one can use optical cooling to refrigerate earth-based components such as ultrastable laser cavities, or space-bourne instruments such as detector arrays. In the long term, optical cooling may follow the same path as did thermocouples, from a sensing technique to a ubiquitous cooling system which can be taken to a park to refrigerate beer.

Here the proof-of-concept of a laser-cooled crystal being used to refrigerate a passive solid thermal mass is shown. To a certain extent, optical-cooling of a semiconductor was demonstrated, for a GaAs disk of 5 μg used as a temperature sensor [58], and recently for nm-thick belts of CdS [56], cooling also the edge of the silicon-on-insulator supporting structure. However, no external mass

larger than a few μg has been optically-cooled to date. In this section, initial tests with larger masses are reported.

The initial plan in the present Thesis was to cool a semiconductor laser. The main constrain of doing so, as it is with opaque samples, is that one has to design a thermal link which rejects fluorescence but allows thermal conduction to occur. Extensive works have been performed on the design of such thermal links [208], and the most recent include use of high purity materials, and state-of-art shaping and bonding [209, 210]. A more straightforward way would be to deposit a high quality mirror on the surface which separates the cooler and the load. It can be shown that the load and the cooler will certainly warm up if the mirror leakage and absorption coefficient are larger than $0.31/A_{surf}$ mm^2, where A_{surf} is the contact area, considering a cooler operating with 1.1 W optical absorbed power and 8 mW of cooling power. Since a spare sample was not available to make such invasive tests, a more conservative test was done, using a transparent heat load to avoid the problem of fluorescence reabsorption without the need to modify the optically-cooled sample.

The transparent load is a silica slab cut from a microscope plate, roughly polished, of edges sizes 1.25 × 0.96 × 2.42 mm^3, denominated LT1. This corresponds to a volume of 2.9 mm^3, or a mass of 6.4 mg, considering the volumetric mass density of silica of 2200 kg/m^3. The laser-cooled mass S1 is a Yb:YAG crystal of 1 mm^2 cross sectional area and 10 mm length, and it has a mass of 45.5 mg. The thermal capacity of S1 and LT1 are respectively 26.8 mJ/K and 4.5 mJ/K, which implies that C_L/C_S ~ 16.8%. LT1 was placed at the center top of the S1, and the FBG was placed above LT1, thus measuring the load surface temperature, as shown in the Figure 5-13.

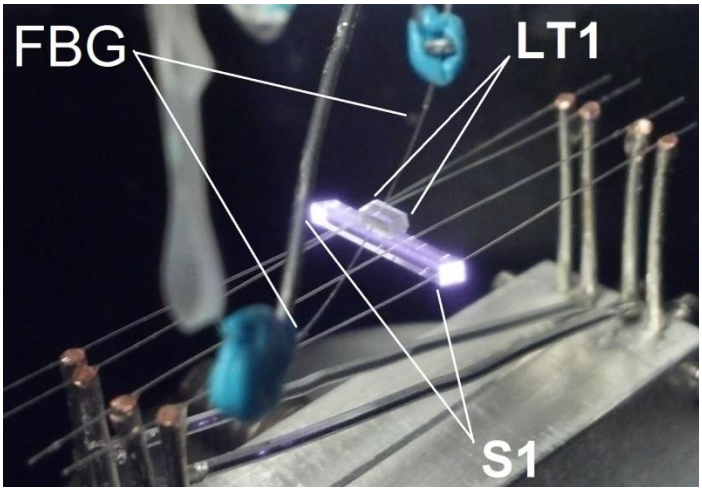

Figure 5-13: Arrangement of the optical cooler and load for the demonstration of the cooling of a transparent solid thermal load. The cooler S1 is held by 4 optical fibers, and the load LT1 is placed on the top of S1, and the FBG measures the temperature of LT1 while S1 is pumped.

After pumping S1 with roughly 190 mW of laser power at 1030 nm wavelength, a final temperature drop of 150 mK is observed. Although small, the cooling is clear and shows that one can indeed use laser-cooling to refrigerate a passive material. At this scale, one may ask if it is possible to use it to switch or control the temperature of small devices, and how fast it could be. Surprisingly, the time constant of the composite system of larger thermal mass was measured to be 26.8(5) s, which is smaller than the one measured by the unloaded sample. This is due to the fact that the external area was increased by a larger factor than the thermal capacity increase. By the addition of the load, the effective surface area of the cooler is increased by $2 \times 0.96 \times (2.42 + 1.25)$ mm^2 = 7.05 mm^2, from an initial surface area of 42 mm^2 (S1's area), so the total area is $A_{S1} + A_{LT1}$ = 49.1 mm^2. This leads to a thermal equilibrium constant of 29.4 s, approximately the same as the unloaded sample. The small discrepancy probably comes from the fact that the emissivity of the silica load is around 0.8-0.9, while the emissivity of YAG is around 0.32 [211]. Although the thermal time constant in the present experiments is relatively long, it can be reduced even for increasing thermal mass, as it was shown here. In the case of an embedded system in a chip, for example, the time constant can be shorter still. The question that was still open was if one could cool a load of larger thermal mass. As it is described in the next paragraph, a larger mass can be cooled by as much as the small mass.

Similar experiments as described in the last paragraph were performed, this time using S1 as the load, and a 2-mm cross-section Yb:YAG (S2) as the refrigerator. S2 is pumped with approximately 200 mW of power at a wavelength 1030 nm, and recorded the temperature of S1 using a FBG, as the pump is switched on and off (Figure 5-14). Since S2 is larger than S1, it is easier to recirculate the unabsorbed power back to the sample using a concave mirror. In order to compare with the single-pass case, measurements, both with the mirror blocked and unblocked were performed.

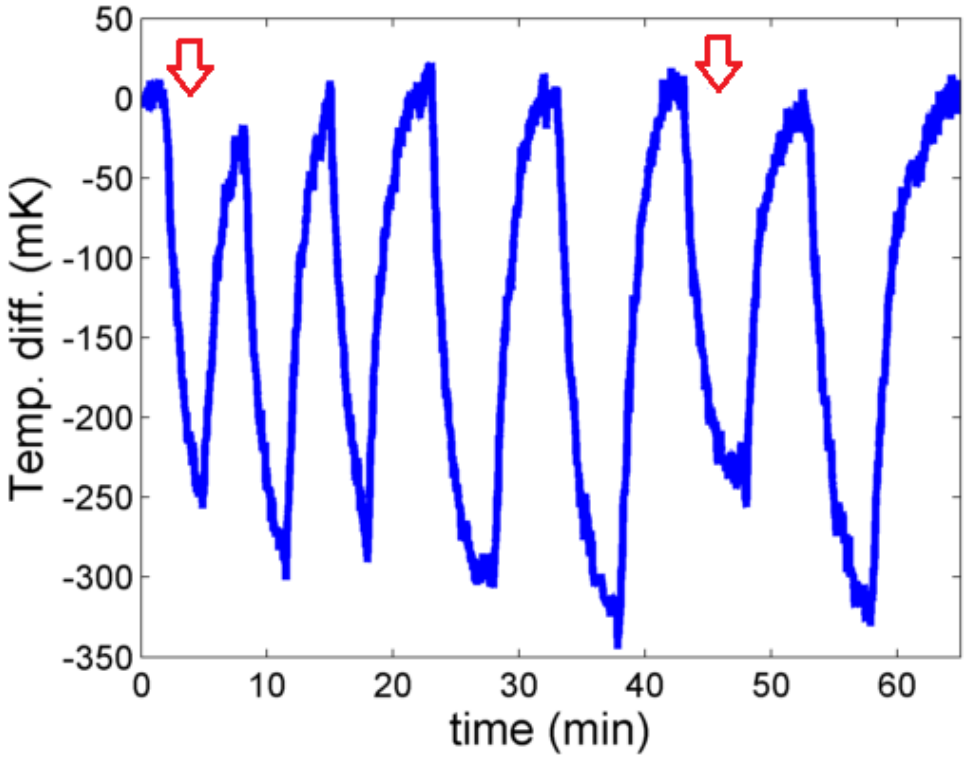

Figure 5-14: Temperature dynamics of a load conductively-coupled to an optically-cooled sample, under different pumping conditions. The decreasing signal corresponds to when the sample is being pumped, and the red arrows indicates the two parts where the beam makes a single pass though the sample.

A temperature drop of 270(20) mK can be observed from the data shown in Figure 5-14 when the sample is pumped by a single-passing beam, and 300(20) mK when the transmitted beam is recirculated in the sample once, showing that unabsorbed power can be recycled and contributes to a higher cooling power. Here, with an additional external mass of 45.5 mg, much higher than the 6.4 mg of the experiment using a silica rod, a larger temperature drop for the same pump power

is observed. This highlights two features of the experiment: reabsorption by high-quantum efficiency materials has less negative effects than impurities; and that extreme rejection of the fluorescence must be achieved in order to cool an absorbing or opaque sample. As it can be concluded from the two latter experiments, even a weakly absorbing sample such as a microscope slide has enough absorption to mitigate the cooling, to a point that it cools less than a sample of much larger mass.

In this chapter, optical cooling of solids to refrigerate a macroscopic device, in air at atmospheric pressure, has been demonstrated using a contact sensor for the measurement of the absolute temperature of the cooled sample. Several groups have also put significant effort on pushing the boundaries of solid-state optical refrigeration, and important breakthroughs are seen year after year in this field of research, as detailed in the introduction. A last avenue which is relatively underexplored, but which prevents LICOS from achieving its full potential, is the research of innovative optically-cooled materials which can be mass-produced. So far, all the work in laser cooling has concentrated on samples which are hard to fabricate, to handle and to integrate in a broad range of devices. The next Chapter of the thesis will concentrate on the search for new optical cooling candidates which could potentially fill this significant shortfall.

CHAPTER 6 FURTHER INVESTIGATIONS

6.1 Optical cooling of nanocrystalline powders

Cooling of single nanocrystals was first proposed in 2015 [79], in an optical trapping setup. Usually in optical trapping one ends with unwanted heating of the sample; optical refrigeration could serve as a tool for controlling this heating. It is possible to estimate the temperature of a particle, as described in the section 4.1.1, by measuring its Brownian motion using a laser and a quadrant photodiode. If instead of warming, the nanoparticle were to cool below the temperature of the surroundings, one would have the cold-Brownian motion, which has potential applications in fundamental research, and so far was not realized in dense media [212]. It can be envisaged that by choosing the right wavelength, one can obtain a "radiation-balanced-heat" nanomarker, which would not suffer from self-heating, thus simplifying temperature measurements which use fluorescence intensity ratio (FIR), as well as avoiding the use of hot-Brownian motion (Ref. [213]) analysis in particle tracking and temperature estimation.

Optical cooling of single nanoparticles in water can be challenging. While a dielectric nanoparticle does not heat as much as other particles used in nanothermo heating, solvent absorption itself can be an issue. For instance, the absorption coefficient of water in the wavelength range 900 nm to 1200 nm is of the order of 10^{-1} cm^{-1} to 1 cm^{-1} [214], while one expects laser-cooled materials to have a maximum background absorption in the order of 10^{-3} cm^{-1}, thus water is far from an ideal candidate for use as a surrounding material in laser cooling. Alternatively one could use deuterium oxide, since the absorption is shifted towards longer wavelengths compared to water and its absorption is therefore reduced in this wavelength region, by a factor of at least ~ 50 [215, 216]. There are many issues to be solved for cooling of trapped nanoparticles in water, and this research is just beginning. The investigations in this chapter concentrate on the cooling of nanocrystalline powders, since its analytical methods are closer to those used in bulk cooling analysis, but some of the results can also be used for cooling of single nanocrystals.

Optical refrigeration with nanocrystalline powders was proposed in Ref. [217] and it was experimentally achieved through infrared-to-visible upconversion, in an neodymium-doped KPb_2Cl_5 nanocrystalline powder [80, 81]. The optical cooling of nanocrystalline powders can increase considerably the range of possible optically-cooled devices, for example by mixing the

powder in a fluid or embedding it in a polymer or glass matrix for microfluidics, localized cooling or making of devices of arbitrary shape. Embedding nanocrystals in glass is an alternative scheme for producing high-quality glass-ceramics for optical cooling. The use of nanocrystals also allows one to explore new phenomena that have not yet been obtained in bulk materials for cooling. For instance, the random scattering of photons in the powder can lead to photon localization, allowing one to achieve high intensities without the use of a high power pump source or a cavity. The small size of the crystals and the high surface-to-volume ratio can lead to higher absorption in the long-wavelength tail of the spectra, when compared with the bulk counterpart. This would allow the use of a pump at longer wavelengths, thus providing a higher cooling efficiency than the one observed in the bulk. In this chapter the spectroscopic properties of ytterbium-doped nanocrystalline powders for optical refrigeration are investigated. The preliminary results indicate that in the present conditions, no significant distortion or enhancement of the absorption spectra occurs. More studies are necessary to obtain nanocrystals with high enough quantum efficiency to show optical cooling. It is yet to be determined if the source of the small quantum efficiency is due to metallic and rare-earth impurities, trapping or water or other adsorption of contaminants on the powder's large surface.

6.1.1 Preparation of the samples

Samples at three different concentrations, (10, 15 and 20) mol % Yb:YLF were prepared by our collaborators at INRS and were sent to our lab. For the first measurements, the samples were dispersed in water inside a 1-mm-long cuvette by vigorous shaking and immersion in a sonicator for 5 min, then immediately transferred to a Perkin-Elmer 1050 spectrometer in order to measure the transmission spectra. When compared to the transmission spectra of pure deonized water, no significant difference was observed, due to the small concentration of nanocrystals. Also, the crystals are found to precipitate relatively fast, thus compromising the accuracy of the measurement. Therefore it is better to work with the dry form of the powders so that one can ensure reproducibility.

Yb:YLF nanopowders were dried by drop-casting onto the top of microscope slides and left to dry in a room-temperature chamber with dry air. The resulting dispersed dry powder was accumulated into a single ~ 3mm-diameter spot, in order to increase the emitting centers in the optical probe volume.

6.1.2 Absorption spectra

Although reproducible, it is relatively hard to measure the probed thickness of the powder, thus the absorption measurement is only relative. The microscope slides with dry powders were placed in a Perkin-Elmer 1050 spectrometer to measure the transmission spectra. After a baseline subtraction to correct for scatter and Fresnel reflection from the microscope slide, the relative absorption spectra is calculated and shown in Figure 6-1. Also shown in the picture is the absorption spectra of bulk Yb:YLF from Ref. [182].

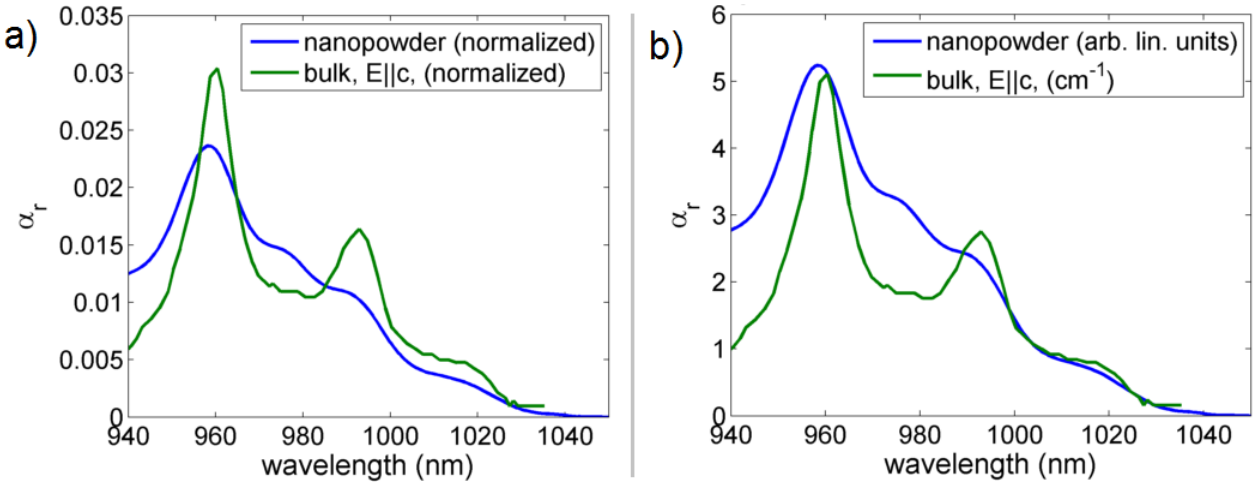

Figure 6-1: Absorption spectra of the 15 mol % Yb:YLF nanopowder, and a 5 mol % YLF bulk from Ref. [182]. (a) The absorption coefficient values are normalized to the area under the curve. (b) The absorption of the nanopowders is multiplied by an arbitrary value so that it matches the bulk absorption at a wavelength of 960 nm.

In Figure 6-1(a) it was assumed that the broadband absorption is the same for both forms, bulk and nanocrystals. From the resulting graph one can see that the nanopowder does not present an enhanced absorption coefficient in the long wavelength tail of the spectra when compared to the bulk form. Also a decrease in the absorption can be noticed at the peaks, due to the effective broadening caused by the random orientation of the nanocrystals. In a less realistic scenario, where the broad absorption in the nanopowder is much larger than that observed in the bulk form, and the absorption coefficients match at a wavelength of 960 nm, one can expect a relative reduction in the

absorption in the long wavelength tail, as can be seen in Figure 6-1(b). In the light of the above results it can be concluded that the absorption of low energy photons is not favored in the nanocrystals relative to the bulk form; the opposite happens. A more definitive conclusion should however be made once an absolute value for the absorption coefficient is obtained for the nanocrystalline powder.

6.1.3 Photoluminescence of the nanopowders

The photoluminescence spectra of the samples were measured by pumping with a 980 nm wavelength laser. For this part, the nanopowders mixed in water were used, so that the geometry of the probing region and the density of the emitters are kept the same when using different samples. In Figure 6-2 the emission spectra of the samples in a 1 wt. % concentration are shown.

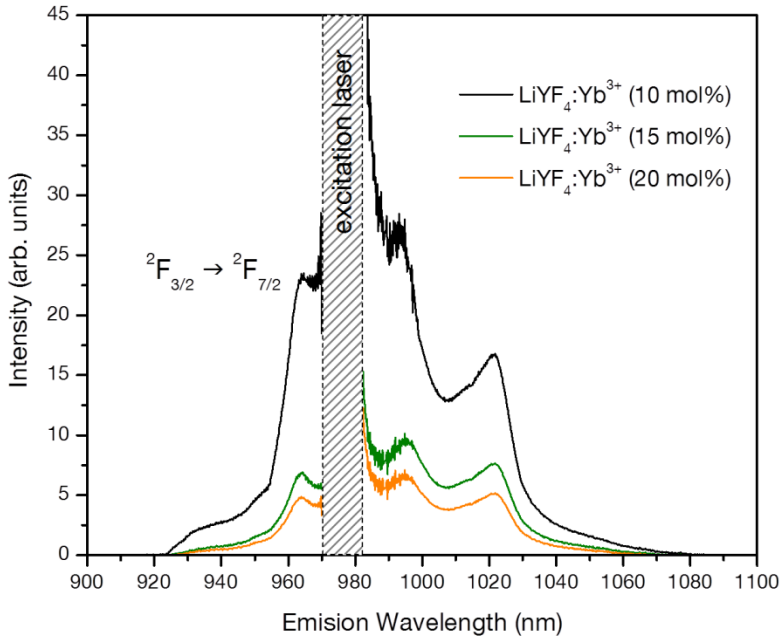

Figure 6-2: Emission spectra of the $^2F_{3/2} \rightarrow {}^2F_{7/2}$ transition after 980 nm laser excitation for the different samples in water.

As can be seen, the sample that shows the highest emission intensity is the one with $[Yb^{3+}]$ = 10 mol. %. To understand this, two effects must be considered. On one hand, smaller particles are generally better quenched. Quenching is in this case a surface-related effect. TEM images showed that in the present conditions, for higher concentrations, the nanocrystals are larger. The samples

with Yb^{3+} concentrations of 10 mol. %, 15 mol. % and 20 mol. % have approximate volumes of $(96 \pm 10) \times (63 \pm 5)^2$ nm^3, $(66 \pm 7) \times (45 \pm 5)^2$ nm^3 and $(70 \pm 7) \times (42 \pm 4)^2$ nm^3, respectively. Since smaller nanoparticles have larger surface-to-volume ratio, the quenching, or radiative decay suppression is stronger in this case [218], i.e. 15 mol. % and 20 mol. % of Yb^{3+} are more quenched than the sample with 10 mol. % Yb^{3+}. Additionally the effect of Yb^{3+} concentration should be considered. To a certain extent, a larger number of Yb^{3+} ions will account for a higher intensity. Nevertheless, a larger concentration is synonymous with shorter Yb^{3+}-to-Yb^{3+} distances, which means that the energy transfer processes between Yb^{3+} ions are favored at higher concentrations. Energy transfer can provoke the migration of light from ion to ion, eventually terminating in non-radiative decay, and this effect could slow down the intensity increase in the emission associated to the fact that at higher concentrations there are more ions that can emit. In our case, this last effect is probably responsible for the intensity decrease that is observed when $[Yb^{3+}]$ is increased from 15 mol. % to 20 mol. %. Up to this point, it can be concluded that for the synthesis parameters applied here, $[Yb^{3+}]$ = 10 mol. % is the optimum concentration. Nevertheless, this value could be different for different particles sizes.

For the quantification of the visible emission, the dried samples inside an integrating sphere were used, and measured the visible spectra using a Thorlabs SPLICCO CCD spectrometer (CCS), and the infrared spectra using an Ando AQ6317B optical spectrum analyser (OSA). In order to relate the measured power by these two instruments, a Ti:Sapphire laser operating at a wavelength of 960 nm and a white light source in conjunction with a large area photodetector are used as references. The visible and infrared spectra are shown in Figure 6-3.

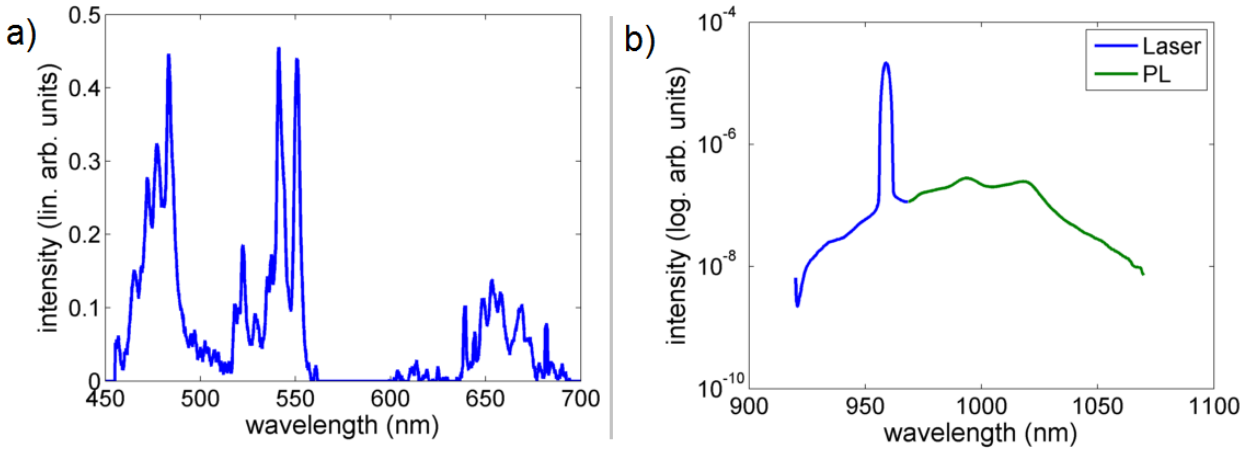

Figure 6-3: Visible (a) and near infrared (b) spectra of the Yb:YLF nanocrystals pumped at 960 nm, inside an integrating sphere.

The 480 nm wavelength emission of Yb^{3+}:YLF is due to thulium [219], and it takes three subsequent excitations using photons from the $^2F_{5/2}$-$^2F_{7/2}$ emission from the ytterbium ion. The 520 nm, 541 nm, 542 nm, 550 and 670 nm emissions are assigned to the presence of Er^{3+}. One can also see the 535 nm and 537 nm emissions, associated with the presence of Ho^{3+} [163]. These increase the number of non-radiative pathways, and can lead to a decrease in the external quantum efficiency. It was previously found that Thulium contamination does not affect the cooling efficiency significantly [163]. Using the broadband photodetector to bridge the power measurement by the OSA and the CCS, the visible upconversion power is estimated to be around 0.1% of the infrared emission. Since the visible spectrum is above a strong background from the Ti:Sapphire laser, it is difficult to estimate an exact value for the emission.

6.1.4 Lifetime of the nanopowders

For lifetime measurements, 940 nm wavelength emission from a Ti:Sapphire laser is used as the pump source, in the configuration shown in Figure 3-8, with 20 mW of power loosely refocused into the sample. The strongly scattered pump radiation is filtered by placing a 975 nm wavelength long-pass interference edge filter (Edmund Optics 86-065) between the telescope and the photodiode, rejecting 99.85 % of the on-axis 940 nm wavelength light.

For the 10 mol % sample, the powder was concentrated in a hand-made glass micro-vial (data of Figure 6-4 a), and then re-dispersed (Figure 6-4 b and c) to reduce possible optical cavity effects.

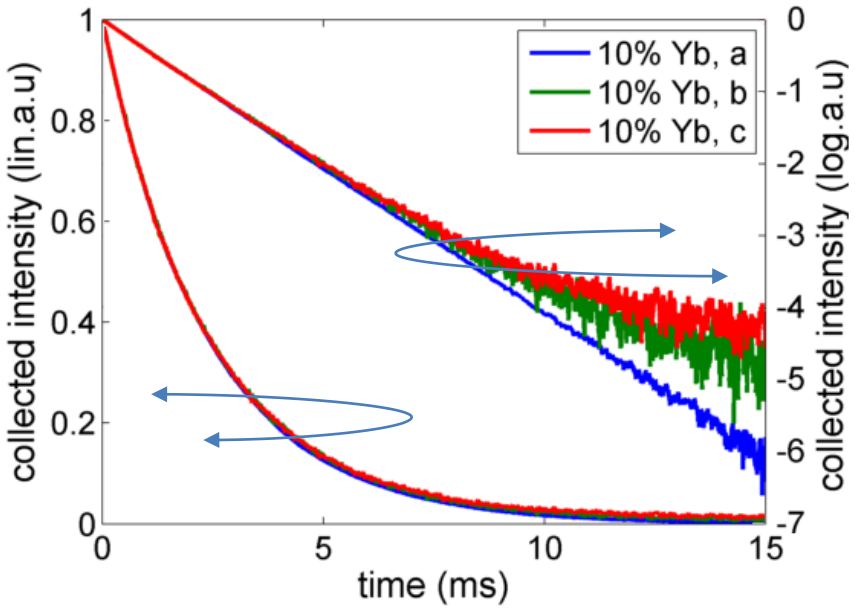

Figure 6-4: Decay curves of the near-1μm fluorescence intensity of a 10 mol % Yb:YLF nanopowder pumped with a chopped laser operating at a wavelength of 940 nm. The curves (b) and (c) were measured using significantly less amount of powder than for (a). In (b) the beam is focused and in (c) the beam is unfocused.

The other 15 mol. % and 20 mol. % samples were kept on top of a microscope slide, as in the previous case (b) and (c). These showed a much shorter lifetime than the 10 mol. % sample, as can be seen in Figure 6-5. The lifetime data is summarized in Table 6-1. The samples were pumped in different regions in (20 %, a) and (20 %, b), but showed no changes in the measured lifetime. Since the powder was accumulated by hand, it is assumed that different regions present different volumes, and as for the 10 mol. % sample, the volume does not play a significant role in the measured lifetime.

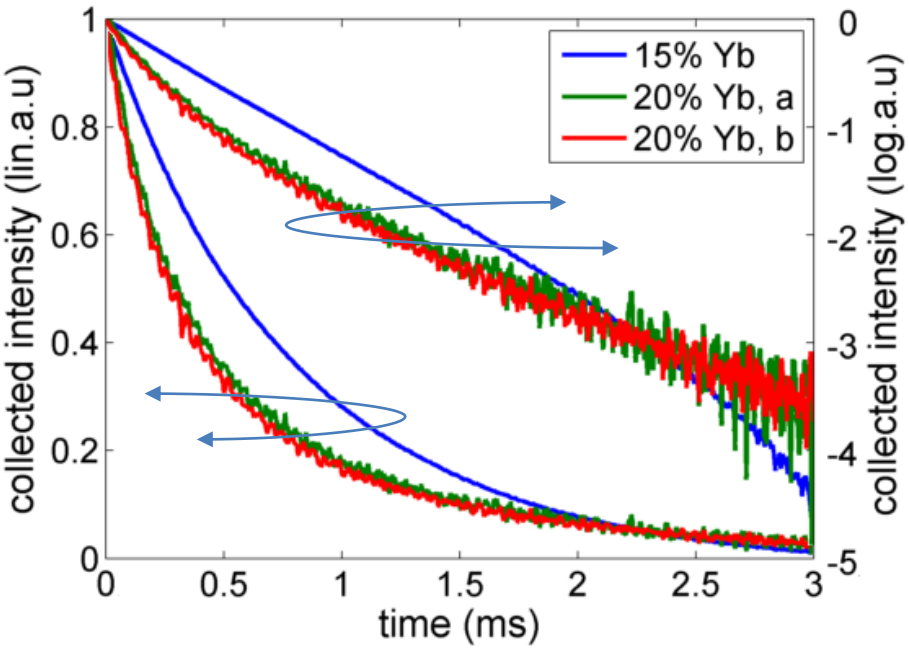

Figure 6-5: Decay curves of the near-1μm wavelength fluorescence intensity of 15 mol % and 20 mol % Yb:YLF nanopowders pumped with a chopped laser wavelength of 940 nm.

The logarithmic curves shown in Figure 6-5 do not fit to straight lines, which could be an indication of energy transfer processes taking place between the Yb^{3+} and impurity ions. However the exact process is not clear, as one can notice from the curvature differences between the data for the 15 mol. % and 20 mol % samples. Also, the same was observed for small-amount of the 10 mol. % sample (Figure 6-4, b and c), which could be an indication of errors due to the small signals of these measurements. Fitting the data to a single exponential to the data for the 10 % Yb sample gives a very good fit, and the difference between the results from the different arrangements is negligible, as one can see in Table 6-1.

Table 6-1: Fluorescence lifetime, single-exponential fit to decay curve of Yb:YLF nanocrystals.

Sample, measurement	**Lifetime and $\sigma_{fitting}$ (µs)**
10 mol % Yb, a	2405.4(13)
10 mol % Yb, b	2417.6(29)
10 mol % Yb, c	2383.1(28)
15 mol % Yb	814.4(13)
20 mol % Yb, a	507.0(46)
20 mol % Yb, b	494.4(43)

One can now observe how the measured lifetime of the excited state of Yb^{3+} in YLF nanopowders depends on the concentration and compare it with results of bulk samples from the literature. These results are shown in Figure 6-6, together with the best fit of Eq. (2) to our data as well as to the literature data.

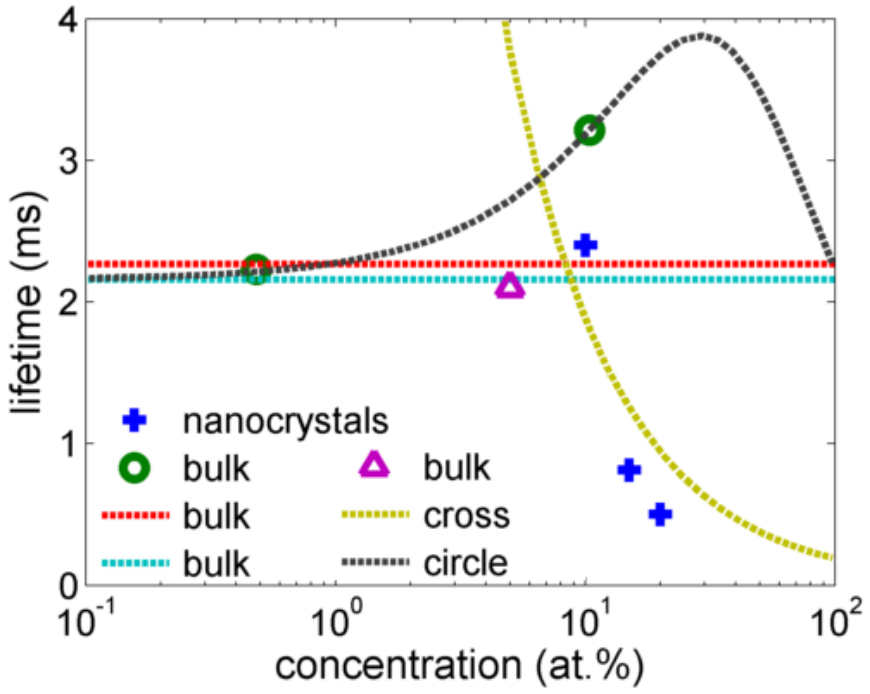

Figure 6-6: Measured lifetime (blue crosses) of the Yb:YLF nanocrystals, and results from literature. The data in represented as circles and triangles are from Ref. [220] and [221], respectively. Also shown are the fit to the literature data (circle) in dark gray, and the fit of our data (cross) in yellow. Horizontal lines corresponds to data from Ref. [123](red) and Ref. [203](cyan), with no information provided for dopant concentrations.

It is clear that the fluorescence lifetimes of the nanocrystalline samples is quenched for concentrations as small as 15 mol. %. The data is strongly dependent on the Yb^{3+} concentration, Equation (2) can be fitted to the bulk data, giving similar numbers to other reported values for low concentrations. For nanocrystals, the fit diverges and is therefore inconclusive. The critical concentration, from the fit for the nanocrystals data is 0.25 mol. %, while for the bulk it is at 52 mol. %. The exact lifetime dependence on the concentration should also take into consideration a fast diffusion process [222], where the energy is transferred to intrinsic non-radiative centers. However, the present data cannot fit a simple sum of fast diffusion and slow diffusion (Eq. 2) processes. One possible explanation is that the problem arises from a spatial dependence on the ion-concentration of the nanocrystals. To confirm this, a high resolution transmission electron microscopy measurement should be performed. It can be concluded however that the quantum

efficiency of the current nanocrystals is not as high as in the bulk, and no enhancement in the absorption was observed. Thus optical cooling is not expected on these samples in the present form.

6.1.5 Conclusion, nanocrystalline powders

The spectroscopic properties of ytterbium-doped nanocrystalline powders for optical refrigeration applications were investigated. Fiorenzo Vetrone's group at the INRS have synthetized Yb:YLF at three different dopant concentrations, and different nanocrystal size. From the absorption spectra, an improvement in the long-wavelength absorption tail which could enhance optical refrigeration cannot be seen as was theoretically suggested. The samples show visible emission to a level between 0.1 % and 1 % of the infrared emission power, and indicate the presence of other rare-earth impurities, leading to an increase in the possible non-radiative pathways, and which could further prevent cooling.

From the infrared photoluminescence spectra of the samples, a concentration which gives the global most intense emission could not be found, since the least concentrated one gives the local maximum intensity. This shows that quenching is present in much lower concentrations than expected.

Lifetime measurements confirm that the emission of the nanocrystalline samples is strongly quenched at relatively low concentrations (~15 mol. %) for this material. The much shorter lifetimes of the nanocrystals compared to the bulk counterparts further indicates that the quantum efficiency of the samples is too low to allow optical cooling to occur in their present form. Further investigation on the dopant concentration and spatial distribution in the crystals needs to be performed in order to find an agreement between the theoretical model and the experimental data. Further purification of the samples may lead to different results, but so far there is no clear indication that the properties of the nanocrystalline samples are more promising than those found in bulk hosts.

6.2 Optical cooling of glass-ceramics

Rare earth doped fluoride crystals and glasses have been the workhorse materials for optical refrigeration of solids [143]. They exhibit low phonon energy, desirable for reducing non-radiative decays or quenching [223]. The fluoride glass ZBLAN was the first solid-state material to be

optically cooled [19], but it has a higher phonon energy than other hosts used for cooling and it is a challenging material to prepare [224]. For instance ZBLAN has a maximum phonon energy of 580 cm^{-1} [105], while in PbF_2 crystals it is only 250 cm^{-1} [112]. The most often used optical cooling material to date is Yb:$YLiF_4$, a material of low maximum phonon energy – 450 cm^{-1} [225] – and which has been optically cooled to cryogenic temperatures [226]. High-purity single crystals are hard to mass-produce, and in the case of fluorides, are also hard to handle and polish [35], since they can be brittle and prone to chemical attack.

Nanocrystals of low phonon energy such as fluorides have gained attention recently mainly for their strong up-conversion processes due to weak quenching and strong absorption. These characteristics are desirable and useful for displays [227, 228], lasers, biomarkers [229], bioactuators [230], photovoltaics [231], and temperature sensors [130-132], to cite a few. A common route to use these properties in a robust material is to create a composite which shares the desirable optical properties of the nanocrystals with the mechanical and chemical properties of a glass host. In the case of upconversion applications, usually the crystals are co-doped with multiple types of ions for enhancing the absorption and enabling different emissions [232]. For laser cooling applications, the same properties of the host are desirable, but a single kind of dopant with a large bandgap is usually a safer way to avoid non-radiative decays, thus increasing the cooling efficiency [36], although multilevel cooling or the use of dopants with lower bandgaps than in Ytterbium are also useful candidates [233, 234].

Oxyfluoride CLYSiAl (cadmium, lead, yttrium fluoride and silicon and aluminum oxide) glasses with chemical composition $30SiO_2$-$15Al_2O_3$-(27-x)CdF_2-$22PbF_2$-$4YF_3$-$xYbF_3$, with x = (2, 5, 8, 12, 16 and 20) mol %, were subjected to different heat treatment to grow fluoride nanocrystallites within them. They were prepared by conventional melt-quenching technique. High purity (Sigma-Aldrich, 99.99%) precursors were well mixed in an agate mortar to obtain homogeneous powder, and were transferred to a covered platinum (Pt-100 %) crucible. The crucible was fired at 1100 °C for 2 h in a muffle furnace. The resulting molten glass was poured into a stainless steel mold that was pre-heated at the glass transition temperature, where the glass was annealed at the same temperature for 5 h to remove internal stresses and strains. The solid samples were cut and polished optically to dimensions 10 × 2 × 2 mm^3 for spectroscopic and cooling measurements. Some of the samples were not polished, but used for thermal and structural characterization. Further details on the preparations of these samples can be found in [86]. The samples are labelled as Yb*XXX*Glass

and Yb*XXX*GC for the glass and glass-ceramics samples, respectively, where *XXX* is the YbF_3 concentration in mol. %.

The glass samples were annealed at different temperatures and timescales to transform them into glass-ceramics (GC's). The whole synthesis was performed at ambient air at atmospheric pressure. A photograph of the 2 mol. % Yb-doped glass and the glass-ceramic samples is shown in Figure 6-7.

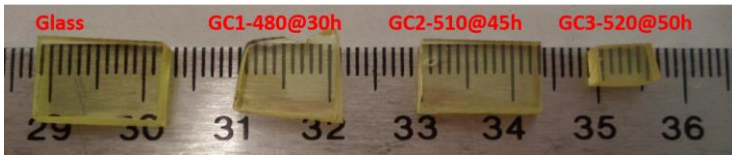

Figure 6-7: Photograph of the 2 mol. % Yb-doped glass and the glass-ceramic samples fabricated from a duplicate of the glass, after different annealing times.

The obtained GC's are ultra-transparent in nature, and the Yb002G and Yb002GC had their specific heat measured (Table 6-2), and used as reference for the other samples. After fine calibration with a sapphire reference as well as fused silica, the same setup was used to measure the thermal capacity of Yb002G, the Yb002GC3, and a glass-ceramic sample annealed for 25 h at 470 °C, which is used as reference for the Yb002GC1 and Yb002GC2.

Table 6-2: Sample preparation details and thermal properties

Sample	Annealing temperature (K)	Annealing time (h)	Specific heat capacity ($J.g^{-1}.K^{-1}$)	Mass (mg)
Yb002G	295	0	0.26(1)	331(6)
Yb002GC1	733	20	0.38(3)	317(2)
Yb002GC2	753	30	0.38(3)	371(5)
Yb002GC3	783	45	0.38(3)	215(3)

In order to estimate the effect of the annealing time and temperatures on the crystallization, X-ray diffraction (XRD) measurements were performed on samples of the same preparation as the YbG, GC1 and GC2, using a X-ray Bruker D8 Advance (CuKα12 radiation) equipped with a Vantec-1 linear detector. The resulting XRD profile is shown in Figure 6-8.

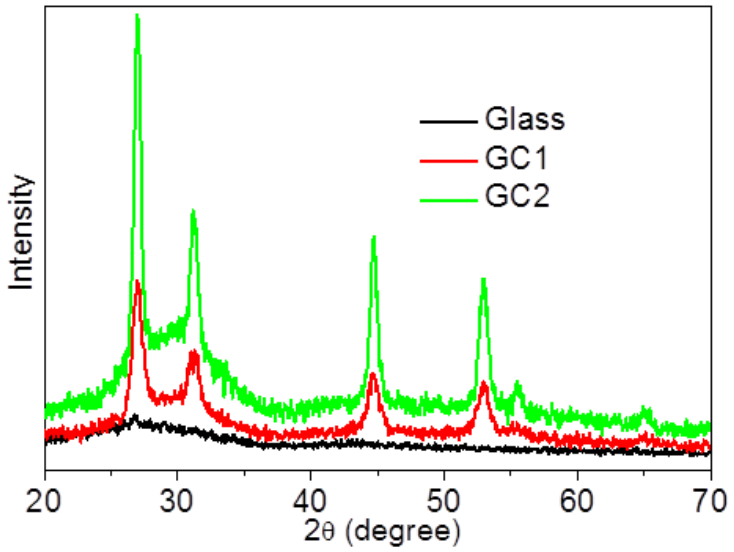

Figure 6-8: The XRD pattern of the 2 mol% as-made glass and glass-ceramics.

The glass-ceramics are free from any secondary phase crystals and uniformly dispersed β-PbF_2 nanocrystals were grown after appropriate thermal treatment. The XRD profile of glass contains two broad curves typical of amorphous structure whereas the GCs contain several sharp peaks related to the diffraction pattern of the crystalline structure, which can be identified as cubic β-PbF_2 nanocrystalline phase. The amount of crystalline phase improves with increasing the heat treatment temperature. The crystallite size of the nanocrystals was evaluated from transmission electron microscope (TEM) images of the samples (Figure 6-9) and was found to be less than 20 nm.

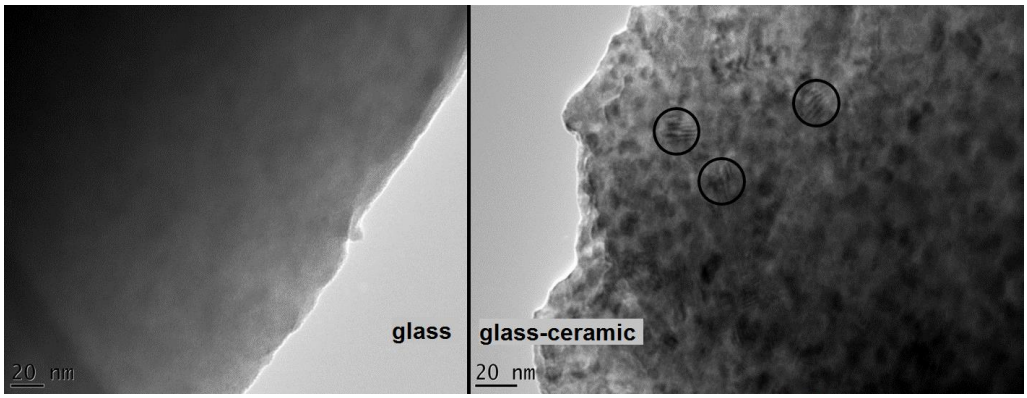

Figure 6-9: Transmission electron microscope images of a glass (left) and a glass-ceramic (right) sample. The nanocrystals are found to be smaller than 20 nm.

6.2.1 Depth and concentration-dependence of the photoluminescence spectra

The samples' photoluminescence spectra was measured by an Ando AQ6317B optical spectrum analyser (OSA) and a 200 μm-diameter optical fiber placed close to the sample, which is pumped using a Ti:Sapphire laser at a wavelength of 920 nm. The spectra for all the samples, for pumping at the surface, as well as at a depth of 1 mm from the collection surface, are shown in Figure 6-10 below.

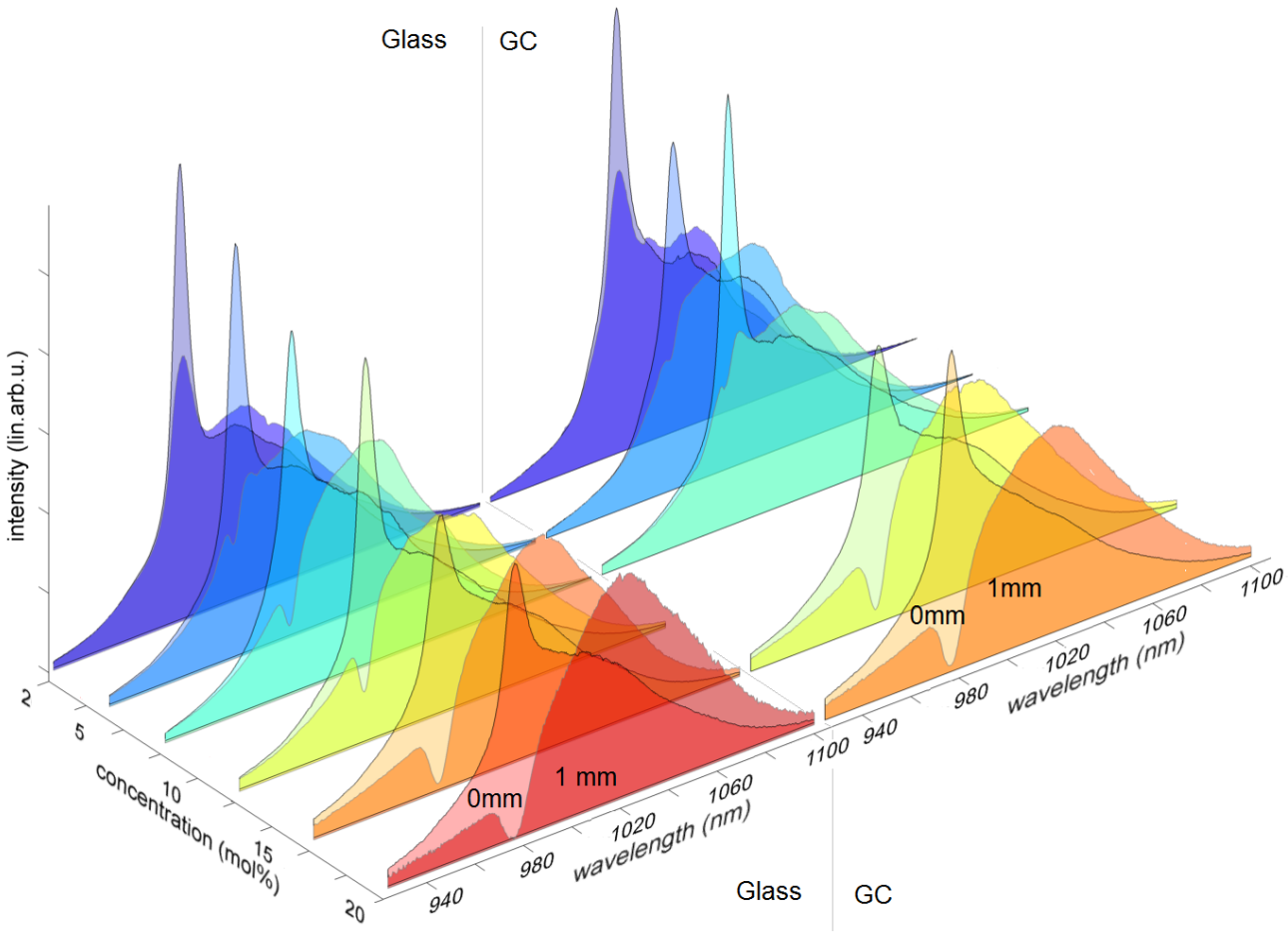

Figure 6-10: Photoluminescence spectra of the ytterbium doped CLYSiAl glasses (left side) and glass-ceramics (right side) for different pump-collection depth and dopant concentrations. The data corresponding to different depths for the same sample are overlapped to highlight the red-shift introduced by re-absorption – the curves with sharper peaks corresponding to 0-mm-depth collection. The colors represent qualitatively by how much the escaping fluorescence is red-shifted.

The mean fluorescence wavelength λ_f of the samples is calculated from the photoluminescence (PL) data at a 1 mm depth on the sample, where it is pumped for the calorimetric measurements. For comparison the PL is also made at the sample surface, and the results are shown in Figure 6-11.

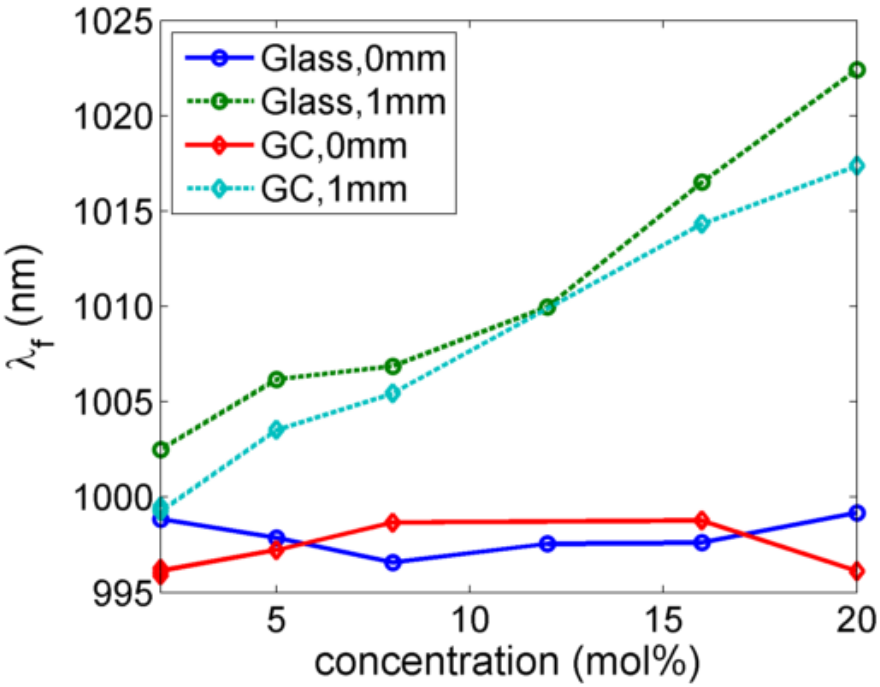

Figure 6-11: Mean fluorescence wavelength of the photoluminescence as a function of the dopant concentration and pump-collection depth.

From the graphs shown in Figure 6-10 and Figure 6-11 it can be seen that although the intrinsic mean fluorescence wavelength in the glass and glass-ceramics is essentially the same, the external mean fluorescence wavelength (eMFW) is consistently longer for the glass samples. The observed red-shift on the eMFW is expected due to the inner-filter effect. For fluorophores of high efficiency, the total observed spectra is a mixture of the filtered primary emission (from directly excited ions) with the secondary emission (from subsequently excited ions closer to the surface). It is expected that, the higher the quantum efficiency of the material, the higher is the contribution of these secondary emissions, which present less filtering and thus are less red-shifted. In addition, used for the calorimetric calculation, the measured eMFW is an indication of the higher quantum efficiency of the glass-ceramics, compared to the glassy precursor.

6.2.1.1 Quantum efficiency measured by integrating sphere and from the lifetime

In order to make a study of the optimal concentration for laser cooling, the quantum efficiency is first measured using an absolute method such as the integrating sphere, which is less time consuming than calorimetric methods. With this one can estimate which samples have the potential for laser cooling. The integrating sphere method [127] was used as the absolute method, which was assessed using an already optically-cooled Yb:YAG crystal [85]. The samples were pumped inside an integrating sphere (ISp) using 200 mW from a Ti:Sapphire laser set to a wavelength of 915 nm, while the minute fluctuations of a fraction of the pump power, tapped by a glass plate, were monitored by a photodetector and picoamperimeter. The diffused photoluminescence, from direct and indirect excitation, as well as the diffused pump transmission and scatter are collected by a 200 μm optical fiber and measured by an Ando AQ6317B optical spectrum analyzer. An ensemble of 50 spectra are measured for each sample, for each of the conditions: A – the integrating sphere is empty; B – the sample is inside the ISp, but it is out of the pump beam path, and C – the sample is inside the ISp, and is directly irradiated by the pump beam. The spectra measured for the Yb008Glass are shown in Figure 6-12 as a reference.

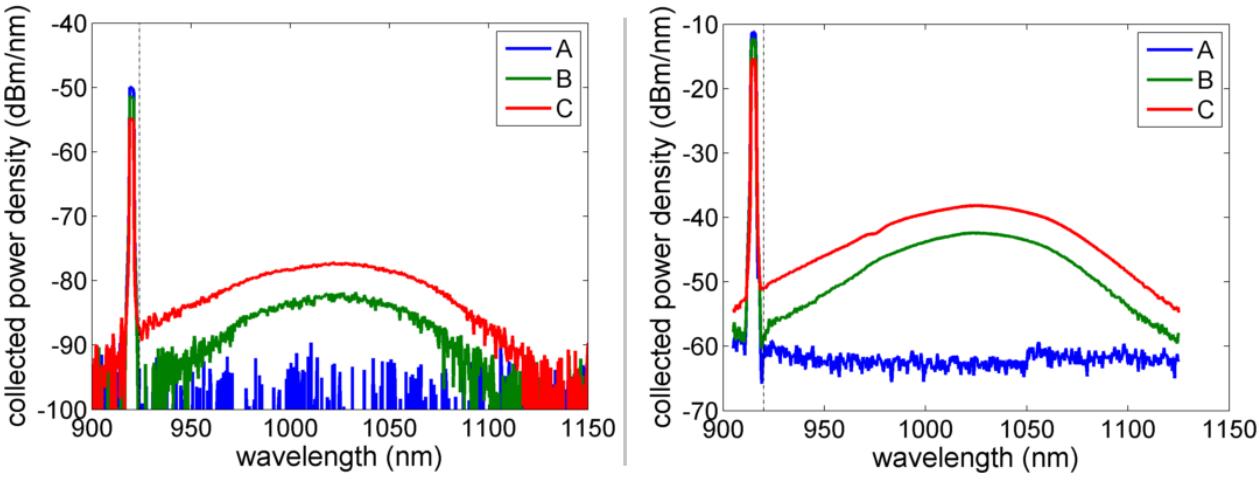

Figure 6-12: Spectra of the 8 mol. % Yb:CLYSiAl glass sample inside the integrating sphere while pumped directly (C) and indirectly (B) at 915 nm, and the diffused pump (A). Left: single measurement. Right: 50 times – averaged data, each normalized by the power tapped from the Ti:Sapphire laser.

The integral of the photon number in the pump wavelength region L_i and the photoluminescence wavelength band P_i, i = (A,B,C) is used to calculate the quantum efficiency with (6.1), as per [127].

$$\eta_{ext} = \frac{P_C - (1-A)P_B}{L_A A}, \quad A \equiv 1 - \frac{L_C}{L_B}. \tag{6.1}$$

The results of the calculation of (6.1) to the measured spectra are summarized in Table 6-3.

Table 6-3: Quantum efficiency of the CLYSiAl samples in different forms, as measured by the integrating sphere method.

Concentration (mol. %)	**Glass**	**GC**
02	0.88	0.97
02, 2nd		0.98
02, 3rd		0.85
05	0.46	0.60
08	0.14	0.35
12	0.06	--
16	0.02	0.03
20	0.01	0.02

From Eq. (2.5), it is straightforward to see that a minimum condition for cooling to happen is that $\eta_{ext} > \lambda_f/\lambda_p$. Since the resonant absorption is limited to $\lambda_p < 1050$ nm, and $\lambda_f > 995$ nm, the external quantum efficiency must be at least 0.95 for an ideal sample. That implies that from the measurements with the integrating sphere, only the Yb002GC samples have the potential for optical cooling. It must be noticed that the integrating sphere method does not discriminate between energy loss from background absorption of the pump photon, or multiphonon and other nonradiative losses of an excited electron, thus it underestimate the quantum efficiency of high-background loss samples.

An alternative way to estimate the quantum efficiency of excited electrons is to look at the radiative decay rate, or lifetime. A drawback of this method is the need for the knowledge of the intrinsic radiative lifetime, as well as taking into account cavity effects, which can increase the apparent lifetime of an excited state. These problems can be circumvented by using equivalent systems of different dopant concentrations, and by fitting the lifetime data to a concentration-dependent model of radiation trapping and self-quenching, which can be described by (6.2).

$$\tau_{\text{measured}} = \frac{\tau_0 \left(1+\sigma_a l N_{Yb}\right)}{\left[1+\frac{9}{2\pi}\left(\frac{N_{Yb}}{N_0}\right)^2\right]}, \tag{6.2}$$

where l is the average absorption length of the sample, σ_a the absorption cross-section of the transition, N_{Yb} is the Yb^{3+} concentration, N_0 is a critical concentration for self-quenching and τ_0 is the measured lifetime at very weak concentration [222]. The last term in the numerator accounts for radiation trapping, which delays the energy escape. The second term in the denominator accounts for concentration quenching.

The excited state lifetimes of the samples were measured by pumping them with 20 mW of power at a wavelength of 940 nm from a chopped beam from a Ti:Sapphire laser. The emission is filtered using a 975 nm wavelength longpass interference edge filter, and monitored by a 4-*f* telescope and a silicon photodiode of 13 mm^2 area (Thorlabs SM05PD1B). The signal is amplified by a benchtop transimpedance amplifier (Thorlabs PDA200C) and displayed on an oscilloscope (Tektronix TDS7104). The data is fit to single exponential decays quite well, as shown in Figure 6-13 for two samples. The calculated lifetimes for all the samples are shown in Figure 6-14, plotted together with the best fit to (6.2).

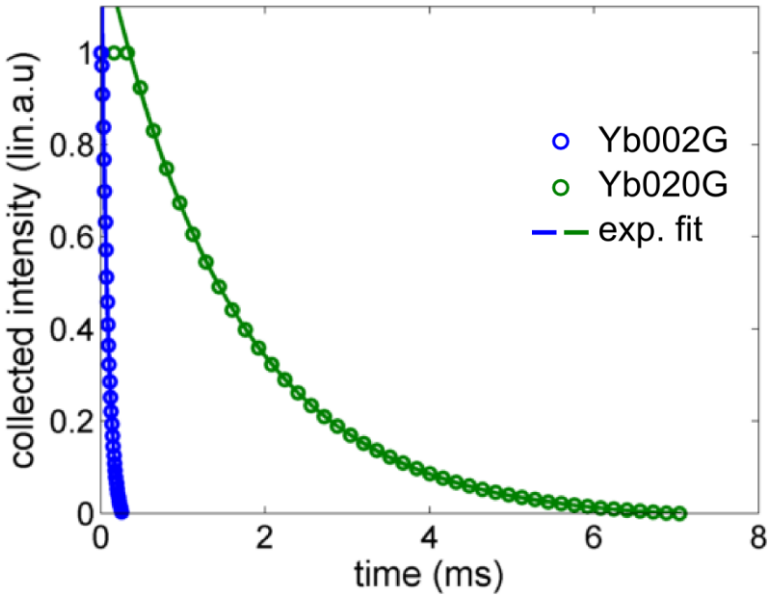

Figure 6-13: Measured lifetime (circles) of Yb-doped CLYSiAl glasses. The lines represent the best fit of the data to a single exponential decay function.

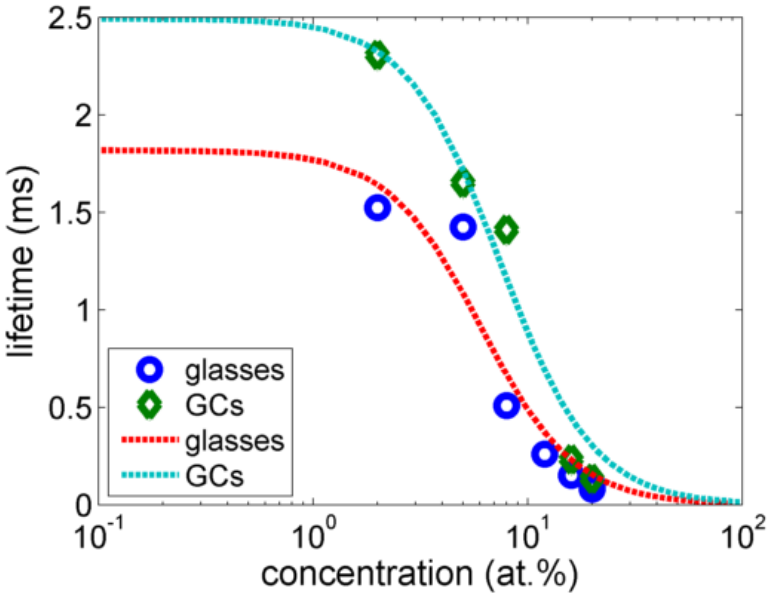

Figure 6-14: Measured lifetime of Yb-doped CLYSiAl glasses and glass-ceramics, as a function of the Yb^{3+} concentration. The lines represent the best fit of the data to a slow-diffusion process of self-quenching and radiation trapping.

Since no evident radiation-trapping was observed – which would appear as an increase in the lifetime with concentration, one can consider only concentration-quenching, thus the measured lifetime is a good representation of the quantum efficiency of the samples at a given concentration. Also, the intrinsic radiative lifetime can be estimated by extrapolating the data to the very low concentrations. Thus, from the data and fit shown in Figure 6-14 the quantum efficiency of the samples is calculated as $\eta_e = \tau_{emeasured}/\tau_0$ [235], and the results are presented in Table 6-4.

Table 6-4: Quantum efficiency of the CLYSiAl samples, estimated from the lifetime measurements, and intrinsic lifetime from fit.

Concentration (mol. %)	**Glass**	**GC**
02	0.84	0.93
05	0.78	0.66
08	0.28	0.57
12	0.15	--
16	0.08	0.09
20	0.06	0.05

As observed from the measurements with the integrating sphere, the samples with higher quantum efficiency are the doped at a concentration of 2 mol. % Yb. The results from the lifetimes differ by less than 5 % from the values obtained with the integrating sphere for the Yb002Glass and Yb002GC. As the concentration increases, the quantum efficiency decreases but the results from the different methods differ. It is indeed expected that the integrating sphere method underestimate the η_e for samples with high background absorption, since it leads to a total photonic energy loss which includes the non-resonantly absorbed photons. On the other hand, the calculated quantum efficiency from lifetime measurements depends on the precise knowledge of the intrinsic radiative lifetime. That can lead to large errors, especially for systems in the early stage of investigation, where data from the literature is scarce. The result indicates that the addition of the dopant increases the background absorption. Both methods show than the samples with more than 5 mol. % Yb, in the present form, cannot lead to optical cooling. Thus the calorimetric investigation are limited to

the Yb005Glass and Yb005GC, in order to compare them to those previously measured, Yb002Glass and Yb002GC.

6.2.2 Calorimetry of the glasses and glass-ceramics

The samples were placed in a sample holder consisting of eight 1-mm-thick vertical steel rods, which holds four 125 μm optical fibers to clamp the sample to minimize conduction heat loads and clamp heating due to the pump and fluorescence. A fiber Bragg grating (FBG) is placed on the top of the sample to measure the sample's temperature continuously during the experiment, including during the pumping. The FBG temperature is interrogated by a narrow wavelength probe and an optical fiber power meter, as shown in Figure 6-15.

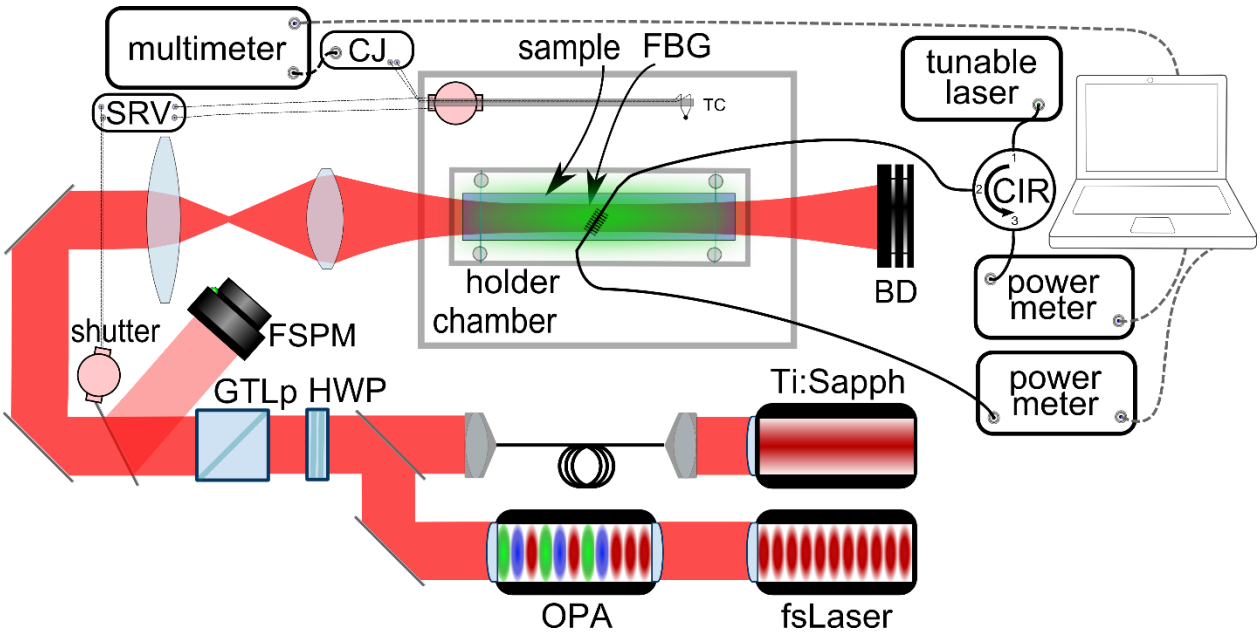

Figure 6-15: Diagram of the setup for optical calorimetry experiments with the glass and glass-ceramics. The output power from a Ti:Sapphire laser or an optical parametric oscillator is controlled by a half-wave-plate (HWP) and Glan-Thompson polarizer (GTLp) and interrogated by a free-space optical power meter (FSPM). A servo controller (SRV) drives the thermocouple (TC) and the shutter mirror position. An electronic cold junction compensator (CJ) and a multimeter interrogate the TC. The laser beam is recollimated into the sample and the transmitted power is dumped in a beam dump (BD). The temperature of the sample is monitored by a fiber Bragg grating (FBG), which is interrogated by a tunable laser, optical circulator (CIR) and power meter which measure the reflection and transmitted power and send the data to a computer.

6.2.2.1 Samples with different crystallization levels

Initially the work concentrated in the more promising samples, Yb002Glass and the corresponding glass-ceramic annealed at different temperatures. The samples exhibited heating rather than cooling for the pump wavelengths used here, and their heating spectra is shown in Figure 6-16. The best fit of (5.5) is shown in the figure as the green solid curve, while the curves corresponding to 95% confidence interval of the fitted η_c and α_b are shown in dashed curves. The absorption coefficient is also plotted as a function of wavelength for a reference.

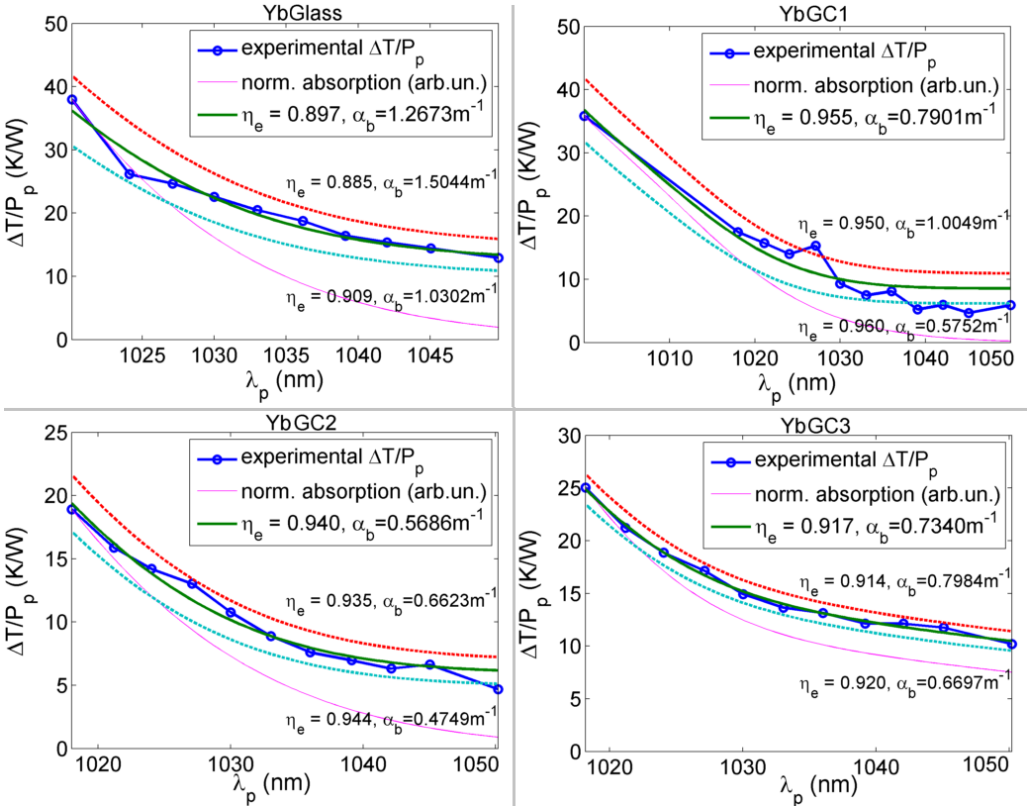

Figure 6-16: Heating spectra of the samples, i.e. the temperature rise divided by the pump power, as a function of the pump wavelength. The experimental data is shown in blue circles and the absorption profile is shown as the pink thin line. The best fit to the data is given by the green curve. The two adjacent dashed curves correspond to the confidence intervals of the fitted parameters, whose values are shown next to the curves.

From the data in Figure 6-16, it can be observed that the glass-ceramics presented higher quantum efficiency and smaller background absorption than their glass precursor. In the long wavelength tail of the spectra, where the resonant absorption is weak, Yb002G showed the highest temperature, which is due to background absorption. At the same time, a temperature rise of 40 K/W is observed in the glass when pumped at 1020 nm, a level which is not observed in the Yb002GC1 even at the 1000 nm wavelength, where the resonant absorption is much higher. The same is observed in Yb002GC2 and to a lesser extent in the Yb002GC3. That indicates a better ratio of anti-Stokes emission to non-radiative decay in the GCs when compared to the glass. Table 6-5 summarizes the findings and fitted data. This impact on the quantum efficiency was expected, since a fraction of the ions are within a lower phonon-energy host than the ions hosted in a glassy matrix. An explanation for the decrease in the background absorption is less trivial. In a first instance, the annealing may relief some stresses or inhomogeneities which are partially responsible for background absorption. The material structure data at the present is insufficient to determine the exact mechanism responsible for the reduction in α_b. With further annealing, the size of the crystallites increases, and so does the scattering increase, leading to an indirect increase in the background absorption.

Table 6-5: Samples' photophysical properties

Sample	λ_f (nm)	η_{ext}, int. sphere	η_{ext}, calorimetric	α_b (m^{-1})
3%Yb:YAG	1010(1) [34]	1.02(12)	0.991(1) [34]	0.029(1) [34]
Yb002G	1003(1)	0.88(9)	0.897(6)	1.27(10)
Yb002GC1	1000(1)	0.97(4)	0.955(3)	0.790(11)
Yb002GC2	999.4(10)	0.98(12)	0.940(2)	0.569(47)
Yb002GC3	999.3(10)	0.85(12)	0.917(2)	0.734(33)

The same fitted exponential used to calculate the equilibrium temperature can be used to obtain the thermal equilibrium time τ_h which together with the thermal capacity of the sample, can be used to deduce the sample-environment thermal coupling coefficient κ. This allows us to better evaluate

the material rather than the physical sample, by calculating the materials cooling figure of merit (CFOM), shown in Figure 6-17Figure .

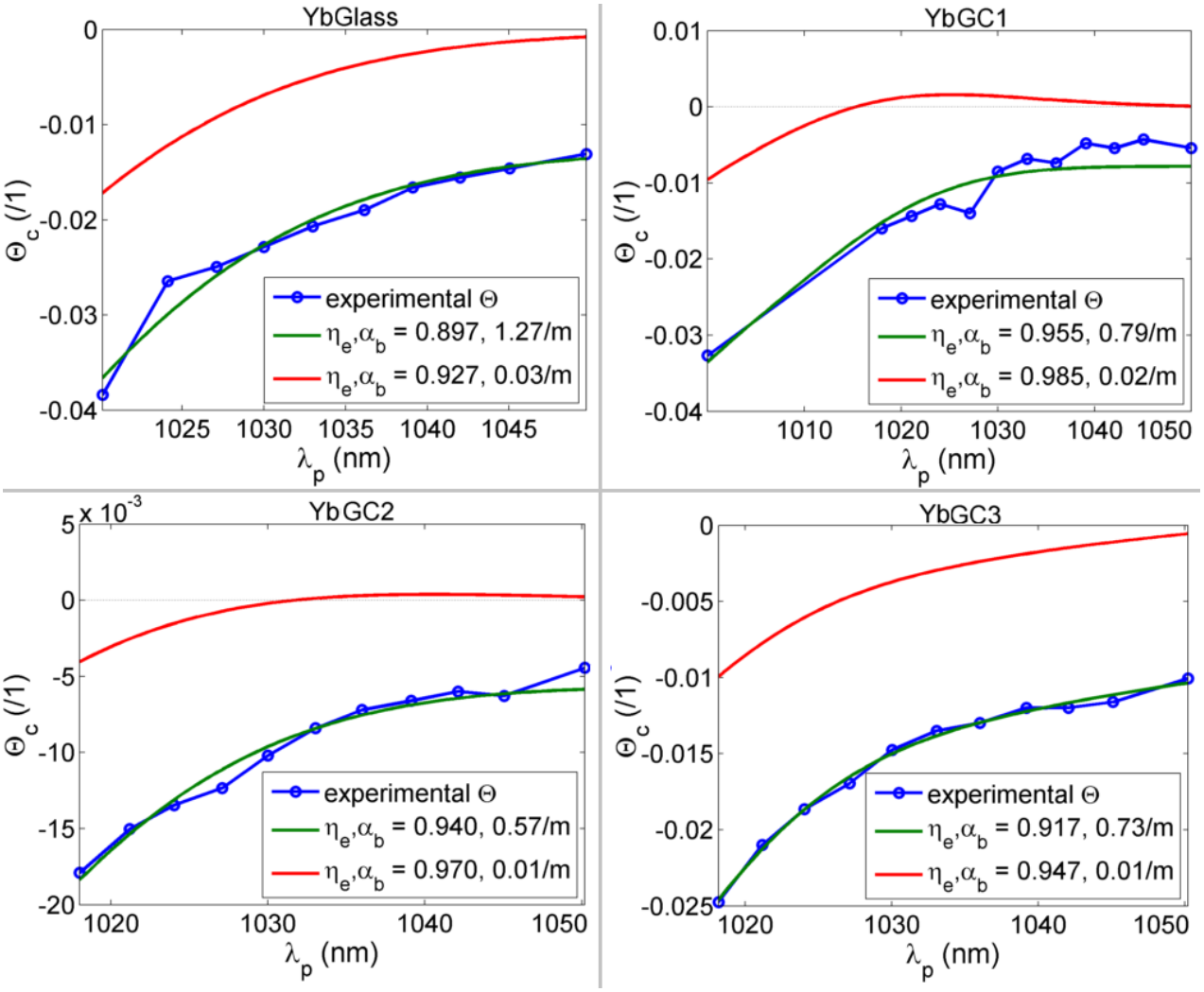

Figure 6-17: Cooling figure-of-merit spectra of the samples. In red: theoretical Θ_c based on the experimental data with an improvement $\Delta\eta_{ext} = 0.03$ and $\alpha_{b,new} = \alpha_b/50$.

The cooling figures-of-merit shown in Figure 6-17 reproduces the same qualitative behavior as seen in Figure 6-16, but without the ambiguity that the samples' dimensions and thermal coupling with the environment could influence if they were dissimilar. Evidently, the quantitative behavior, thus the cooling parameters are the same as before, since the model already takes the thermal coupling into account. From the present results, it is obvious that the samples need improvement before showing a positive cooling figure-of-merit. The red curve on Figure 6-17 shows what would

be the CFOM if the quantum efficiencies were higher by 0.03 and the background absorption lower by a factor 50, which would lead GC1 to cool by 1.75 K/W. If η_c were as high as in the Yb:YAG, GC1 could cool by -3.1 K/W, which corresponds to a final temperature difference of -13.0 K, for the same 4.2 W of pump power which drove the Yb:YAG sample 8.8 K below the chamber temperature. While the glass sample would still heat, it is clear that the Yb002GC1 and Yb002GC2 would cool, showing that the low-temperature glass-ceramic performs better than the glass. Given the present exploratory preparation conditions, these factors are feasible with further purification of the precursors. For instance purification methods developed for cooling have achieved better than 1000-fold reduction in transition metal contamination in ZBLAI glass [236], and intense research has achieved similar results in crystal purification as well [226]. On the other hand, glass-ceramics are much easier to manufacture on a large scale than are single crystals. The optimal cooling wavelength for Yb002GC1 is 1025 nm, and for $\eta_{ext} < 0.975$ no cooling is possible at this pump wavelength, independently of the value of the background absorption. Due to this specifity, it is worth mentioning that, in addition to optical refrigeration, these samples are strong candidates for quantum efficiency references at the near-infrared region, if indeed optical refrigeration becomes a reality with them.

6.2.2.2 Samples with higher dopant concentration

From the results of the spectroscopy section, no cooling is expected for the samples with ytterbium concentrations of 5 mol. % or higher, since the heating due to low QE and background absorption will be much higher than anti-Stokes cooling. However, while Yb005Glass and Yb005GC show relatively low quantum efficiency, it is interesting to make an independent measurement of their cooling performance, and verify which form is better, as well as how they compare with the Yb002Glass and YB002GC. Using the same procedure used in the last section for different crystallization, the figure of merit of the samples with concentration 5 mol% Yb is calculated. The results are shown in Figure 6-18. It is also estimated what would be the cooling figure of merit, if the samples quantum efficiency where improved by 0.03 and the background absorption reduced by a factor 50.

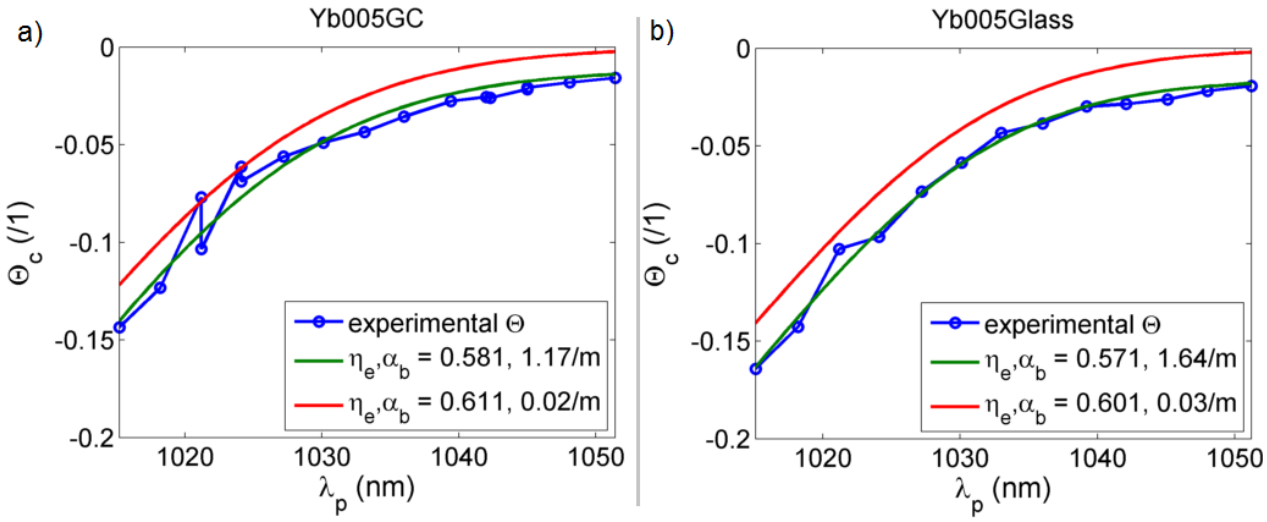

Figure 6-18: Cooling figure-of-merit spectra of the samples. In red: theoretical Θ_c based on the experimental data with an improvement $\Delta\eta_{ext} = 0.03$ and $\alpha_{b,new} = \alpha_b/50$.

The results from the calorimetry confirm the results expected from the spectroscopic characterization. The data is summarized in the Table 6-6.

Table 6-6: Photo-physical properties of the glass and glass-ceramic samples, as measured by different techniques.

Sample	QE from ISp	QE from lifetime	QE from calorimetry	α_b (m^{-1}) from calorimetry
Yb002G	0.88	0.84	0.897	1.27
Yb002GC1 (best)	0.97	0.93	0.955	0.79
Yb005G	0.46	0.78	0.571	1.64
Yb005GC	0.60	0.66	0.581	1.17
Yb008G	0.14	0.28	--	--
Yb008GC	0.35	0.57	--	--
Yb012G	0.06	0.15	--	--
Yb016G	0.02	0.08	--	--

Table 6-6: Photo-physical properties of the glass and glass-ceramic samples, as measured by different techniques **(cont'd)**

Yb016GC	0.03	0.09	--	--
Yb020G	0.01	0.06	--	--
020GC	0.02	0.05	--	--

There is a good agreement between the calorimetric results and the integrating sphere method, although the latter shows smaller quantum efficiencies. This is expected, since the integrating sphere accounts for all the losses including non-resonant absorbed photons. The lifetime method gives different values from the other techniques, since it relies on more assumptions about the samples, compromising the accuracy of the calculations. However the same concentration quenching trend is observed. The general trend is that, as the concentration of the dopant is increased, the quantum efficiency decreases and the background absorption increases. However, after the precursor glass is heat treated in order to form the glass-ceramic, an improvement in the quantum efficiency is observed for all the samples, and a decrease in the background absorption of the four samples investigated by calorimetry. The enhancement in the quantum efficiency is already expected, since the nanocrystals present in the glass-ceramics have lower maximum phonon energy than the glassy counterpart. However the mechanism responsible for the decrease in the background absorption is not obvious and requires further investigation. The background absorption can be measured by a complementary and independent measurement, using a pump source out of the resonance used for cooling, e.g. using an optical parametric oscillator as shown in Figure 6-15. The experimental setup is set and the measurements are under way.

The quantum efficiency of this first batch of glass-ceramics, prepared at ambient air, is comparable to the most efficient laser materials. A list of some of the results on the quantum efficiency reported in the literature is shown in the Table 6-7.

Table 6-7: Quantum efficiency of typical laser materials, and the method utilized.

Material	QE	Method, reference
8% Yb:YAG	0.7	Thermal lens, [237].
1% Yb:YAG	0.93, 0.90	ISp and calorimetric*, [238].
5-100% Yb:YAG	0.94-0.97	Calorimetric, intrinsic QE, [205].
2.3 % Yb:YAG	0.988	Calorimetric, thermal camera, [122]. Cooled.
5.6% Yb:YAB	0.88	Interferometric, [239].
1-2% Yb:ZBLANI	0.991,0.994	Calorimetric, thermal camera, [137]. Cooled.
5.7% Yb:GGG	0.9	Thermal lens, [237]
15% Yb:GdCOB	0.71	Thermal lens, [237]
15% Yb:YCOB	0.90	Thermal lens, [237]
5% Yb:KGW	0.96	Thermal lens, [237]
5% Yb:YSO	0.89	Thermal lens, [237]

*does not mention the sensor

The external quantum efficiency is not a general property of a material, but a parameter that describes a given sample [237], and depends on its history: the dopant concentration, growth technique and growth environmental conditions, as well as the purity of the starting materials. This can be readily verified from the Table 6-7, as well as from the results obtained for my samples. From the global results one can see that in glass-ceramics all cooling-relevant parameters are enhanced in comparison to their glassy counterparts. Cooling was not observed in any of the present samples. An evident next step is to prepare new samples at various concentrations below 5 mol. %, reduce the impurities of the starting materials, and to prepare the samples in a controlled, clean and dry atmosphere.

6.2.3 Conclusion, oxyfluoride glasses and glass-ceramics

Ytterbium-doped transparent glass and glass ceramics were fabricated by collaborators at Laval University, and their thermal and spectroscopic properties were measured in this Thesis. The results

above correspond to the first time one has measured cooling figure-of-merits of glass-ceramic. The calorimetric results on the quantum efficiency of the samples are in line with the results obtained using an integrating sphere, showing an above 0.9 quantum efficiency for all the samples with concentration of 2 mol % of Yb. It has also been shown for the first time, the use of an optically-cooled sample as an accurate reference for quantum efficiency measurements. It is estimated that the use of a glass-ceramic could lead to an accuracy in the measurement of QE to better than 2.5 %. As expected, nonradiative decays are considerably reduced in the glass-ceramics when compared to those seen in glass. Hence, rare earth doped glass-ceramics offer a promising path towards samples with higher efficiency for use in optical refrigeration and metrology, with a much more scalable production method than crystals. Also shown here is, that further precursor purification will ultimately lead to samples which may exhibit laser induced cooling

The quantum efficiency of samples with various concentrations of ytterbium-doped oxyfluoride glasses and glass-ceramics is investigated, using three different techniques, and measured the background absorption of the most prominent ones by an optical calorimetry technique. The depth-dependence of the mean fluorescence wavelength of all the samples are measured, showing that reabsorption is less pronounced in the glass-ceramics, which can be attributed to their higher quantum efficiency.

It is shown that the crystallization of the samples leads to and enhancement in the optical cooling-relevant parameters, for all the investigated concentrations. Preparation of samples in better controlled conditions, and with precursor materials of higher purity could reduce the impurities responsible for the background absorption and for part of the quantum efficiency quenching. Also, a lower range of sample concentrations should be investigated in order to find the optimal concentration and growth parameters which could ultimately lead to optical cooling. A successful outcome would translate to samples which are easier to fabricate and handle than current optically-cooled materials, thus allowing a wider range of applications for optical cooling technology.

CHAPTER 7 CONCLUSION

Summary

The work presented in this thesis is directed towards the realization of optical refrigeration in a solid, in environmental conditions close to that found in everyday devices. Although the technology has shown to be promising for cryogenic applications, few reports can be found on the implementation of optical cooling in a relatively simple and scalable way. This Thesis presents the first realization of optical cooling in air at atmospheric pressure. Also presented for the first time is a fiber Bragg grating used for temperature measurements in laser cooling. The potential for laser cooling of two new materials: glass-ceramics and ytterbium-doped nanocrystals was also studied experimentally for the first time.

The first part of this thesis concentrated in the design of the scientific tools used to conduct the main optical cooling experiment. The first innovation presented was a simple technique which allows photoluminescence measurements of highly scattering samples under high power any-wavelength pumping, with no need of a set of filters. The second is to use optically-cooled materials as quantum efficiency standards. The main tool developed here concerns thermometry. Several works in the field were plagued with disputable results, mainly due to the non-triviality of temperature measurements in laser cooling of condensed media. It is shown in this thesis that one can obtain the main advantages of the use of a contact sensor which is reliable and easy to use, at the same time avoiding heating from the intense fluorescence present in optical refrigeration. This is achieved through the use of fiber Bragg gratings (FBGs), which in addition to the aforementioned advantages, can be directly integrated in an all-optical device as well as to be interrogated remotely. The last step in order to show that FBGs are applicable to most optical cooling experiments was to show that they can be used in a cryogenic environment. Most of the divergences found on the literature concerning the employability of FBGs at cryogenic temperatures were solved first, by the careful modeling of the fibers thermo-optical and mechanical properties. In addition, the issues were solved by the experimental demonstration of these sensors sensing 0.25 K changes or less in the whole temperature range when interrogated using a simple spectral method. The sensitivity of FBG has also shown to be able to measure optical cooling with low pump powers.

The implementation of optical cooling in a relatively simple way translates initially to the first demonstration of laser induced cooling of solids (LICOS) at atmospheric pressure, which was demonstrated here using an ytterbium-doped YAG crystal, an ubiquitous laser material. This work also presents the cooling of a solid external heat load of mass comparable to the refrigerator itself, as a proof-of-concept that emphasises the macroscopic nature of optical refrigeration applications. It was also shown that the reduction of the dimensions of the optically-cooled sample implies in a reduction on the heat load posed by the surrounding environment, thus it allows the solid to reach lower temperatures than a larger sample would achieve. Concomitantly to the reduction of the thermal load, the cooling efficiency is reduced with the size-reduction, due to absorption saturation effects which although small, can counteract cooling. Thus, there is an optimal dimension so that one achieves maximum temperature drop for a given sample, pumped at a fixed optical power. With these effects on mind, but limiting to fabrication constraints, it was possible to show optical cooling to similar temperatures achieved before in vacuum for the same material and pump power, this time in air at atmospheric pressure. This achievement shows that one can use optical cooling in conventional devices, and that one can study optical cooling without cumbersome equipment. It also simplifies the experiment, and therefore accelerates the search for new materials for optical cooling.

While the primary investigations help with the advancement of laser cooling science, another main issue which could prevent the widespread use the technology is the relatively small and exclusive pool of materials available for optical refrigeration. Previous breakthroughs in laser cooling were achieved using expensive and hard to fabricate and to use, fluoride crystals and glasses. In this thesis it is investigated the cooling potential of ytterbium-doped-oxyfluoride glasses and glass-ceramics, which have showed promising properties such as high quantum efficiencies. With further improvement on the preparation of these materials, they are expected to show optical refrigeration.

Therefore the main contributions of this thesis are the demonstration of optical cooling of a solid at atmospheric pressure, and unambiguous interpretation of the cooling signal at a broad temperature range. The design recipes given here simplify the study and open the possibility for other researchers to join the efforts on the advancement of laser cooling science, without the need of vacuum chambers, powerful lasers, and without complex and error-prone thermometric setups.

Sequels

As with any research, its progress affects an intangible number of other fields. When it involves lasers, predictions of the full impact of the research become even more complex to make, due to the ubiquity of lasers in current science and technology. This section will therefore be restricted to the description of a few, direct sequels from the studies presented in this thesis.

The investigation of the fiber Bragg grating sensors in harsh environments, such as under intense optical fields, inspired their use in the measurement of the temperature of gases in atmospheric pressure plasmas, where intense electromagnetic fields and high voltage prevent the use of conventional sensors. The same temperature measurement approach used in this thesis was directly applicable to temperature measurements in low temperature and pressure plasmas.

The need of cryogenic-grade sensors in optical cooling motivated the in-depth investigations of the FBGs properties at cryogenic temperatures. Although several approaches had been implemented in the past to increase the sensitivity of FBGs at low temperatures, none had included the thermal expansion coefficient in the prediction of the Bragg wavelength temperature coefficient, therefore theory and experiments did not match. The studies aimed at laser cooling resolved this modeling problem by including the thermal expansion contribution, and also demonstrated the usefulness of bare FBG sensors at low temperature.

A restriction in optical refrigeration by anti-Stokes photoluminescence is the need of materials which present very high quantum efficiency. While this limits the chance of success of a given sample, it conversely impedes that a successful optically-cooled sample have the quantum efficiency outside these strict limits. This thesis uses an optically-cooled sample to assess the accuracy of setup for the measurement of the absolute quantum efficiency setup, where many factors could induce to a measurement error and no reliable reference is available commercially.

Directions for future work

In order to incorporate optical cooling in a complete device, one has to be able to thermally couple the optically-cooled sample to the thermal load. Although other researchers have studied this concept in depth, no simple solution was put forth. Once cooling with glass-ceramics is realized, one should take advantage of its capability of free-geometry formation to test experimentally different monolithic thermal links, which can reject fluorescence but transmit the cooling power,

thus could cool an opaque load. The same flexibility can be used to test different non-resonant cavity shapes to improve pump absorption.

Since the use of FBGs for temperature measurement in laser cooling is demonstrated, there is no fundamental need to use the flexible research-grade interrogators. A dedicated commercial interrogator should be able to perform the same functions, with less training necessary at the user side. Tailored fabrication of FBGs could however still find a niche in optically-cooled fibers, both for increasing pump absorption and to measure the temperature.

Publications

Journal papers

1. R. R. P. Machado, **E. Soares de Lima Filho**, R. C. Dutra, N. R. Barbosa Raposo, R. S. Duarte, G. Luiz G. Soares, *et al.*, "Metabolic Activity Interferometer: A Powerful Tool for Testing Antibiotics," *Journal of Sensors*, vol. 2012, p. 7, 2012.
2. **E. Soares de Lima Filho**, G. Nemova, S. Loranger, and R. Kashyap, "Laser-induced cooling of a Yb:YAG crystal in air at atmospheric pressure," *Optics Express,* vol. 21, pp. 24711-24720, 2013.
3. **E. Soares de Lima Filho**, M. D. Baiad, M. Gagné, and R. Kashyap, "Fiber Bragg gratings for low-temperature measurement," *Optics Express,* vol. 22, pp. 27681-27694, 2014.
4. **E. Soares de Lima Filho**, K. V. Krishnaiah, Y. Ledemi, Y.-J. Yu, Y. Messaddeq, G. Nemova, *et al.*, "Ytterbium-doped glass-ceramics for optical refrigeration," *Optics Express,* vol. 23, pp. 4630-4640, 2015.
5. K. Venkata Krishnaiah, Y. Ledemi, **E. Soares de Lima Filho**, Y. Messaddeq, and R. Kashyap, “Ytterbium doped oxyfluoride glass and glass-ceramic fibers: fabrication and characterization,” (In preparation), 2015.
6. K. Venkata Krishnaiah, **E. Soares de Lima Filho**, Y.-J. Yu, Y. Ledemi, G. Nemova, Y. Messaddeq, and R. Kashyap, “Yb^{3+}-doped oxyfluoride glasses for laser cooling applications,” (In preparation), 2015.

7. J. Lapointe, F. Parent, **E. Soares de Lima Filho**, S. Loranger, and R. Kashyap, “Robust optical sensor for mobile devices: One step waveguide refractive index sensor fabrication using fs laser in Gorilla glass,” (In preparation), 2015.

Technical reviews

1. **E. Soares de Lima Filho**, G. Nemova, M. Saad, S. R. Bowman, and R. Kashyap, "Photoluminescence Measurements for LICOS: Laser Induced Cooling of Solids," *PHOTONS Mag., Revue technique de l'institut canadien pour les innovations en photonique,* vol. 8, pp. 29-32, Fall 2010.
2. R. Kashyap, G. Nemova, **E. Soares de Lima Filho**, and S. Loranger. “How Cool is Laser Refrigeration?, ” *IEEE Photonics Society News 27(2)*, April 2013.
3. E. Barboza Kapish, F. L. Marinho de Oliveira, A. C. de Andrade, F. Kitamura, R. R. P. Machado, D. Farago Jardim, **E. Soares de Lima Filho**, B. Lesche, “Automation of interferometric measurements,” *Principia, Caminhos da Iniciação Científica* v. 17. p. 21-28, 2013.

Conference proceedings

1. **E. Soares de Lima Filho**, M. Gagné, G. Nemova, M. Saad, S. R. Bowman, and R. Kashyap, "Sensing of laser cooling with optical fibres," 7th International Workshop on Fibre Optics and Passive Components, Montréal, 2011.
2. M. Ahlawat, B. Saoudi, **E. Soares de Lima Filho**, M. Wertheimer, and R. Kashyap, "Use of an FBG Sensor for In-situ Temperature Measurements of Gas Dielectric Barrier Discharges," BGPP 2012, Colorado Springs, Colorado, United States, 17-21 June 2012.
3. G. Nemova, **E. Soares de Lima Filho**, S. Loranger, and R. Kashyap, "Laser Cooling With Nanoparticles," Photonics North 2012, Montreal, 6-8 June 2012.
4. S. Loranger, A. Lesage-Landry, **E. Soares de Lima Filho**, G. Nemova, N. O. Dantas, P. C. Morais, *et al.*, "Spectroscopic and life-time measurements of quantum dot doped glass for optical refrigeration: a feasibility study," Photonics West 2013, San Francisco, February 2013.

5. **E. Soares de Lima Filho**, G. Nemova, S. Loranger, and R. Kashyap, "Direct measurement of laser cooling of Yb:YAG crystal at atmospheric pressure using a fiber Bragg grating," Photonics West 2014, San Francisco, 1-6 February 2014.
6. K. Venkata Krishnaiah, Y. Ledemi, **E. Soares de Lima Filho**, Y. Messaddeq, and R. Kashyap, "Nanocrystallization in Yb^{3+}-doped oxyfluoride glasses for laser cooling," Photonics West 2015, San Francisco, 7-12 February 2015.
7. **E. Soares de Lima Filho**, K. Venkata Krishnaiah, Y.-J. Yu, Y. Ledemi, Y. Messaddeq, and R. Kashyap, "Prospects of optical refrigeration in oxyfluoride glasses and glass-ceramics: experiments," Photonics West 2015, San Francisco, 7-12 February 2015.
8. **E. Soares de Lima Filho**, M. Quintanilla, F. Vetrone, G. Nemova, V. K. Kummara, and R. Kashyap, "Characterization of fluoride nanocrystals for optical refrigeration," Photonics West 2015, San Francisco, 7-12 February 2015.
9. K. Venkata Krishnaiah, **E. Soares de Lima Filho**, Y. Ledemi, G. Nemova, Y.-J. Yu, Y. Messaddeq, and R. Kashyap, "Oxyfluoride glass and glass-ceramics for laser induced cooling applications," EXCON 2015, Montréal, 18-22 May 2015 (abstract accepted).

Conference presentations without proceedings

10. (poster) **E. Soares de Lima Filho**, G. Nemova, M. Saad, S. R. Bowman, and R. Kashyap, "LICOS: Laser induced cooling of solids," CIPI Annual General Meeting 2010, Niagara Falls, June 2010.
11. (poster) **E. Soares de Lima Filho**, G. Nemova, M. Saad, S. R. Bowman, and R. Kashyap, "LICOS: Laser induced cooling of solids," CREER Symposium, Montreal, 11 June 2010.
12. (poster) M. Ahlawat, **E. Soares de Lima Filho**, B. Saoudi, M. Wertheimer, and R. Kashyap, "A new optical sensor for in-situ temperature measurements in discharges at atmospheric pressure," Colloque de Plasma-Québec, Montréal, 29-31 May 2012.
13. (talk) G. Nemova, S. Loranger, **E. Soares de Lima Filho** and R. Kashyap, "Quantum dots doped in glass as a new tool for laser cooling of solids," ICOOPMA 2012, Nara, Japan, 3-7 June 2012.

14. (poster) **E. Soares de Lima Filho**, G. Nemova, S. Loranger, and R. Kashyap, "Laser-induced cooling of a Yb^{3+}:YAG at atmospheric pressure," Rencontre annuelle du COPL 2013, Montréal, 16 May 2013.
15. (talk) S. Loranger, **E. Soares de Lima Filho**, G. Nemova, C. Allen, S. Lamarre and R. Kashyap, "Spectroscopy and efficiency of colloidal CdSe quantum dots in liquids for laser cooling," Photonics North 2013, Montréal, 4 June 2013.
16. (poster) S. Loranger, **E. Soares de Lima Filho**, G. Nemova, and R. Kashyap, "Thermal study of laser cooling in rhodamine dye using a Bragg grating," Photonics West 2014, San Francisco, 1-6 February 2014.

Invited talks

1. (Plenary) R. Kashyap, G. Nemova, **E. Soares de Lima Filho**, and S. Loranger, "Cold facts of laser cooling," 16th Canadian Semiconductor Science and Technology Conference, Thunder Bay, Canada, 12-16 August 2013.
2. R. Kashyap, G. Nemova, **E. Soares de Lima Filho**, S. Loranger, Y.-J. Yu, Y. Ledemi, Y. Messaddeq, F. Vetrone, and C. Allen, "Converting hot into cold with light," University of Brazilia, Brazil, 2 December 2013.
3. G. Nemova, S. Loranger, **E. Soares de Lima Filho**, Y.-J. Yu, Y. Ledemi, Y. Messaddeq and R. Kashyap, "Materials and techniques for efficient laser cooling of solids," RADIO 2014, Mauritius, 7-10 April 2014.
4. R. Kashyap, G. Nemova, **E. Soares de Lima Filho**, S. Loranger, K. V. Krishnaiah, Y.-J. Yu, Y. Messaddeq, Y. Ledemi, F. Vetrone, M. Quintanilla and G. Ahluwalia, "Recent advances in proposed techniques for laser cooling of solids," Photonics West 2015, San Francisco, 7-12 February 2015.
5. K. Venkata Krishnaiah, **E. Soares de Lima Filho**, S. Loranger, Y.-J. Yu, G. Nemova, Y. Ledemi, M. Quintanilla, G. Ahluwalia, F. Vetrone, Y. Messaddeq, and R. Kashyap, "Novel rare-earth doped materials for laser cooling," ICMAT 2015, Singapore, 28 June - 3 July 2015.

REFERENCES OF BIBLIOGRAPHY

[1] P. Pringsheim, "Zwei Bemerkungen über den Unterschied von Lumineszenz- und Temperaturstrahlung," *Zeitschrift für Physik A Hadrons and Nuclei*, vol. 57, pp. 739-746, 1929.

[2] L. Landau, "On the thermodynamics of photoluminescence," *J. Phys. USSR*, vol. 10, 1946.

[3] X. L. Ruan, S. C. Rand, and M. Kaviany, "Entropy and efficiency in laser cooling of solids," *Physical Review B*, vol. 75, p. 214304, 2007.

[4] G. Mills and A. Mord, "Performance modeling of optical refrigerators," *Cryogenics*, vol. 46, pp. 176-182, 2005.

[5] G. Nemova and R. Kashyap, "Fiber amplifier with integrated optical cooler," *J. Opt. Soc. Am. B*, vol. 26, pp. 2237-2241, 2009.

[6] E. N. Pettyjohn, "USAF space sensing cryogenic considerations," *Proceedings of SPIE*, vol. 7951, p. 795102, 2011.

[7] M. Zhou, X. Wang, and J. Tan, "Feasibility analysis of radiation balanced laser," *Optics Communications*, vol. 282, pp. 1841-1846, 2009.

[8] S. N. Andrianov and V. V. Samartsev, *Optical Superradiance and Laser Cooling of Solids*, 1st ed. Kazan, 1998.

[9] P. Pringsheim, "Fluorescence and phosphorescence," 1949.

[10] A. Kastler, "Quelques suggestions concernant la production optique et la détection optique d'une inégalité de population des niveaux de quantifigation spatiale des atomes. Application à l'expérience de Stern et Gerlach et à la résonance magnétique," *J. Phys. Radium*, vol. 11, pp. 255-265, 1950.

[11] E. Soares de Lima Filho, G. Nemova , M. Saad, S. R. Bowman, and R. Kashyap, "LICOS: Laser Induced Cooling of Solids," in *CIPI Annual General Meeting*, Niagara Falls (ON) - Canada, 2010.

[12] D. V. Seletskiy, S. D. Melgaard, S. Bigotta, A. Di Lieto, M. Tonelli, and M. Sheik-Bahae, "Laser cooling of solids to cryogenic temperatures," *Nat Photon*, vol. 4, pp. 161-164, 2010.

[13] M. Sheik-Bahae and R. I. Epstein, "Laser cooling of solids," *Laser & Photonics Review*, vol. 3, pp. 67-84, 2009.

[14] G. C. Dousmanis, C. W. Mueller, H. Nelson, and K. G. Petzinger, "Evidence of Refrigerating Action by Means of Photon Emission in Semiconductor Diodes," *Physical Review*, vol. 133, p. A316, 1964.

[15] T. Kushida and J. E. Geusic, "Optical Refrigeration in Nd-Doped Yttrium Aluminum Garnet," *Physical Review Letters*, vol. 21, pp. 1172-1175, 1968.

[16] T. W. Hansch and A. L. Schawlow, "Cooling of gases by laser radiation," *Opt. Commun.*, vol. 13, pp. 68-69, 1975.

[17] N. Djeu and W. T. Whitney, "Laser Cooling by Spontaneous Anti-Stokes Scattering," *Physical Review Letters*, vol. 46, pp. 236-239, 1981.

[18] C. Zander and K. H. Drexhage, "Cooling of a dye solution by anti-stokes fluorescence," in *Proceedings of 5th European Quantum Electronics Conference*, 1994, pp. 9-9.

[19] R. I. Epstein, M. I. Buchwald, B. C. Edwards, T. R. Gosnell, and C. E. Mungan, "Observation of Laser-Induced Fluorescent Cooling of a Solid," *Nature*, vol. 377, pp. 500-503, 1995.

[20] S. R. Bowman and C. E. Mungan, "New materials for optical cooling," *Appl. Phys. B*, vol. 71, pp. 807-811, 2000.

[21] J. Thiede, J. Distel, S. R. Greenfield, and R. I. Epstein, "Cooling to 208 K by optical refrigeration," *Applied Physics Letters*, vol. 86, pp. 154107-3, 2005.

[22] S. Bigotta, D. Parisi, L. Bonelli, A. Toncelli, A. D. Lieto, and M. Tonelli, "Laser cooling of Yb^{3+}-doped BaY_2F_8 single crystal," *Optical Materials*, vol. 28, pp. 1321-1324, 2006.

[23] S. Bigotta, "Spectroscopic and laser cooling results on Yb^{3+}-doped BaY_2F_8 single crystal," *J. Appl. Phys.*, vol. 100, p. 013109, 2006.

[24] S. Bigotta, "Laser cooling of solids: new results with single fluoride crystals," *Nuovo Cimento B Serie*, vol. 122, p. 685694, 2007.

[25] V. S. Denis, D. M. Seth, B. Stefano, L. Alberto Di, T. Mauro, I. E. Richard, *et al.*, "Demonstration of an Optical Cryocooler," in *International Quantum Electronics Conference*, 2009, p. IPDA9.

[26] D. V. Seletskiy, S. D. Melgaard, R. I. Epstein, A. Di Lieto, M. Tonelli, and M. Sheik-Bahae, "Local laser cooling of Yb:YLF to 110 K," *Opt. Express*, vol. 19, pp. 18229-18236, 2011.

[27] S. D. Melgaard, D. V. Seletskiy, A. Di Lieto, M. Tonelli, and M. Sheik-Bahae, "High sensitivity optical refrigeration spectroscopy: Local cooling of Yb:YLF crystal to 110 K," in *Conference on Lasers and Electro-Optics (CLEO)*, 2011, pp. 1-2.

[28] D. Seletskiy, "Fast differential luminescence thermometry," *Proc. SPIE*, vol. 7228, p. 72280K, 2009.

[29] S. Melgaard, D. Seletskiy, A. Albrecht, and M. Sheik-Bahae. (2015) First solid-state cooling below 100K. *Optical Design & Engineering.* 1-2.

[30] D. V. Seletskiy, R. I. Epstein, and M. Sheik-Bahae, "Progress toward sub-100 Kelvin operation of an optical cryocooler," presented at the Laser Refrigeration of Solids IV, San Francisco, California, USA, 2011.

[31] E. Soares de Lima Filho, M. Gagné, G. Nemova , M. Saad, S. R. Bowman, and R. Kashyap, "Sensing of laser cooling with optical fibres," presented at the 7th International Workshop on Fibre Optics and Passive Components, Montréal, 2011.

[32] E. Soares de Lima Filho, G. Nemova, M. Saad, S. R. Bowman, and R. Kashyap, "Photoluminescence Measurements for LICOS: Laser Induced Cooling of Solids," *PHOTONS Mag., Revue technique de l'institut canadien pour les innovations en photonique*, vol. 8, pp. 29-32, 2010.

[33] E. Soares de Lima Filho, G. Nemova, S. Loranger, and R. Kashyap, "Direct measurement of laser cooling of Yb:YAG crystal at atmospheric pressure using a fiber Bragg grating," in *Proc. SPIE 9000*, 2014, pp. 90000I-90000I-11.

[34] E. Soares de Lima Filho, G. Nemova, S. Loranger, and R. Kashyap, "Laser-induced cooling of a Yb:YAG crystal in air at atmospheric pressure," *Optics Express,* vol. 21, pp. 24711-24720, 2013.

[35] B. Zhong, Y. Jia, L. Chen, Y. Deng, Y. Chen, and J. Yin, "Cavity-enhanced laser cooling for Yb^{3+}-doped fluoride crystal using a low-power diode laser," *Journal of the Optical Society of America B,* vol. 31, pp. 2116-2120, 2014.

[36] B. Zhong, J. Yin, Y. Jia, L. Chen, Y. Hang, and J. Yin, "Laser cooling of Yb^{3+}-doped $LuLiF_4$ crystal," *Optics Letters,* vol. 39, pp. 2747-2750, 2014.

[37] E. E. Brown, U. Hömmerich, E. Kumi-Barimah, A. Bluiett, and S. B. Trivedi, "Comparative spectroscopic studies of Ho:KPb_2Cl_5, Ho:KPb_2Br_2, and Ho:YAG for 2 μm laser cooling applications," in *Laser Refrigeration of Solids VIII*, 2015, pp. 93800O-93800O-7.

[38] S. R. Bowman, "Lasers without internal heat generation," *Quantum Electronics, IEEE Journal of,* vol. 35, pp. 115-122, 1999.

[39] S. R. Bowman and C. E. Mungan, "New materials for optical cooling," *Applied Physics B: Lasers and Optics,* vol. 71, pp. 807-811, 2000.

[40] S. N. Andrianov and V. V. Samartsev, "Solid state lasers with internal laser refrigeration effect," *Proc. SPIE 4605-31,* pp. 208-213, 2001.

[41] G. Nemova and R. Kashyap, "Athermal continuous-wave fiber amplifier," *Optics Communications,* vol. 282, pp. 2571-2575, 2009.

[42] G. Nemova and R. Kashyap, *High-power fiber lasers with integrated rare-earth optical cooler* vol. 7614: SPIE, 2010.

[43] G. Nemova and R. Kashyap, "Yb^{3+}-doped fiber laser with integrated optical cooler," in *Laser Technology for Defense and Security VI*, Orlando, FL, USA, 2010.

[44] G. Nemova and R. Kashyap, "Optimization of the dimensions of an Yb^{3+}:ZBLANP optical fiber sample for laser cooling of solids," *Opt. Lett.,* vol. 33, pp. 2218-2220, 2008.

[45] G. Nemova and R. Kashyap, "Raman Fiber Amplifier With Integrated Cooler," *Journal of Lightwave Technology,* vol. 27, pp. 5597-5601, 2009.

[46] J. N. W. Bowman S R, Feldman B & O'Connor S, "Demonstration of a radiatively cooled laser," in *Conf. Lasers Electro-Opt.*, Long Beach, CA, 2002.

[47] S. R. Bowman, S. P. O'Connor, S. Biswal, N. J. Condon, and A. Rosenberg, "Minimizing Heat Generation in Solid-State Lasers," *IEEE Journal of Quantum Electronics,* vol. 46, pp. 1076-1085, 2010.

[48] M. Sheik-Bahae and R. I. Epstein, "Optical refrigeration," *Nature Photon.,* vol. 12, pp. 693-699, 2007.

[49] M. Sheik-Bahae and R. I. Epstein, "Can laser light cool semiconductors?," *Phys. Rev. Lett.,* vol. 92, p. 247403, 2004.

[50] H. Gauck, T. H. Gfroerer, M. J. Renn, E. A. Cornell, and K. A. Bertness, "External radiative quantum efficiency of 96% from a GaAs/GaInP heterostructure," *Appl. Phys. A,* vol. 64, pp. 143-147, 1997.

[51] E. Finkeissen, M. Potemski, P. Wyder, L. Vina, and G. Weimann, "Cooling of a semiconductor by luminescence up-conversion," *Appl. Phys. Lett.*, vol. 75, pp. 1258-1260, 1999.

[52] T. H. Gfroerer, E. A. Cornell, and M. W. Wanlass, "Efficient directional spontaneous emission from an InGaAs/InP heterostructure with an integral parabolic reflector," *Journal of Applied Physics*, vol. 84, pp. 5360-5362, 1998.

[53] B. Imangholi, M. P. Hasselbeck, M. Sheik-Bahae, R. I. Epstein, and S. Kurtz, "Effects of epitaxial lift-off on interface recombination and laser cooling in GaInP⁄ GaAs heterostructures," *Applied Physics Letters*, vol. 86, p. 081104, 2005.

[54] S. Eshlaghi, W. Worthoff, A. D. Wieck, and D. Suter, "Luminescence upconversion in GaAs quantum wells," *Physical Review B*, vol. 77, p. 245317, 2008.

[55] X. L. Ruan and M. Kaviany, "Advances in Laser Cooling of Solids," *Journal of Heat Transfer*, vol. 129, pp. 3-10, 2007.

[56] D. Li, J. Zhang, X. Wang, B. Huang, and Q. Xiong, "Solid-State Semiconductor Optical Cryocooler Based on CdS Nanobelts," *Nano letters*, vol. 14, pp. 4724-4728, 2014.

[57] J. Zhang, D. Li, R. Chen, and Q. Xiong, "Laser cooling of a semiconductor by 40 kelvin," *Nature*, vol. 493, pp. 504-508, 2013.

[58] D. V. Seletskiy, S. D. Melgaard, A. Di Lieto, M. Tonelli, and M. Sheik-Bahae, "Laser cooling of a semiconductor load to 165 K," *Optics Express*, vol. 18, pp. 18061-18066, 2010.

[59] W. G. Scheibenzuber and U. T. Schwarz, "Fast self-heating in GaN-based laser diodes," *Applied Physics Letters*, vol. 98, p. 181110, 2011.

[60] M. Fadhali, J. Zainal, Y. Munajat, J. Ali, and R. A. Rahman, "Efficient coupling and relaxed alignment tolerances in pigtailing of a laser diode using dual ball lenses," *Optik - International Journal for Light and Electron Optics*, vol. 120, pp. 384-389, 2009.

[61] R. Dong, J. Zhang, T. Zhang, and C. Xie, "Quantum anticorrelation between orthogonal-polarization modes of laser diode at cryogenic temperature," *Optics Communications*, vol. 201, pp. 105-112, 2002.

[62] K. J. Linden, W. R. Neal, T. Ta, R. Feeler, and S. Ross, "Kilowatt CW Cryogenic 940-nm Diode Lasers," *Photonics Technology Letters, IEEE*, vol. 22, pp. 1452-1454, 2010.

[63] S. Andrianov and V. Samartsev, "Optical superradiation and laser cooling," *Laser Physics*, vol. 7, pp. 314-317, 1997.

[64] S. N. Andrianov, "Experimental and theorectical studies of laser cooling of condensed media," *J. Opt. Technol.*, vol. 69, pp. 864-870, 2002.

[65] G. Nemova and R. Kashyap, "Alternative technique for laser cooling with superradiance," *Physical Review A*, vol. 83, p. 013404, 2011.

[66] G. Nemova and R. Kashyap, "Breaking the low phonon energy barrier for laser cooling in rare-earth doped hosts," San Francisco, California, USA, 2011, pp. 79510G-9.

[67] S. Petrushkin and V. Samartsev, "Advances of laser refrigeration in solids," *Laser Physics*, vol. 20, pp. 38-46, 2010.

[68] S. V. Petrushkin and V. V. Samartsev, "Superradiance Regime of Laser Cooling of Crystals and Glasses Doped with Rare-Earth Ions," *Laser Physics,* vol. 11, pp. 948-956, 2001.

[69] S. V. Petrushkin and V. V. Samartsev, *Laser cooling of solids*. Cambridge; Oxford; Boca Raton: Cambridge International Science Pub. Ltd. ; In association with Woodhead Pub. Ltd. ; CRC Press, 2009.

[70] G.-Z. Dong, X.-L. Zhang, and J.-H. Cui, "Double-pulse excitation scheme for laser cooling of solids in the superradiance regime," *Journal of the Optical Society of America B,* vol. 32, pp. 324-330, 2015.

[71] E. Bashkirov, "Superradiance regime of laser cooling in extended solids," *Physics of Particles and Nuclei Letters,* vol. 4, pp. 169-172, 2007.

[72] K. Koshino, "Theory of resonance fluorescence from a solid-state cavity QED system: Effects of pure dephasing," *Physical Review A,* vol. 84, p. 033824, 2011.

[73] A. Sawadsky, H. Kaufer, R. M. Nia, S. P. Tarabrin, F. Y. Khalili, K. Hammerer, *et al.*, "Observation of Generalized Optomechanical Coupling and Cooling on Cavity Resonance," *Physical Review Letters,* vol. 114, p. 043601, 2015.

[74] V. K. Malyutenko, V. V. Bogatyrenko, and O. Y. Malyutenko, "Radiative cooling of bulk Si by optical down-conversion," *J Appl Phys Journal of Applied Physics,* vol. 108, 2010.

[75] V. K. Malyutenko, V. V. Bogatyrenko, and O. Y. Malyutenko, "Radiative cooling by light down conversion of InGaN light emitting diode bonded to a Si wafer," *Applied Physics Letters,* vol. 102, pp. 241102-241102-3, 2013.

[76] V. K. Malyutenko, "Light up conversion versus light down conversion in radiative cooling of semiconductors," in *Proc. SPIE 9000,* 2014, pp. 90000P-90000P-8.

[77] V. K. Malyutenko, V. V. Bogatyrenko, and O. Y. Malyutenko, "Radiative cooling of bulk silicon by incoherent light pump," *Applied Physics Letters,* vol. 103, pp. -, 2013.

[78] M. Tonelli, A. Dilieto, and A. Volpi, "A novel approach for solid-state cryocooler (unpublished)," Laser Refrigeration of Solids VIII, 2015.

[79] P. B. Roder, B. Smith, X. Zhou, M. J. Crane, and P. J. Pauzauskie, "Laser-refrigeration of rare-earth-doped nanocrystals in water," in *Laser Refrigeration of Solids VIII*, 2015, pp. 938007-938007-9.

[80] A. J. Garcia-Adeva, R. Balda, M. Al Saleh, and J. Fernandez, "Local internal and bulk optical cooling in Nd-doped crystals and nanocrystalline powders," in *Laser Refrigeration of Solids III*, 2010, pp. 76140A-76140A-12.

[81] A. J. Garcia-Adeva, R. Balda, M. Al Saleh, S. Garcia-Revilla, and J. Fernandez, "Local internal and bulk optical cooling in Nd-doped crystals and nanocrystalline powders revisited," in *Laser Refrigeration of Solids IV*, 2011, pp. 795106-795106-10.

[82] A. J. Garcia-Adeva, R. Balda, M. Al Saleh, S. Garcia-Revilla, D. Sola, and J. Fernández, "Optical cooling of Nd-doped solids," 2012, pp. 827502-827502-14.

[83] J. Fernández, R. Balda, M. Barredo-Zuriarrain, O. Merdrignac-Conanec, N. Hakmeh, S. García-Revilla, *et al.*, "Spectroscopic and thermal study of Er-doped oxysulfide crystal powders," in *Laser Refrigeration of Solids VIII*, 2015, pp. 93800A-93800A-10.

[84] E. Soares de Lima Filho, M. Quintanilla, F. Vetrone, G. Nemova, V. K. Kummara, and R. Kashyap, "Characterization of fluoride nanocrystals for optical refrigeration," in *Laser Refrigeration of Solids VIII*, 2015, pp. 93800Q-93800Q-10.

[85] E. Soares de Lima Filho, K. V. Krishnaiah, Y. Ledemi, Y.-J. Yu, Y. Messaddeq, G. Nemova, *et al.*, "Ytterbium-doped glass-ceramics for optical refrigeration," *Optics Express*, vol. 23, pp. 4630-4640, 2015.

[86] K. Venkata Krishnaiah, Y. Ledemi, E. Soares de Lima Filho, Y. Messaddeq, and R. Kashyap, "Nanocrystallization in Yb^{3+}-doped oxyfluoride glasses for laser cooling," in *Laser Refrigeration of Solids VIII*, 2015, pp. 93800P-93800P-8.

[87] E. Soares de Lima Filho, K. Venkata Krishnaiah, Y.-J. Yu, Y. Ledemi, Y. Messaddeq, and R. Kashyap, "Prospects of optical refrigeration in oxyfluoride glasses and glass-ceramics: experiments," in *Laser Refrigeration of Solids VIII*, 2015, pp. 93800R-93800R-9.

[88] J. Tauc, "The share of thermal energy taken from the surroundings in the electro-luminescent energy radiated from ap-n junction," *Cechoslovackij fiziceskij zurnal*, vol. 7, pp. 275-276, 1957.

[89] R. Kashyap and G. Nemova, "Laser induced cooling of solids," *physica status solidi (c)*, vol. 8, pp. 144-150, 2011.

[90] J. M. William, "Optical and Electronic Properties of Rare Earth Ions in Glasses," in *Rare-Earth-Doped Fiber Lasers and Amplifiers, Revised and Expanded*, ed: CRC Press, 2001.

[91] Y. Y. Kalisky, *The physics and engineering of solid state lasers* vol. 71: SPIE Press, 2006.

[92] B. Walsh, "Judd-Ofelt theory: principles and practices," in *Advances in Spectroscopy for Lasers and Sensing*, B. Bartolo and O. Forte, Eds., ed: Springer Netherlands, 2006, pp. 403-433.

[93] E. U. Condon and G. H. Shortley, *The theory of atomic spectra*: Cambridge University Press, 1951.

[94] M. P. Hehlen, "Crystal-field effects in fluoride crystals for optical refrigeration," 2010, pp. 761404-761404-12.

[95] F. Auzel, "A relationship for crystal field strength along the lanthanide series; application to the prediction of the ($^2F_{7/2}$) Yb^{3+} maximum splitting," *Optical Materials*, vol. 19, pp. 89-94, 2002.

[96] F. Auzel, "On the maximum splitting of the (2F7/2) ground state in Yb3+-doped solid state laser materials," *Journal of Luminescence*, vol. 93, pp. 129-135, 2001.

[97] R. P. Leavitt and C. A. Morrison, "Crystal-field analysis of triply ionized rare earth ions in lanthanum trifluoride. II. Intensity calculations," *The Journal of Chemical Physics*, vol. 73, pp. 749-757, 1980.

[98] J. H. V. Vleck, "The Puzzle of Rare-earth Spectra in Solids," *The Journal of Physical Chemistry*, vol. 41, pp. 67-80, 1937.

[99] S. Tanabe, T. Ohyagi, N. Soga, and T. Hanada, "Compositional dependence of Judd-Ofelt parameters of Er^{3+} ions in alkali-metal borate glasses," *Physical Review B*, vol. 46, pp. 3305-3310, 1992.

[100] J. M. F. van Dijk and M. F. H. Schuurmans, "On the nonradiative and radiative decay rates and a modified exponential energy gap law for 4f–4f transitions in rare-earth ions," *The Journal of Chemical Physics,* vol. 78, pp. 5317-5323, 1983.

[101] M. P. Hehlen, W. L. Boncher, S. D. Melgaard, M. W. Blair, R. A. Jackson, T. E. Littleford, *et al.*, "Preparation of high-purity LiF, YF_3, and YbF_3 for laser refrigeration," in *Laser Refrigeration of Solids VII*, 2014, pp. 900004-900004-11.

[102] R. I. Epstein and M. Sheik-Bahae, *Optical refrigeration : science and applications of laser cooling of solids*. Weinheim: Wiley-VCH, 2009.

[103] G. C. Righini and M. Ferrari, "Photoluminescence of rare-earth-doped glasses," *Rivista del Nuovo Cimento,* vol. 28, 2005.

[104] D. W. Hewak, J. A. Medeiros Neto, B. N. Samson, J. Wang, H. J. Tate, A. Pearson, *et al.*, "Spectroscopy of Pr^{3+}-doped low-phonon-energy glasses based on halides and sulfides," in *Fiber Laser Sources and Amplifiers V*, 1994, pp. 102-117.

[105] S. Aasland, M.-A. Einarsrud, T. Grande, and P. F. McMillan, "Spectroscopic investigations of fluorozirconate glasses in the ternary systems ZrF_4-BaF_2-AF (A= Na, Li)," *The Journal of Physical Chemistry,* vol. 100, pp. 5457-5463, 1996.

[106] M. Dejneka, E. Snitzer, and R. E. Riman, "Blue, green and red fluorescence and energy transfer of Eu^{3+} in fluoride glasses," *Journal of Luminescence,* vol. 65, pp. 227-245, 1995.

[107] R. S. Deol, D. W. Hewak, S. Jordery, A. Jha, M. Poulain, M. D. Baró, *et al.*, "Improved fluoride glasses for 1.3 μm optical amplifiers," *Journal of Non-Crystalline Solids,* vol. 161, pp. 257-261, 1993.

[108] M. Voda, M. Al-Saleh, G. Lobera, R. Balda, and J. Fernández, "Crystal growth of rare-earth-doped ternary potassium lead chloride single crystals by the Bridgman method," *Optical Materials,* vol. 26, pp. 359-363, 2004.

[109] A. Ferrier, M. Velázquez, J.-L. Doualan, and R. Moncorgé, "Energy level structure and excited-state absorption properties of Er^{3+}-doped KPb_2Cl_5," *J. Opt. Soc. Am. B,* vol. 24, pp. 2526-2536, 2007.

[110] H. Scheife, G. Huber, E. Heumann, S. Bär, and E. Osiac, "Advances in up-conversion lasers based on Er^{3+} and Pr^{3+}," *Optical Materials,* vol. 26, pp. 365-374, 2004.

[111] S. Salaün, A. Bulou, M. Rousseau, B. Hennion, and J. Y. Gesland, "Lattice dynamics of fluoride scheelites: II. Inelastic neutron scattering in $LiYF_4$ and modelization," *Journal of Physics: Condensed Matter,* vol. 9, p. 6957, 1997.

[112] V. K. Tikhomirov, G. Adamo, A. E. Nikolaenko, V. D. Rodriguez, P. Gredin, M. Mortier, *et al.*, "Cathodo- and photoluminescence in Yb^{3+}-Er^{3+} co-doped PbF_2 nanoparticles," *Optics Express,* vol. 18, pp. 8836-8846, 2010.

[113] G. A. Slack, D. W. Oliver, R. M. Chrenko, and S. Roberts, "Optical Absorption of $Y_3Al_5O_{12}$ from 10 to 55000 cm Wave Numbers," *Physical Review,* vol. 177, pp. 1308-1314, 1969.

[114] D. C. Brown and V. A. Vitali, "Yb:YAG Kinetics Model Including Saturation and Power Conservation," *IEEE Journal of Quantum Electronics,* vol. 47, pp. 3-12, 2011.

[115] M. Bahrami, J. R. Culham, M. M. Yovanovich, and G. E. Schneider, "Thermal Contact Resistance of Nonconforming Rough Surfaces, Part 1: Contact Mechanics Model," *Journal of Thermophysics and Heat Transfer,* vol. 18, pp. 209-217, 2004.

[116] S. Oke, A. Oyekunle, T. Salau, A. Adegbemile, and K. Lawal, "Estimation of thermal contact resistance in metal-plastic interface of semiconducting electronic devices," *Int. J. Nanoelectronics and Materials,* vol. 2, pp. 23-39, 2009.

[117] D. C. Brown and H. J. Hoffman, "Thermal, stress, and thermo-optic effects in high average power double-clad silica fiber lasers," *IEEE Journal of Quantum Electronics,* vol. 37, pp. 207-217, 2001.

[118] R. I. Epstein, M. P. Hehlen, M. Sheik-Bahae, and S. D. Melgaard, "Optical cryocoolers for sensors and electronics," 2014, pp. 90702K-90702K-10.

[119] A. Rayner, "Laser Cooling of Solids," PhD, Department of Physics, University of Queensland, 2002.

[120] R. Siegel and J. R. Howell, *Thermal Radiation Heat Tranfer*: Hemisphere Publishing Corporation / McGraw-Hill Book Company, 1981.

[121] R. Gardon, "The Emissivity of Transparent Materials," *Journal of the American Ceramic Society,* vol. 39, pp. 278-285, 1956.

[122] R. I. Epstein, J. J. Brown, B. C. Edwards, and A. Gibbs, "Measurements of optical refrigeration in ytterbium-doped crystals," *Journal of Applied Physics,* vol. 90, pp. 4815-4819, 2001.

[123] S. Chénais, F. Druon, S. Forget, F. Balembois, and P. Georges, "On thermal effects in solid-state lasers: The case of ytterbium-doped materials," *Progress in Quantum Electronics,* vol. 30, pp. 89-153, 2006.

[124] T. Y. Fan, "Heat generation in Nd:YAG and Yb:YAG," *Quantum Electronics, IEEE Journal of,* vol. 29, pp. 1457-1459, 1993.

[125] G. G. Demirkhanyan, "Intensities of inter-Stark transitions in YAG-Yb^{3+} crystals," *Laser Physics,* vol. 16, pp. 1054-1057, 2006.

[126] C. Würth, J. Pauli, C. Lochmann, M. Spieles, and U. Resch-Genger, "Integrating Sphere Setup for the Traceable Measurement of Absolute Photoluminescence Quantum Yields in the Near Infrared," *Analytical Chemistry,* vol. 84, pp. 1345-1352, 2011.

[127] J. C. de Mello, H. F. Wittmann, and R. H. Friend, "An improved experimental determination of external photoluminescence quantum efficiency," *Advanced Materials,* vol. 9, pp. 230-232, 1997.

[128] C. Würth, D. Geißler, T. Behnke, M. Kaiser, and U. Resch-Genger, "Critical review of the determination of photoluminescence quantum yields of luminescent reporters," *Analytical and Bioanalytical Chemistry,* vol. 407, pp. 59-78, 2015.

[129] O. E. Semonin, J. C. Johnson, J. M. Luther, A. G. Midgett, A. J. Nozik, and M. C. Beard, "Absolute Photoluminescence Quantum Yields of IR-26 Dye, PbS, and PbSe Quantum Dots," *The Journal of Physical Chemistry Letters,* vol. 1, pp. 2445-2450, 2010.

[130] D. Jaque and F. Vetrone, "Luminescence nanothermometry," *Nanoscale,* vol. 4, pp. 4301-4326, 2012.

[131] F. Vetrone, R. Naccache, A. Zamarrón, A. Juarranz de la Fuente, F. Sanz-Rodríguez, L. Martinez Maestro, *et al.*, "Temperature Sensing Using Fluorescent Nanothermometers," *ACS Nano,* vol. 4, pp. 3254-3258, 2010.

[132] W. Xu, X. Gao, L. Zheng, Z. Zhang, and W. Cao, "Short-wavelength upconversion emissions in Ho^{3+}/Yb^{3+} codoped glass ceramic and the optical thermometry behavior," *Optics Express,* vol. 20, pp. 18127-18137, 2012.

[133] C. E. Mungan, M. I. Buchwald, B. C. Edwards, R. I. Epstein, and T. R. Gosnell, "Laser cooling of a solid by 16 K starting from room temperature," *Phys. Rev. Lett.,* vol. 78, pp. 1030-1033, 1997.

[134] X. Luo, M. D. Eisaman, and T. R. Gosnell, "Laser cooling of a solid by 21K starting from room temperature," *Opt. Lett.,* vol. 23, pp. 639-641, 1998.

[135] T. R. Gosnell, "Laser cooling of a solid by 65K starting from room temperature," *Opt. Lett.,* vol. 24, pp. 1041-1043, 1999.

[136] W. M. Patterson, "Model of laser-induced temperature changes in solid-state optical refrigerators," *J. Appl. Phys.,* vol. 107, p. 063108, 2010.

[137] W. M. Patterson, D. V. Seletskiy, M. Sheik-Bahae, R. I. Epstein, and M. P. Hehlen, "Measurement of solid-state optical refrigeration by two-band differential luminescence thermometry," *J. Opt. Soc. Am. B,* vol. 27, pp. 611-618, 2010.

[138] W. M. Patterson, M. P. Hehlen, M. Sheik-Bahae, and R. I. Epstein, "Synthesis and evaluation of ultra-pure rare-earth-doped glass for laser refrigeration," in *Proc. SPIE 7228*, 2009, pp. 72280C-72280C-10.

[139] S. D. Melgaard, D. V. Seletskiy, A. Di Lieto, M. Tonelli, and M. Sheik-Bahae, "Optical refrigeration progress: cooling below NIST cryogenic temperature of 123K," in *Proc. SPIE 8638*, 2013, pp. 863804-863804.

[140] S. D. Melgaard, D. V. Seletskiy, A. Di Lieto, M. Tonelli, and M. Sheik-Bahae, "Optical refrigeration to 119K, below National Institute of Standards and Technology cryogenic temperature," *Opt. Lett.,* vol. 38, pp. 1588-1590, 2013.

[141] M. Ghasemkhani, A. R. Albrecht, S. D. Melgaard, D. V. Seletskiy, J. G. Cederberg, and M. Sheik-Bahae, "Intra-cavity cryogenic optical refrigeration using high power vertical external-cavity surface-emitting lasers (VECSELs)," *Optics Express,* vol. 22, pp. 16232-16240, 2014.

[142] M. P. Hehlen, R. I. Epstein, and W. M. Patterson, "Synthesis of ultrapure ZBLAN glass for laser refrigeration," in *Proc. SPIE 6970*, 2008, pp. 69070A-11.

[143] M. P. Hehlen, M. Sheik-Bahae, R. I. Epstein, S. D. Melgaard, and D. V. Seletskiy, "Materials for Optical Cryocoolers," *Journal of Materials Chemistry C,* vol. 1, pp. 7471-7478, 2013.

[144] A. C. Boccara, W. Jackson, N. M. Amer, and D. Fournier, "Sensitive photothermal deflection technique for measuring absorption in optically thin media," *Optics Letters,* vol. 5, pp. 377-379, 1980.

[145] C. E. Mungan, M. I. Buchwald, B. C. Edwards, R. I. Epstein, and T. R. Gosnell, "Internal laser cooling of Yb^{3+}-doped glass measured between 100 and 300 K," *Applied Physics Letters*, vol. 71, pp. 1458-1460, 1997.

[146] D. V. Seletskiy, "Cooling of Yb:YLF using cavity enhanced resonant absorption," *Proc. SPIE*, vol. 6907, p. 6907B, 2008.

[147] M. Sheik-bahae, A. A. Said, and E. W. Van Stryland, "High-sensitivity, single-beam n2 measurements," *Optics Letters*, vol. 14, pp. 955-957, 1989.

[148] M. Sheik-Bahae, A. A. Said, T. H. Wei, D. J. Hagan, and E. W. Van Stryland, "Sensitive measurement of optical nonlinearities using a single beam," *Quantum Electronics, IEEE Journal of*, vol. 26, pp. 760-769, 1990.

[149] N. Giannini, J. R. Silva, C. Wang, A. R. Albrecht, S. D. Melgaard, and M. Sheik-Bahae, "High sensitivity background absorption measurements in semiconductors," in *Laser Refrigeration of Solids VIII*, 2015, pp. 93800F-93800F-8.

[150] J. Shen, M. L. Baesso, and R. D. Snook, "Three-dimensional model for cw laser-induced mode-mismatched dual-beam thermal lens spectrometry and time-resolved measurements of thin-film samples," *Journal of Applied Physics*, vol. 75, pp. 3738-3748, 1994.

[151] X. Peng, A. Asundi, Y. Chen, and Z. Xiong, "Study of the mechanical properties of Nd:YVO_4 crystal by use of laser interferometry and finite-element analysis," *Applied Optics*, vol. 40, pp. 1396-1403, 2001.

[152] C. Jacinto, D. N. Messias, A. A. Andrade, S. M. Lima, M. L. Baesso, and T. Catunda, "Thermal lens and Z-scan measurements: Thermal and optical properties of laser glasses – A review," *Journal of Non-Crystalline Solids*, vol. 352, pp. 3582-3597, 2006.

[153] J. R. Silva, L. C. Malacarne, M. L. Baesso, S. M. Lima, L. H. C. Andrade, C. Jacinto, *et al.*, "Modeling the population lens effect in thermal lens spectrometry," *Opt. Lett.*, vol. 38, pp. 422-424, 2013.

[154] J. Silva, L. Andrade, S. Lima, M. Hehlen, Y. Guyot, A. Medina, *et al.*, "Laser-induced lensing effects in solid-state optical refrigerators," *Applied Physics Letters*, vol. 102, p. 141910, 2013.

[155] R. R. P. Machado, E. Soares de Lima Filho, D. F. Jardim, M. A. A. Ferreira, C. G. de Faria, R. S. Duarte, *et al.*, "Metabolic activity interferometer: description and calibration of an interferometric method to measure growth of mycobacteria," *European Biophysics Journal*, vol. 38, pp. 111-119, 2008.

[156] C. W. Hoyt, "Advances in laser cooling of thulium-doped glass," *J. Opt. Soc. Am. B*, vol. 20, pp. 1066-1074, 2003.

[157] C. Farley III and B. R. Bommareddi, "Mach-Zehnder interferometric measurement of laser heating/cooling in Yb^{3+}: YAG," 2011, pp. 79510I-79510I-8.

[158] I. I. I. C. W. Farley and B. R. Reddy, "Interferometric measurement of laser heating in praseodymium-doped YAG crystal," *Appl. Opt.*, vol. 50, pp. 526-531, 2011.

[159] N. J. Condon, S. R. Bowman, S. P. O'Connor, R. S. Quimby, and C. E. Mungan, "Optical cooling in Er^{3+}:KPb_2Cl_5," *Opt. Express*, vol. 17, pp. 5466-5472, 2009.

[160] S. S. Sih and J. W. Barlow, "The Prediction of the Emissivity and Thermal Conductivity of Powder Beds," *Particulate Science and Technology,* vol. 22, pp. 427-440, 2004.

[161] C. W. Hoyt, M. Sheik-Bahae, R. I. Epstein, B. C. Edwards, and J. E. Anderson, "Observation of anti-Stokes fluorescent cooling in thulium-doped glass," *Phys. Rev. Lett.,* vol. 85, pp. 3600-3603, 2000.

[162] W. Patterson, "Anti-Stokes luminescence cooling of Tm^{3+} doped BaY_2F_8," *Opt. Express,* vol. 16, pp. 1704-1710, 2008.

[163] A. Di Lieto, A. Sottile, A. Volpi, Z. Zhang, D. V. Seletskiy, and M. Tonelli, "Influence of other rare earth ions on the optical refrigeration efficiency in Yb:YLF crystals," *Optics Express,* vol. 22, pp. 28572-28583, 2014.

[164] A. Di Lieto, A. Sottilea, A. Volpia, Z. Zhanga, and M. Tonellia, "Effect of impurities on cooling efficiency in fluoride crystals," in *Proc. of SPIE Vol*, 2014, pp. 900003-1.

[165] J. V. Guiheen, "Ytterbium(3+) and thulium(3+) doped fluoroaluminate glasses for anti-Stokes cooling," 3134843 Ph.D., Rutgers The State University of New Jersey - New Brunswick, Ann Arbor, 2004.

[166] D. Seletskiy, M. P. Hasselbeck, M. Sheik-Bahae, and R. I. Epstein, "Laser cooling using cavity enhanced pump absorption," in *Proc. SPIE 6461*, San Jose, CA, USA, 2007, pp. 646104-8.

[167] D. V. Seletskiy, M. P. Hasselbeck, and M. Sheik-Bahae, "Resonant cavity-enhanced absorption for optical refrigeration," *Applied Physics Letters,* vol. 96, p. 181106, 2010.

[168] A. Einstein, "Über die von der molekularkinetischen Theorie der Wärme geforderte Bewegung von in ruhenden Flüssigkeiten suspendierten Teilchen," *Annalen der physik,* vol. 322, pp. 549-560, 1905.

[169] J. Perrin, "Mouvement brownien et réalité moléculaire," in *Annales de Chimie et de Physique*, 1909, pp. 5-104.

[170] R. Newburgh, J. Peidle, and W. Rueckner, "Einstein, Perrin, and the reality of atoms: 1905 revisited," *American Journal of Physics,* vol. 74, pp. 478-481, 2006.

[171] J. S. Park, C. K. Choi, and K. D. Kihm, "Temperature measurement for a nanoparticle suspension by detecting the Brownian motion using optical serial sectioning microscopy (OSSM)," *Measurement Science and Technology,* vol. 16, p. 1418, 2005.

[172] R. Radünz, D. Rings, K. Kroy, and F. Cichos, "Hot Brownian Particles and Photothermal Correlation Spectroscopy," *The Journal of Physical Chemistry A,* vol. 113, pp. 1674-1677, 2009.

[173] K. Chung, J. K. Cho, E. S. Park, V. Breedveld, and H. Lu, "Three-Dimensional in Situ Temperature Measurement in Microsystems Using Brownian Motion of Nanoparticles," *Analytical Chemistry,* vol. 81, pp. 991-999, 2009.

[174] G. Falasco, M. V. Gnann, D. Rings, and K. Kroy, "Effective temperatures of hot Brownian motion," *Physical Review E,* vol. 90, p. 032131, 2014.

[175] MillenJ, DeesuwanT, BarkerP, and AndersJ, "Nanoscale temperature measurements using non-equilibrium Brownian dynamics of a levitated nanosphere," *Nat Nano,* vol. 9, pp. 425-429, 2014.

[176] B. C. Edwards, J. E. Anderson, R. I. Epstein, G. L. Mills, and A. J. Mord, "Demonstration of a solid-state optical cooler: An approach to cryogenic refrigeration," *Journal of Applied Physics,* vol. 86, pp. 6489-6493, 1999.

[177] J. Thiede, J. Distel, S. R. Greenfield, and R. I. Epstein, "Cooling to 208 K by optical refrigeration," *Applied Physics Letters,* vol. 86, 2005.

[178] A. Rayner, N. R. Heckenberg, and H. Rubinsztein-Dunlop, "Condensed-phase optical refrigeration," *J. Opt. Soc. Am. B,* vol. 20, pp. 1037-1053, 2003.

[179] A. Rayner, M. Hirsch, N. R. Heckenberg, and H. Rubinsztein-Dunlop, "Distributed laser refrigeration," *Applied Optics,* vol. 40, pp. 5423-5429, 2001.

[180] S. Melgaard, A. R. Albrecht, M. Hehlen, D. Seletskiy, and M. Sheik-Bahae, "Optical refrigeration cools below 100K," in *CLEO: 2014,* San Jose, California, 2014, p. FTh4D.4.

[181] S. Melgaard, A. R. Albrecht, D. Seletskiy, R. Epstein, J. Alden, and M. Sheik-Bahae, "Solid-state cryo-cooling using optical refrigeration," in *CLEO: 2014,* San Jose, California, 2014, p. FTh4D.6.

[182] D. V. Seletskiy, S. D. Melgaard, R. I. Epstein, A. Di Lieto, M. Tonelli, and M. Sheik-Bahae, "Precise determination of minimum achievable temperature for solid-state optical refrigeration," *Journal of Luminescence,* vol. 133, pp. 5-9, 2011.

[183] M. P. Hasselbeck, M. Sheik-Bahae, and R. I. Epstein, "Effect of high carrier density on luminescence thermometry in semiconductors," in *Laser Cooling of Solids*, 2007, pp. 646107-646107-5.

[184] R. Kashyap, *Fiber Bragg Gratings*: Academic Press, 2009.

[185] A. J. v. Wyk, L. S. Pieter, and A. C. Anatoli, "Fibre Bragg grating gas temperature sensor with fast response," *Measurement Science and Technology,* vol. 17, p. 1113, 2006.

[186] M. Gagné and R. Kashyap, "New nanosecond Q-switched Nd:VO4 laser fifth harmonic for fast hydrogen-free fiber Bragg gratings fabrication," *Optics Communications,* vol. 283, pp. 5028-5032, 2010.

[187] G. T. Reid, "Automatic fringe pattern analysis: A review," *Optics and Lasers in Engineering,* vol. 7, pp. 37-68, 1986.

[188] E. Soares de Lima Filho, M. D. Baiad, M. Gagné, and R. Kashyap, "Fiber Bragg gratings for low-temperature measurement," *Optics Express,* vol. 22, pp. 27681-27694, 2014.

[189] M. Toru, T. Hiroaki, and K. Hideo, "High-sensitivity cryogenic fibre-Bragg-grating temperature sensors using Teflon substrates," *Measurement Science and Technology,* vol. 12, p. 914, 2001.

[190] M.-C. Wu, R. H. Pater, and S. L. DeHaven, "Effects of coating and diametric load on fiber Bragg gratings as cryogenic temperature sensors," 2008, pp. 693303-693303-10.

[191] S. Parne, R. Sai Prasad, S. G. Dipankar, M. Sai Shankar, and S. Kamineni, "Polymer-coated fiber Bragg Grating Sensor for cryogenic temperature measurements," *Microwave and Optical Technology Letters,* vol. 53, pp. 1154-1157, 2011.

[192] M. B. Reid and M. Ozcan, "Temperature dependence of fiber optic Bragg gratings at low temperatures," *Optical Engineering,* vol. 37, pp. 237-240, 1998.

[193] T. J. Quinn, *Temperature*. London; New York: Academic Press, 1983.

[194] P. K. Bachmann, D. U. Wiechert, and T. P. M. Meeuwsen, "Thermal expansion coefficients of doped and undoped silica prepared by means of PCVD," *Journal of Materials Science,* vol. 23, pp. 2584-2588, 1988.

[195] S. Chénais, F. Balembois, F. Druon, G. Lucas-Leclin, and P. Georges, "Thermal lensing in diode-pumped ytterbium lasers-Part I: theoretical analysis and wavefront measurements," *Quantum Electronics, IEEE Journal of,* vol. 40, pp. 1217-1234, 2004.

[196] Y. Jaluria, *Natural convection*: Pergamon Press Oxford, 1980.

[197] P. M. Teertstra, M. M. Yovanovich, and J. R. Culham, *Models and Experiments for Laminar Natural Convection from Heated Bodies in Enclosures*: University of Waterloo, 2003.

[198] P. Shi, B. Bai, L. Zhang, L. Li, and Y. Xin, "Semianalytical thermal analysis of the heat capacity of YAG laser rods," *Appl. Opt.,* vol. 48, pp. 6701-6707, 2009.

[199] I. Kudryashov, N. Ter-Gabrielyan, and M. Dubinskii, "Resonantly diode-pumped Er:YAG laser: 1470-nm versus 1530-nm CW pumping case," 2009, pp. 732505-732505-11.

[200] K. Spariosu and M. Birnbaum, "Intracavity 1.549μm pumped 1.634μm Er:YAG lasers at 300 K," *Quantum Electronics, IEEE Journal of,* vol. 30, pp. 1044-1049, 1994.

[201] S. D. Setzler, M. J. Shaw, M. J. Kukla, J. R. Unternahrer, K. M. Dinndorf, J. A. Beattie, *et al.*, "A 400W cryogenic Er:YAG laser at 1645 nm," 2010, pp. 76860C-76860C-7.

[202] B. Denker, B. Galagan, V. Osiko, S. Sverchkov, A. M. Balbashov, J. E. Hellström, *et al.*, "Yb^{3+},Er^{3+}:YAG at high temperatures: Energy transfer and spectroscopic properties," *Optics Communications,* vol. 271, pp. 142-147, 2007.

[203] L. D. DeLoach, S. A. Payne, L. L. Chase, L. K. Smith, W. L. Kway, and W. F. Krupke, "Evaluation of absorption and emission properties of Yb^{3+} doped crystals for laser applications," *Quantum Electronics, IEEE Journal of,* vol. 29, pp. 1179-1191, 1993.

[204] D. E. McCumber, "Einstein Relations Connecting Broadband Emission and Absorption Spectra," *Physical Review,* vol. 136, pp. A954-A957, 1964.

[205] F. D. Patel, E. C. Honea, J. Speth, S. A. Payne, R. Hutcheson, and R. Equall, "Laser demonstration of $Yb_3Al_5O_{12}$ (YbAG) and materials properties of highly doped Yb:YAG," *Quantum Electronics, IEEE Journal of,* vol. 37, pp. 135-144, 2001.

[206] G. Nemova and R. Kashyap, "Laser cooling in Yb^{3+}: YAG," *To be published in Journal of the Optical Society of America B.*

[207] M. Esmaeilzadeh, H. Roohbakhsh, and A. Ghaedzadeh, "Experimental Study on Temperature Dependence of Absorption and Emission Properties of Yb: YAG Crystal as a

Disk Laser Medium," *World Academy of Science, Engineering and Technology,* vol. 63, pp. 436-439, 2012.

[208] J. Parker, D. Mar, S. Von der Porten, J. Hankinson, K. Byram, C. Lee, *et al.*, "Thermal links for the implementation of an optical refrigerator," *Journal of Applied Physics,* vol. 105, pp. 013116-11, 2009.

[209] M. P. Hehlen, W. L. Boncher, and S. P. Love, "Design study of a laser-cooled infrared sensor," in *Laser Refrigeration of Solids VIII,* 2015, pp. 93800I-93800I-15.

[210] K. W. Martin, J. Schomacker, T. Fraser, and C. Dodson, "Thermal modeling for an optical refrigerator," in *Laser Refrigeration of Solids VIII,* 2015, pp. 93800J-93800J-8.

[211] G. A. Newburgh, A. Michael, and M. Dubinskii, "Composite Yb:YAG/SiC-prism thin disk laser," *Opt. Express,* vol. 18, pp. 17066-17074, 2010.

[212] K. Kroy, "Levitating nanoparticles: Non-equilibrium nano-thermometry," *Nat Nano,* vol. 9, pp. 415-417, 2014.

[213] D. Rings, R. Schachoff, M. Selmke, F. Cichos, and K. Kroy, "Hot Brownian Motion," *Physical Review Letters,* vol. 105, p. 090604, 2010.

[214] G. M. Hale and M. R. Querry, "Optical Constants of Water in the 200-nm to 200-μm Wavelength Region," *Applied Optics,* vol. 12, pp. 555-563, 1973.

[215] W. C. Waggener, "Absorbance of Liquid Water and Deuterium Oxide between 0.6 and 1.8 Microns. Comparison of Absorbance and Effect of Temperature," *Analytical Chemistry,* vol. 30, pp. 1569-1570, 1958.

[216] M. L. Viger, W. Sheng, K. Doré, A. H. Alhasan, C.-J. Carling, J. Lux, *et al.*, "Near-Infrared-Induced Heating of Confined Water in Polymeric Particles for Efficient Payload Release," *ACS Nano,* vol. 8, pp. 4815-4826, 2014.

[217] X. L. Ruan and M. Kaviany, "Enhanced laser cooling of rare-earth-ion-doped nanocrystalline powders," *Physical Review B,* vol. 73, p. 155422, 2006.

[218] X. Xue, S. Uechi, R. N. Tiwari, Z. Duan, M. Liao, M. Yoshimura, *et al.*, "Size-dependent upconversion luminescence and quenching mechanism of LiYF4: Er3+/Yb3+ nanocrystals with oleate ligand adsorbed," *Optical Materials Express,* vol. 3, pp. 989-999, 2013.

[219] M. D. Kelzenberg, S. W. Boettcher, J. A. Petykiewicz, D. B. Turner-Evans, M. C. Putnam, E. L. Warren, *et al.*, *Nat. Mater.,* vol. 9, p. 239, 2010.

[220] A. Bensalah, Y. Guyot, A. Brenier, H. Sato, T. Fukuda, and G. Boulon, "Spectroscopic properties of Yb^{3+}: $LuLiF_4$ crystal grown by the Czochralski method for laser applications and evaluation of quenching processes: a comparison with Yb^{3+}: $YLiF_4$," *Journal of Alloys and Compounds,* vol. 380, pp. 15-26, 2004.

[221] N. Coluccelli, "Diode pumped passively mode-locked Yb:YLF laser," *Opt. Express,* vol. 16, pp. 2922-2927, 2008.

[222] M. Ito, G. Boulon, A. Bensalah, Y. Guyot, C. Goutaudier, and H. Sato, "Spectroscopic properties, concentration quenching, and prediction of infrared laser emission of Yb^{3+}-doped KY_3F_{10} cubic crystal," *Journal of the Optical Society of America B,* vol. 24, pp. 3023-3033, 2007.

[223] F. Wang and X. Liu, "Recent advances in the chemistry of lanthanide-doped upconversion nanocrystals," *Chemical Society Reviews*, vol. 38, pp. 976-989, 2009.

[224] X. Zhu and N. Peyghambarian, "High-Power ZBLAN Glass Fiber Lasers: Review and Prospect," *Advances in OptoElectronics*, vol. 2010, 2010.

[225] S. Salaün, M. T. Fornoni, A. Bulou, M. Rousseau, P. Simon, and J. Y. Gesland, "Lattice dynamics of fluoride scheelites: I. Raman and infrared study of $LiYF_4$ and $LiLnF_4$ (Ln = Ho, Er, Tm and Yb)," *Journal of Physics: Condensed Matter*, vol. 9, p. 6941, 1997.

[226] S. Melgaard, D. Seletskiy, V. Polyak, Y. Asmerom, and M. Sheik-Bahae, "Identification of parasitic losses in Yb: YLF and prospects for optical refrigeration down to 80K," *Optics express*, vol. 22, pp. 7756-7764, 2014.

[227] F. Vetrone and J. A. Capobianco, "Lanthanide-doped fluoride nanoparticles: luminescence, upconversion, and biological applications," *International Journal of Nanotechnology*, vol. 5, pp. 1306-1339, 2008.

[228] P. Babu, K. H. Jang, C. S. Rao, L. Shi, C. K. Jayasankar, V. Lavín, *et al.*, "White light generation in Dy^{3+}-doped oxyfluoride glass and transparent glass-ceramics containing CaF_2 nanocrystals," *Optics Express*, vol. 19, pp. 1836-1841, 2011.

[229] M. Wang, G. Abbineni, A. Clevenger, C. Mao, and S. Xu, "Upconversion Nanoparticles: Synthesis, Surface Modification, and Biological Applications," *Nanomedicine : nanotechnology, biology, and medicine*, vol. 7, pp. 710-729, 2011.

[230] P. Zhang, W. Steelant, M. Kumar, and M. Scholfield, "Versatile Photosensitizers for Photodynamic Therapy at Infrared Excitation," *Journal of the American Chemical Society*, vol. 129, pp. 4526-4527, 2007.

[231] X. Huang, S. Han, W. Huang, and X. Liu, "Enhancing solar cell efficiency: the search for luminescent materials as spectral converters," *Chemical Society Reviews*, vol. 42, pp. 173-201, 2013.

[232] F. Vetrone, J.-C. Boyer, J. A. Capobianco, A. Speghini, and M. Bettinelli, "Significance of Yb^{3+} concentration on the upconversion mechanisms in codoped Y_2O_3:Er^{3+},Yb^{3+} nanocrystals," *Journal of Applied Physics*, vol. 96, pp. 661-667, 2004.

[233] S. R. Bowman, J. Ganem, and C. G. Brown, "Optical cooling in multi-level systems," in *Laser Refrigeration of Solids VII*, 2014, pp. 90000G-90000G-10.

[234] G. Nemova, E. Soares de Lima Filho, S. Loranger, and R. Kashyap, "Laser Cooling With Nanoparticles," presented at the SPIE Photonics North, Montreal, Canada, 2012.

[235] M. Savarese, A. Aliberti, I. De Santo, E. Battista, F. Causa, P. A. Netti, *et al.*, "Fluorescence Lifetimes and Quantum Yields of Rhodamine Derivatives: New Insights from Theory and Experiment," *The Journal of Physical Chemistry A*, vol. 116, pp. 7491-7497, 2012.

[236] W. M. Patterson, P. C. Stark, T. M. Yoshida, M. Sheik-Bahae, and M. P. Hehlen, "Preparation and Characterization of High-Purity Metal Fluorides for Photonic Applications," *Journal of the American Ceramic Society*, vol. 94, pp. 2896-2901, 2011.

[237] S. Chenais, F. Balembois, F. Druon, G. Lucas-Leclin, and P. Georges, "Thermal lensing in diode-pumped ytterbium Lasers-Part II: evaluation of quantum efficiencies and thermo-optic coefficients," *Quantum Electronics, IEEE Journal of*, vol. 40, pp. 1235-1243, 2004.

[238] N. Barnes and B. M. Walsh, "Quantum efficiency measurements of Nd:YAG, Yb:YAG, and Tm:YAG," in *Advanced Solid-State Lasers*, Québec City, Canada, 2002, p. TuB15.

[239] J. L. Blows, P. Dekker, P. Wang, J. M. Dawes, and T. Omatsu, "Thermal lensing measurements and thermal conductivity of Yb:YAB," *Applied Physics B*, vol. 76, pp. 289-292, 2003.